An Invariant Extended Kalman Filter for Indirect Wind Estimation Using a Small, Fixed-Wing Uncrewed Aerial Vehicle

Zakia Ahmed

Dissertation submitted to the Faculty of the
Virginia Polytechnic Institute and State University
in partial fulfillment of the requirements for the degree of

Doctor of Philosophy
in
Mechanical Engineering

Craig A. Woolsey, Chair
Mary Kasarda
Kevin Kochersberger
Shane Ross

May 08, 2024
Blacksburg, Virginia

Keywords: Wind estimation, invariant EKF, geometric mechanics

An Invariant Extended Kalman Filter for Indirect Wind Estimation Using a Small, Fixed-Wing Uncrewed Aerial Vehicle

Zakia Ahmed

(ABSTRACT)

Atmospheric sensing tasks, including measuring the thermodynamic state (pressure, temperature, and humidity) and kinematic state (wind velocity) of the atmospheric boundary layer (ABL) can aid in numerical weather prediction, help scientists assess climatological and topological features over a region, and can be incorporated into flight path planning and control of small aircraft. Small uncrewed aerial vehicles (UAVs) are becoming an attractive platform for atmospheric sensing tasks as they offer increased maneuverability and are low-cost instruments when compared to traditional atmospheric sensing methods such as ground-based weather stations and weather balloons. *In situ* measurements using a UAV can be obtained for the thermodynamic state of the ABL using dedicated sensors that directly measure pressure, temperature, and humidity whereas the kinematic state (wind velocity) can be measured directly, using, for example, a five-hole Pitot probe or a sonic anemometer mounted on an aircraft, or indirectly. Indirect measurement methods consider the dynamics of the aircraft and use measurements from its operational sensor suite to infer wind velocity. This work is concerned with the design of the invariant extended Kalman filter (invariant EKF) for indirect wind estimation using a small, fixed-wing uncrewed aerial vehicle. Indirect wind estimation methods are classified as model-based or model-free, where the model refers to the aerodynamic force and moment model of the considered aircraft. The invariant EKF is designed for aerodynamic model-free wind estimation using a fixed-wing UAV in horizontal-plane flight and the full six degree of freedom UAV. The design of the invariant

EKF relies on leveraging the symmetries of the dynamic system in the estimation scheme to obtain more accurate estimates where convergence of the filter is guaranteed on a larger set of trajectories when compared to conventional estimation techniques, such as the conventional extended Kalman filter (EKF). The invariant EKF is applied on both simulated and experimental flight data to obtain wind velocity estimates where it is successful in providing accurate wind velocity estimates and outperforms the conventional EKF. Overall, this work demonstrates the feasibility and effectiveness of implementing an invariant EKF for aerodynamic model-free indirect wind estimation using only the available measurements from the operational sensor suite of a UAV.

An Invariant Extended Kalman Filter for Indirect Wind Estimation Using a Small, Fixed-Wing Uncrewed Aerial Vehicle

Zakia Ahmed

(GENERAL AUDIENCE ABSTRACT)

Atmospheric sensing tasks, such as obtaining measurements of the pressure, temperature, humidity, and wind velocity of the atmospheric boundary layer (ABL), the lowest part of the atmosphere, have historically been dominated by the use of ground-based weather stations and deployment of weather balloons. Uncrewed aerial vehicles (UAVs) are emerging as an attractive, cost-effective platform for measuring desired quantities in the ABL. A UAV provides increased maneuverability when compared to fixed ground-based sensors and weather balloons as it can fly in different patterns and over any specified region within physical limits. Measurements of the ABL can help atmospheric scientists improve numerical weather prediction by providing more temporally and spatially dense data, in addition to helping assess climatological or topological features such as how the flow of wind varies over different types of terrain. A UAV can measure wind velocity directly or indirectly. Direct wind velocity measurements require mounting a dedicated wind sensor on a UAV and indirect measurement methods require only knowledge of the UAV's motion model with measurements from sensors already onboard to support automated flight. This work is concerned with designing an estimator for indirect wind velocity estimation using a small, fixed-wing UAV and only measurements from its operational sensor suite. The estimator, the invariant extended Kalman filter, leverages the symmetries of the system to provide estimates of the state or extended state of the system which can include position, velocity, and wind velocity. A system with symmetry is one that is unchanged by actions or transformations such

as translation and rotation. The knowledge that the system remains unchanged under some transformations is used in the design of the invariant EKF. This estimator is then implemented for indirect wind estimation on both simulated and experimental flight data where it, in general, outperforms a conventional estimation method–the extended Kalman filter. The work presented in this dissertation demonstrates the effectiveness of implementing an invariant EKF for indirect wind estimation using a small, fixed-wing UAV and measurements from its operational sensor suite.

Dedication

For my dear parents, Kamal and Shajeda Ahmed,

and my loving husband, Nazmus Sakib.

Acknowledgments

I am extremely grateful to my advisor and mentor, Dr. Craig Woolsey, for his constant guidance, support, and enthusiasm as I navigated through my doctoral studies. Dr. Woolsey, you are truly a gem of an advisor (and human being) and I will always appreciate the encouragement you gave me over the years. I would also like to thank my committee members, Dr. Mary Kasarda, Dr. Kevin Kochersberger, and Dr. Shane Ross, for serving on my committee and supporting my research endeavors with their time and ideas. Specifically, I thank Dr. Kasarda for being a mentor and safe space within the department with whom I have shared many insightful conversations.

I will always cherish the time I have spent with my colleagues in the Nonlinear Systems Lab (NSL). The camaraderie among us made my doctoral journey a pleasant one. I would like to thank Javier González-Rocha, Jean-Michel Fahmi, Mekonen Halefom, Jeremy Hopwood, Lt. Col. James Gresham, Maj. Kenneth C. Gahan, Mohammed Zakaria, Ian Willebeek-LeMair, and Dennis Marquis for their friendship.

Lastly, I would like to thank family and friends, starting with my dear husband and NSL colleague Nazmus Sakib for his love and support throughout both of our graduate studies. I have always enjoyed our time spent together while working and at home, and look forward to what the future holds for us. I am deeply indebted to my parents Kamal and Shajeda Ahmed who have showered me with unconditional love and support throughout my life. Abbu, you dreamed of completing a Ph.D. but could not due to your responsibilities. My achievement here would not have been possible without you, and I hope you regard it as your win. My parents-in-law Gaziur Rahman and Gule Mushfika Yazthajid also did their best to support my studies and I have the highest regard and love for them. My son, Zaeem Arham Sakib,

was a constant source of joy throughout the latter years of my studies. I thank my brothers Imtiaz and Ashef Ahmed for being there for me throughout my life, especially Imtiaz for being my role model. Finally, I am grateful for my friends, those I have known before my time at Virginia Tech, and those I met through my connections at Virginia Tech. More specifically, I would like to thank Meherin Mazumder, Anika Alam, Seum Karim, Shadli Islam, Mautushi Das, and Nazia Tabassum.

Contents

List of Figures

List of Tables

Chapter 1

Introduction

1.1 Motivation

Small UAVs are emerging as popular low-cost instruments in several applications such as infrastructure inspection [1, 2], crop monitoring and smart spraying [3], package delivery [4], and terrain mapping [5]. Atmospheric sensing is another prevailing application [6, 7, 8, 9, 10]. A UAV might also be used, for example, to measure the thermodynamic state (pressure, temperature, and humidity, or PTH) and kinematic state (wind velocity) of the atmospheric boundary layer (ABL). Using UAVs to sample the ABL can help scientists assess or demonstrate climatological or topological features such as variations in flow over complex terrain [7, 9, 11] or even aid in numerical weather prediction. Wind estimates obtained using UAVs can be used to validate computational fluid dynamics models of wind in the wake of a marine vessel [12, 13, 14] or can be incorporated into flight path planning and control [15]. Accurate, real-time wind velocity measurements are increasingly valuable in supporting safe, reliable flight in the air mobility concept [16] where small aircraft take off and land at urban vertiports.

Conventional methods for measuring PTH and wind velocity include ground-based weather stations and deploying weather balloons equipped with radiosondes. These methods have limited mobility as ground-based stations are fixed, and there is no control authority over balloons. Small UAVs are a desirable low-cost, *in situ* measurement platform as they can

be deployed to sample the ABL at any time and over any specified location within physical limits. Thus, UAVs can provide higher spatial and temporal resolution measurements of the ABL. UAV-based measurements of PTH are obtained by directly mounting PTH sensors onboard the aircraft. Wind velocity can be measured directly or indirectly, where direct wind measurements are obtained by mounting a dedicated sensor such as a sonic anemometer on the UAV. Direct wind measurement can provide accurate measurements, but it adds weight and cost, and the measurements are sensitive to anemometer placement and base vehicle motion [17]. Indirect wind velocity measurements are obtained using the standard onboard sensor suite comprising a global navigation satellite system (GNSS) receiver, inertial measurement unit (IMU), magnetometer, and pitot tube, along with a vehicle motion model to estimate the wind velocity. The focus of this work is indirect wind inference using small UAVs equipped with a standard onboard operational sensor suite.

Indirect wind velocity inference using UAVs can be further categorized as model-based and model-free, or a combination of the two. Model-based wind estimation uses operational sensor measurements and the aircraft dynamic model to determine wind velocity. Model-free wind estimation methods do not require knowledge of the aircraft aerodynamic model and use only operational sensor measurements to compute estimates of wind velocity. The methods are combined with different estimation approaches including linear and nonlinear filters (for random disturbances), deterministic observers, and machine learning methods. The former two approaches include the KF, EKF, UKF, and deterministic (Luenberger) observer. This work considers model-based wind estimation using a variation of the EKF called the invariant EKF that leverages the symmetries of the dynamic system in its formulation. The invariant EKF assumes the aerodynamic force and moment acting on the aircraft can be measured. These estimates will then be used with the system dynamics and other measurements to infer wind velocity.

1.2 Scope of the Work

This work concerns indirect aerodynamic model-free wind estimation using small, fixed-wing UAVs. The approach to wind inference explored is an invariant EKF where the motivation is to answer the question: Is aerodynamic model-free wind estimation possible using the invariant EKF where only measurements from the operational sensor suite of a fixed-wing UAV are available? An invariant EKF is chosen as the estimator over a conventional EKF as it has local convergence guarantees along so-called 'permanent' trajectories, which are explained in the dissertation. First, a simple example of a small, fixed-wing UAV in horizontal-plane flight is presented where the invariant EKF is applied for indirect wind estimation on the 3 degree of freedom (DOF) system. This initial implementation of the invariant EKF proves that the dynamics and measurements of the 3DOF system are $SE(2)$-invariant and equivariant, respectively, and it demonstrates the applicability of the invariant EKF for wind estimation on constant altitude flight. To extend this, the full 6DOF rigid body model of an aircraft in wind is considered where the invariant EKF is used to estimate the extended aircraft state, including wind velocity. It is proven that the aircraft dynamics are left-invariant and that the measurements are equivariant with respect to the Lie group $SE(3)$ of 6DOF rigid motions. The results of wind estimation using both the invariant EKF and conventional EKF on simulated flight data of a fixed-wing aircraft subject to 1D and 2D von Kármán turbulence are presented. A sensitivity analysis is conducted to assess the performance of the invariant EKF in the presence of high measurement noise. The invariant EKF is also applied to experimental flight data collected by the Nonlinear Systems Laboratory using the MTD2 aircraft, a small, fixed-wing UAV. The aircraft dynamics, along with the estimated force and moment and other measurements using the aircraft's standard onboard sensor suite, are used to infer wind velocity.

1.3 Contributions

The main contributions of this work are:

1. An extensive literature review of indirect wind estimation methods where several works were identified and categorized based on the type of estimator used, the aircraft considered, and whether the method used is model-based or model-free
2. A proof showing that the rigid body aircraft dynamics are left-invariant with respect to the Lie group $SE(3)$
3. The design of an invariant EKF for wind estimation using small fixed-wing UAVs
4. Development of a wind estimation scheme that requires no aerodynamic force and moment model
5. The first application of the invariant EKF to a fixed-wing UAV

Following is a list of publications that are a result of the work done in this dissertation:

1. **Ahmed, Z.**, Halefom, M. H., and Woolsey, C. A., "A Tutorial Overview of Indirect Wind Estimation Using Small Uncrewed Air Vehicles," *Journal of Aerospace Information Systems*, 2024. (To appear).
2. **Ahmed, Z.**, and Woolsey, C. A., "The Invariant Extended Kalman Filter for Wind Estimation Using a Small Fixed-wing UAV in Horizontal-Plane Flight," *AIAA SciTech Forum*, American Institute of Aeronautics and Astronautics, 2024.
3. **Ahmed, Z.**, and Woolsey, C. A., "The Invariant Extended Kalman Filter for Wind Estimation Using a Small Fixed-wing UAV," 2024. (In preparation).

4. Halefom, M. H., **Ahmed, Z.**, and Woolsey, C. A., "An Experimental Comparison of Wind Estimators for a Fixed-Wing Aircraft," (In preparation).

5. Sakib, N., **Ahmed, Z.,** and Woolsey, C.A., "A Kalman Filter-based Predictor for 6 DOF Aircraft with Input and Output Delays," *CEAS EuroGNC Conference*, 2024. (Accepted).

6. Sakib, N., **Ahmed, Z.,** and Woolsey, C.A., "Performance Analysis of Three Predictors for Mitigating Input and Output Time Delays", 2024. (In review).

1.4 Organization

This dissertation is organized as follows. Mathematical preliminaries, including a discussion on reference frames and a brief introduction to concepts from differential geometry, are provided in Chapter 2. A review of the literature on wind estimation and symmetry-preserving observers is found in Chapter 3. The rigid body aircraft dynamics in wind and common observers and estimators are given in Chapter 4. The left-invariant EKF is designed for wind estimation for a small, fixed-wing UAV in horizontal-plane flight in Chapter 5. The left-invariant EKF is designed for the full 6DOF UAV in Chapter 6 where it is applied to infer wind from both simulated and experimental flight data. Conclusions are made in Chapter 7.

Chapter 2

Mathematical Preliminaries

This chapter introduces concepts and notations used throughout the work presented in this dissertation. A brief overview of rigid body kinematics and dynamics is presented along with an introduction to ideas from geometric mechanics, including Lie groups. Common background material on dynamics includes the works of Greenwood [18] and Hand and Finch [19]. Discussions of concepts from geometric mechanics can be found in texts by Holm, Schmah, and Stoica [20], Marsden and Ratiu [21], and Bullo and Lewis [22]. The development of the invariant EKF designed in this dissertation for wind estimation also relies on classical invariant theory which can be found in a text by Olver [23].

This chapter is organized as follows. Section 2.1 provides relevant concepts from dynamics to define rigid body motion and derive the equations of motion of a rigid body. Section 2.2 briefly introduces geometric mechanics with a discussion on differential geometry, smooth manifolds, and Lie group theory. Section 2.3 reviews the necessary concepts from classical invariant theory used to develop the work in this dissertation.

2.1 Kinematics and Dynamics of a Rigid Body

This section presents the kinematic and dynamic equations of a rigid body. The *configuration* of a rigid body is expressed by giving the location of the body and its orientation in space. To define a body's configuration, the necessary frames of reference must be established. Here,

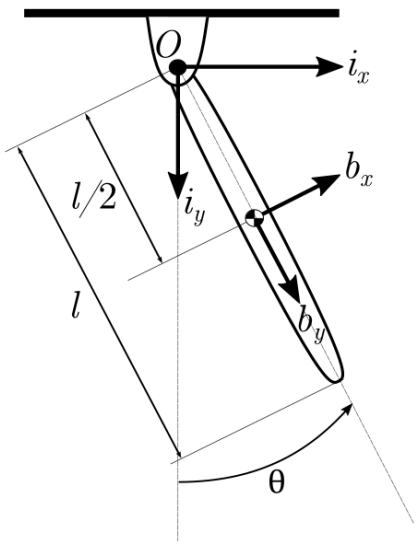

Figure 2.1: A compound pendulum with inertial frame fixed at the pivot O and body-fixed frame at the center of gravity of the pendulum.

two frames of reference are introduced: the *body-fixed* frame and the *inertial* frame. The body-fixed frame is fixed to the body at a specific reference point, for example, at the center of gravity of a rigid body. The inertial frame is considered a fixed frame of reference and the location and orientation of the body-fixed frame is expressed relative to it.

Example 2.1. Consider the compound pendulum system shown in Fig. 2.1. The body-fixed frame is located at the center of gravity of the pendulum and is denoted by the orthonormal pair $\{\boldsymbol{b}_x, \boldsymbol{b}_y\}$ and the inertial frame denoted by the orthonormal pair $\{\boldsymbol{i}_x, \boldsymbol{i}_y\}$ is defined as being fixed with its origin at the pivot O. The origin of the body-fixed frame is located at the point $\left(\frac{l}{2}\sin\theta, \frac{l}{2}\cos\theta\right)$ from O. The orientation of the body-fixed frame relative to the inertial frame is given by the angle θ.

Next, the number of *degrees of freedom* of the dynamic system is defined. The degrees of freedom of a system is the number of independent parameters required to specify its configuration. Referring back to the compound pendulum example, the orientation given by θ provides a complete description of the configuration of the pendulum. Thus, the compound

pendulum is a 1DOF system. In general, a free rigid body with 6DOF is considered where there are three translational DOF and three rotational DOF. The focus of this work is on the kinematics and dynamics of a 6DOF fixed-wing aircraft, as such, moving forward this will be the example system that is primarily referenced.

The 6DOF rigid body equations of motion describe the motion of a body-fixed frame with respect to an inertial frame, where each is a right-handed three-dimensional reference frame with mutually orthogonal axes. See Fig. 2.2. Two reference frames are used in this dissertation:

- The *inertial* reference frame is represented by the orthonormal triad $\{\boldsymbol{i}_1, \boldsymbol{i}_2, \boldsymbol{i}_3\}$. It is considered fixed, and its origin and orientation are arbitrary. In this work, the earth-fixed frame is considered an inertial over short times and distances, relative to the scale of the Earth's motion. This reference frame is referred to as the North-East-Down (NED) frame where the origin is a non-polar arbitrary point on Earth's surface, with the $\boldsymbol{i}_1$ axis pointing towards geographic north, the $\boldsymbol{i}_2$ axis pointing east, and the $\boldsymbol{i}_3$ axis pointing down.

- The *body-fixed* reference frame is represented by the orthonormal triad $\{\boldsymbol{b}_1, \boldsymbol{b}_2, \boldsymbol{b}_3\}$ with its origin at the center of gravity of the rigid body. The $\boldsymbol{b}_1$ axis points out of the "front" of the body, the $\boldsymbol{b}_2$ axis points out of the "right" side of the body, and the $\boldsymbol{b}_3$ axis points down through the "underside" of the body, completing an orthonormal frame.

In this dissertation, the earth-fixed frame is considered an inertial frame and will be referred to as such. A rotation matrix is used to describe the orientation of the body-fixed frame with respect to the inertial frame. A proper rotation matrix $\boldsymbol{R}_{12}$ maps free vectors described in frame 2 to frame 1, has determinant equal to 1, and its inverse is equal to its transpose, *i.e.*, $\boldsymbol{R}_{12}^{-1} = \boldsymbol{R}_{12}^{T}$ where $\boldsymbol{R}_{12}^{T} = \boldsymbol{R}_{21}$ where $\boldsymbol{R}_{21}$ maps free vectors from the 1 frame to the 2

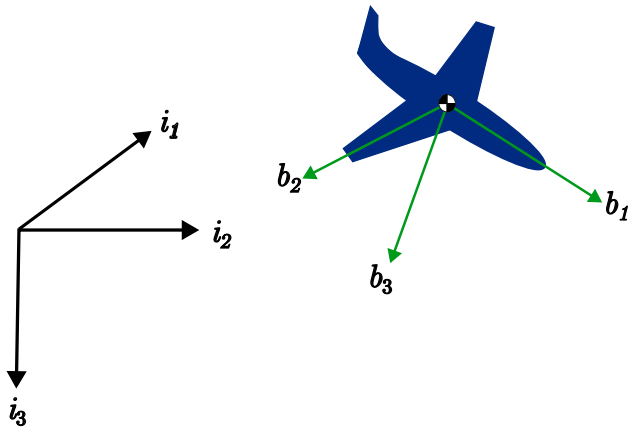

Figure 2.2: An illustration of an aircraft with body-fixed reference frame with origin at its center of gravity and an inertial frame of reference.

frame.

A rotation matrix $\boldsymbol{R}_{\mathrm{BI}}$ maps free vectors from the inertial reference frame to the body-fixed reference frame. The rotation matrix $\boldsymbol{R}_{\mathrm{BI}}$ is a proper rotation matrix in the special orthogonal group $SO(3)$. One can choose to parameterize the rotation matrix, for example, using Euler angles for roll, pitch, and yaw, and considering a 3-2-1 rotation, as shown in Fig. 2.3. It is described by, in order, rotation by an angle ψ about the $\boldsymbol{i}_3$ axis given by the matrix exponential

$$e^{\psi \hat{\boldsymbol{i}}_3} = \begin{pmatrix} \cos\psi & \sin\psi & 0 \\ -\sin\psi & \cos\psi & 0 \\ 0 & 0 & 1 \end{pmatrix},$$

then by an angle θ about the $\boldsymbol{i}_2'$ axis given by

$$e^{\theta \hat{\boldsymbol{i}}_2'} = \begin{pmatrix} \cos\theta & 0 & -\sin\theta \\ 0 & 1 & 0 \\ \sin\theta & 0 & \cos\theta \end{pmatrix},$$

and finally by an angle ϕ about the $\boldsymbol{i}_1''$ axis given by

$$e^{\phi\hat{\boldsymbol{i}}_1''} = \begin{pmatrix} 1 & 0 & 0 \\ 0 & \cos\phi & \sin\phi \\ 0 & -\sin\phi & \cos\phi \end{pmatrix}.$$

The hat operator in Fig. 2.3 denotes the cross-product equivalent matrix of a vector $\boldsymbol{a} \in \mathbb{R}^3$.

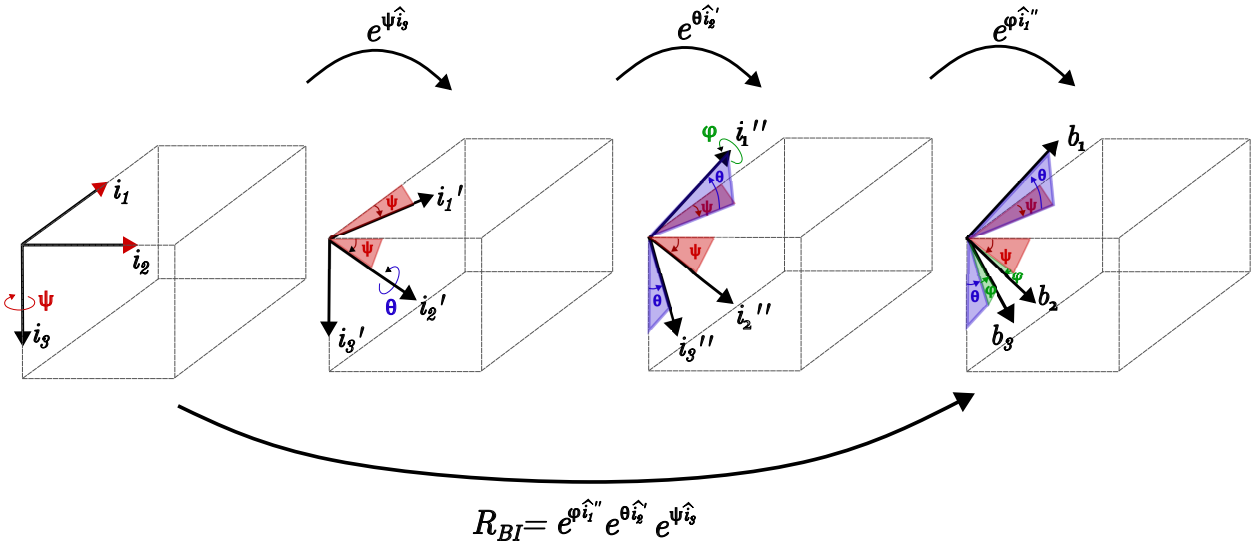

Figure 2.3: An illustration depicting a 3-2-1 rotation about an inertial frame to obtain the rotation matrix denoted $\boldsymbol{R}_{\mathrm{BI}}$.

A vector cross product $\boldsymbol{a} \times \boldsymbol{b}$ can be represented by the product of a skew-symmetric matrix and vector as $\boldsymbol{a}^{\times}\boldsymbol{b}$ or $(\boldsymbol{b}^{\times})^T\boldsymbol{a}$. The cross-product equivalent matrix of the vector $\boldsymbol{a} = (a_1, a_2, a_3)^T$ is

$$\boldsymbol{a}^{\times} = \begin{pmatrix} 0 & -a_3 & a_2 \\ a_3 & 0 & -a_1 \\ -a_2 & a_1 & 0 \end{pmatrix} \tag{2.1}$$

The cross-product equivalent matrix has a useful property where the cross-product equivalent

matrix of a vector rotated by a proper rotation matrix $\boldsymbol{R}$ is equivalent to, in order, the product of the rotation matrix, the cross-product equivalent matrix of the vector, and the transpose of the rotation matrix, *i.e.,*

$$(\boldsymbol{Ra})^{\times} = \boldsymbol{Ra}^{\times}\boldsymbol{R}^{\mathrm{T}}$$

The rotation matrix $\boldsymbol{R}_{\mathrm{BI}}$ is then

$$\begin{aligned}\boldsymbol{R}_{\mathrm{BI}} &= e^{\phi \hat{\boldsymbol{i}_1''}} e^{\theta \hat{\boldsymbol{i}_2'}} e^{\psi \hat{\boldsymbol{i}_3}} \\ &= \begin{pmatrix} \cos\theta\cos\psi & \cos\theta\sin\psi & -\sin\theta \\ \cos\psi\sin\theta\sin\phi - \cos\phi\sin\psi & \sin\phi\sin\theta\sin\psi + \cos\phi\cos\psi & \cos\theta\sin\phi \\ \cos\psi\sin\theta\cos\phi + \sin\phi\sin\psi & \sin\theta\cos\phi\sin\psi - \sin\phi\cos\psi & \cos\theta\cos\phi \end{pmatrix} \end{aligned} \tag{2.2}$$

As explained earlier, the rotation matrix $\boldsymbol{R}_{\mathrm{BI}}$ maps free vectors in the inertial frame to the body-fixed frame. The matrix $\boldsymbol{R}_{\mathrm{IB}} = \boldsymbol{R}_{\mathrm{BI}}^{\mathrm{T}}$ maps free vectors in the body-fixed frame to the inertial frame.

The kinematic equations of a system describe how the configuration of a system changes over time as a function of the system's velocity. For the 6DOF aircraft, the configuration is given by the position and orientation of the aircraft with respect to the inertial frame. The position and orientation of the aircraft in the inertial frame are given by $\boldsymbol{X} = (X, Y, Z)^{\mathrm{T}}$ and $\boldsymbol{R}_{\mathrm{IB}}$, respectively. Consider an aircraft with some translational velocity $\boldsymbol{v}$ and angular velocity $\boldsymbol{\omega}$ expressed in the body-fixed frame. The translational and rotational velocities in the inertial frame are given by

$$\frac{d}{dt}\boldsymbol{X} = \boldsymbol{R}_{\mathrm{IB}}\boldsymbol{v} \tag{2.3}$$

$$\frac{d}{dt}\boldsymbol{R}_{\mathrm{IB}} = \boldsymbol{R}_{\mathrm{IB}}\boldsymbol{\omega}^{\times} \tag{2.4}$$

Equation (2.4) can be simplified and written as three differential equations in terms of Euler angle rates instead of as a matrix differential equation given by

$$\begin{pmatrix} \dot{\phi} \\ \dot{\theta} \\ \dot{\psi} \end{pmatrix} = \underbrace{\begin{pmatrix} 1 & \sin\phi\tan\theta & \cos\phi\tan\theta \\ 0 & \cos\phi & -\sin\phi \\ 0 & \sin\phi\sec\theta & \cos\phi\sec\theta \end{pmatrix}}_{\boldsymbol{L}_{\mathrm{IB}}} \boldsymbol{\omega} \tag{2.5}$$

where the Euler angles are the roll, pitch, and yaw angles $\boldsymbol{\Theta} = (\phi, \theta, \psi)^{\mathrm{T}}$. The matrix $\boldsymbol{L}_{\mathrm{IB}}$ maps the angular velocities expressed in the body-fixed frame to the Euler angle rates $\frac{d}{dt}\boldsymbol{\Theta} = (\dot{\phi}, \dot{\theta}, \dot{\psi})^{\mathrm{T}}$. An issue that arises with Eq. (2.5) is that it faces singularity when the pitch angle θ passes through $\pm\pi$. A fixed-wing aircraft does not typically approach $\theta = \pm\pi$, as such, the Euler angle parameterization of the rotation matrix is used. Other parameterizations of the rotation matrix one can adopt that avoid the singularity include unit quaternions and Modified Rodrigues Parameters. The focus of this dissertation is on fixed-wing aircraft, thus the Euler angle parameterization is adopted throughout the work.

The dynamic equations of a system represent the forces acting on the system over time. Consider a 6DOF rigid body with translational momentum $\boldsymbol{p} = m\boldsymbol{v}$ and angular momentum $\boldsymbol{h} = \boldsymbol{I}\boldsymbol{\omega}$ defined at the center of mass of the body with respect to the inertial frame. The body has mass m and matrix moments of inertia in the body-fixed frame $\boldsymbol{I}$. Using Newton's second law of motion the dynamics are

$$\begin{aligned} \left.\frac{d}{dt}\right|_{\mathrm{Inertial}} \boldsymbol{p} &= \boldsymbol{R}_{\mathrm{BI}}\boldsymbol{F} &&= \dot{\boldsymbol{p}} + \boldsymbol{\omega} \times \boldsymbol{p} \\ \left.\frac{d}{dt}\right|_{\mathrm{Inertial}} \boldsymbol{h} &= \boldsymbol{R}_{\mathrm{BI}}\boldsymbol{M} &&= \dot{\boldsymbol{h}} + \boldsymbol{\omega} \times \boldsymbol{h} \end{aligned}$$

where the inertial vectors $\boldsymbol{F}$ and $\boldsymbol{M}$ are the sum of external forces and total external moment

about the body's center of mass, respectively. The equations of motion in the body-fixed frame are then given by

$$m\dot{\boldsymbol{v}} + \boldsymbol{\omega} \times m\boldsymbol{v} = \boldsymbol{f} \tag{2.6}$$

$$\boldsymbol{I}\dot{\boldsymbol{\omega}} + \boldsymbol{\omega} \times \boldsymbol{I}\boldsymbol{\omega} = \boldsymbol{m} \tag{2.7}$$

where $\boldsymbol{f} = \boldsymbol{R}_{\mathrm{BI}}\boldsymbol{F}$ and $\boldsymbol{m} = \boldsymbol{R}_{\mathrm{BI}}\boldsymbol{M}$. For a rigid aircraft, the sum of forces acting on the body $\boldsymbol{f}$ can be expressed as the sum of the force due to the acceleration of gravity and aerodynamic forces given by

$$\boldsymbol{f} = \boldsymbol{R}_{\mathrm{IB}}^{\mathrm{T}} m\boldsymbol{g} + \boldsymbol{f}_{\mathrm{A}}$$

where $\boldsymbol{g} = (0, 0, g)^{\mathrm{T}}$, g is the acceleration due to gravity, and $\boldsymbol{f}_{\mathrm{A}}$ is the aerodynamic force expressed in the body-fixed frame. The kinematics and dynamics of a 6DOF rigid fixed-wing aircraft are then Eqs. (2.3), (2.5), (2.6), and (2.7).

2.2 A Brief Introduction to Geometric Mechanics

A brief introduction to geometry mechanics and symmetry is provided adapting definitions from Holm, Schmah, and Stoica [20]. Marsden and Ratiu [21], Bullo and Lewis [22], Murray, Li and Sastry [24], and Boothy [25] are additional references for an introduction to differential geometry.

The configuration of a system can be described as a point in a smooth manifold. A topological space called a manifold is a smooth curve, surface, or higher dimensional space where there exist consistent local coordinate charts. An n-dimensional manifold M has the following properties [25]:

1. M is Hausdorff,

2. M is locally Euclidean of dimension n, and

3. M has a countable basis of open sets.

Per the above properties, an n-dimensional manifold M is locally *homeomorphic* to $\mathbb{R}^n$. That is, there exists a continuous map with a continuous inverse from some open neighborhood of a point in M to an open neighborhood in $\mathbb{R}^n$. A local coordinate chart is a pair (ϕ, U) where ϕ is a homeomorphism that maps an open set U of M to an open subset of $\mathbb{R}^n$. Consider another local coordinate chart (ψ, V). If $\psi^{-1} \circ \phi$ is a *diffeomorphism*, a differentiable map with a differentiable inverse, then two overlapping charts (ϕ, U) and (ψ, V) are C^∞ *related*. If the manifold M can be covered by a collection of C^∞ related charts, called a *smooth atlas*, then it is said to be a *smooth* manifold.

Example 2.2. The unit circle $S^1 = \{\boldsymbol{x} \in \mathbb{R}^2 : \|\boldsymbol{x}\| = 1\} = f^{-1}(1)$ where $f(\boldsymbol{x}) = f(x_1, x_2) = x_1^2 + x_2^2$ is a 1-dimensional manifold. S^1 is a subset of a Hausdorff space ($\mathbb{R}^2$) and is thus also a Hausdorff space, it is locally homeomorphic to $\mathbb{R}^1$ (a small piece of the unit circle looks like a small piece of the real line), and has a countable basis of open sets.

Consider a dynamical system, more specifically a particle, whose configuration space is the smooth manifold M. The particle may take some path $p(t) \in M$ where $p(t)$ is the position of the system at time t. Then the velocity vector at time t is the derivative of $p(t)$ given by $\dot{p}(t)$. The vector $\dot{p}(t)$ is the *tangent vector* to M at $p(t) \in M$. For a given point $q \in M$, the set of all tangent vectors based at q corresponds to the set of all possible paths in M that pass through the point q. The set of all tangent vectors based at point $q \in M$ is called *tangent space* of M at q denoted T_qM. An illustration of the tangent space T_qM is given in Fig. 2.4.

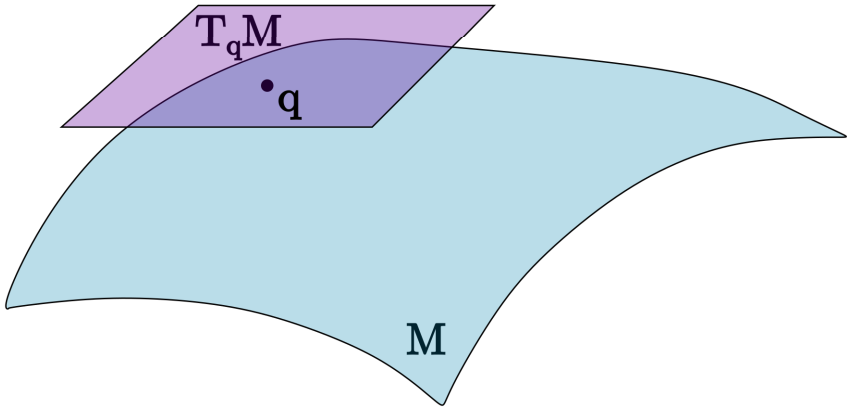

Figure 2.4: An illustration showing T_qM, the tangent space based at the point $\boldsymbol{q}$ on the manifold M.

The *tangent bundle* of M, denoted TM, is the union of all tangent spaces to M and forms a $2n$-dimensional manifold. The tangent bundle is the space of all possible configurations and velocities of a dynamical system. A common way to refer to a point on a manifold and its tangent space is to call them base and fiber coordinates where a "fiber" is the tangent space in TM and the base point is the corresponding point in the manifold M.

The equations of motion of a dynamical system may be defined with respect to some smooth manifold M describing the configuration of the system. A *vector field* $\boldsymbol{X}$ is a map $\boldsymbol{X} : M \to TM$ that assigns a tangent vector $X(q) \in T_qM \ \forall q \in M$. A *smooth* vector field is a vector field that is a smooth map from the manifold M to the tangent bundle TM. The vector space of all smooth vector fields on M is denoted $\mathfrak{X}(M)$. For a dynamical system with configuration manifold M, one may think of the vector field X written in coordinates as the ordinary differential equations that describe the motion of the system. A differentiable map $c : I \to M$ where I is an open interval in $\mathbb{R}$ that satisfies $\dot{c}(t) = X(c(t))$ for all $t \in I$ is an *integral curve* of X. Integral curves are also called *solution curves* or *trajectories* of the vector field X. The *flow* of a vector field X on a manifold M is a differentiable map $\phi : U \times I \to M$ over an interval $I \subseteq \mathbb{R}$ containing 0 and U is an open subset of M such that $\phi_u(t) := \phi(u, t)$ is an integral curve of X with $\phi_u(0) = u$ for all $u \in U$.

A *group* G is a set of elements with a binary operation $G \times G \to G$ that satisfies the following properties:

1. $(gh)k = g(hk)$ for all $g, h, k \in G$ (*associative* property);
2. there is an *identity* element $e \in G$, satisfying $g = eg = ge$ for all $g \in G$; and
3. an *inverse* element g^{-1} exists for all $g \in G$ satisfying $gg^{-1} = g^{-1}g = e$.

Additionally, the group is called *commutative* or *Abelian* if $gh = hg$ for all $g, h \in G$. A *matrix group* is a subset of $\mathcal{M}(n, \mathbb{R})$ or $\mathcal{M}(n, \mathbb{C})$ that satisfies the properties of being a group where the group operation is matrix multiplication.

To generalize the concept of a matrix Lie group, *Lie groups* are introduced. A Lie group is a smooth manifold that also satisfies the group axioms that the operations of group multiplication and inversion are smooth. Lie groups whose elements are represented as matrices are called matrix Lie groups. A *matrix Lie group* is a matrix group that is also a submanifold of $\mathcal{M}(n, \mathbb{R})$ or $\mathcal{M}(n, \mathbb{C})$. In other words, a matrix Lie group G is a differentiable manifold equipped with matrix multiplication as the group action where group multiplication and inversion are smooth. In addition, a matrix Lie group must include the identity matrix $\mathbb{I}$ to satisfy the group conditions. Each element in a Lie group may represent a configuration or a transformation that maps one configuration to another. For any matrix Lie group G, a *matrix Lie algebra* denoted $\mathfrak{g}$ is the tangent space to G at the identity element $\mathbb{I}$, $T_I G$. A matrix Lie algebra is defined as a vector subspace of $\mathcal{M}(n, \mathbb{R})$ or $\mathcal{M}(n, \mathbb{C})$ for some n, with matrix addition and scalar multiplication, that is also closed under the matrix commutator. The *matrix commutator* of any pair of $n \times n$ matrices A and B is $[A, B] := AB - BA$. The group of proper rotation matrices is the matrix Lie group $SO(3)$, the special orthogonal group comprising 3×3 matrices whose inverse is their transpose and with determinant 1.

The Lie algebra of $SO(3)$ is $\mathfrak{so}(3)$ which is the space of 3×3 skew-symmetric matrices. Every matrix Lie group is also a Lie group where matrix multiplication is the group operation.

A property of a Lie group is that an entire atlas may be constructed given a local coordinate chart. The operation of group multiplication allows for this. For a Lie group G with elements g, a *left translation* by g is the map

$$L_g : G \to G, \qquad h \to L_g(h) := gh$$

A left translation and its inverse are smooth. A *right translation* by g is the map

$$R_g : G \to G, \qquad h \to R_g(h) := hg$$

A *Lie algebra* is a vector space $\mathcal{A}$ with a bilinear operation $(v, w) \in \mathcal{A} \times \mathcal{A} \to [v, w] \in \mathcal{A}$, called the *bracket*, such that

1. $[v, w] = -[v, w]$ for all $v, w \in V$ (skew-symmetry)
2. $[[v, w], u] + [[u, v], w] + [[w, u], v] = 0$ for all $u, v, w \in V$ (Jacobi identity)

An example of a Lie algebra is a vector space $\mathcal{X}(M)$ of all smooth vector fields on a smooth manifold M with the *Jacobi-Lie bracket* (in local coordinates) $[X, Y] = X \cdot \nabla Y - Y \cdot \nabla X$. The *left extension* of any $\xi \in T_eG$ is the vector field X^L_ξ given by

$$X^L_\xi(g) := T_eL_g(\xi)$$

where the tangent map T_eL_g shifts vectors based at e to vectors based at $g \in G$. A vector

field $X : G \to TG, h \to X(h)$, is called *left-invariant* if

$$T_h L_g(X(h)) = X(L_g(h)) = X(gh), \qquad \text{for all } g, h \in G.$$

A *smooth left action* of a Lie group G on a manifold M is a smooth mapping $\phi : G \times M \to M$ such that

1. $\phi(e, x) = x$ for all $x \in M$,
2. $\phi(g, \phi(h, x)) = \phi(gh, x)$ for all $g, h \in G$ and $x \in M$, and
3. For every $g \in G$, the map $\phi_g : M \to M$, defined by

$$\phi_g(x) := \phi(g, x)$$

   is a diffeomorphism.

A *smooth right action* of a Lie group G on a manifold M is a smooth mapping $\phi : G \times M \to M$ satisfying the same conditions as a smooth left action, except that condition (2) is replaced by:

2. $\phi(g, \phi(h, x)) = \phi(hg, x)$ for all $g, h \in G$ and $x \in M$.

Convenient notation for a left action is

$$gx := \phi_g(x) = \phi(g, x),$$

and for a right action is

$$xg := \phi_g(x) = \phi(g, x).$$

According to [20], any left action gives gx gives rise to a right action $g^{-1}x$, and vice versa, where any right action xg gives rise to a left action xg^{-1}.

A function f is said to be *invariant* with respect to the action ϕ of the Lie group G, if for every $g \in G$, the map ϕ_g is a symmetry of f, *i.e.*,

$$f \circ \phi_g = f$$

The group G is called a symmetry group of f. Suppose G acts on two manifolds M and N. A map $h : M \to N$ maps an element $x \in M$ to the manifold N and is said to be *equivariant* with respect to the action of G, if for all $g \in G$ and $x \in M$,

$$h(gx) = gh(x)$$

2.3 A Basic Overview of Classical Invariant Theory

An overview of concepts from classical invariant theory is provided in this section following the discussion by Olver [23]. The discussion of classical invariant theory aids in understanding the design of symmetry-preserving observers introduced by Bonnabel *et al.* in [26], the foundation for the invariant EKF, and a focus of this work. Topics discussed include transformation groups, symmetry groups, group orbits, and normalization.

A *transformation group* acting on a space X is a group homomorphism $\rho : G \to \mathcal{G}(X)$ mapping a group G to the group of invertible maps on X. That is, each element $g \in G$ induces an invertible map $\rho(g) : X \to X$. For this mapping to be a group homomorphism, the mapping ρ must satisfy the group properties of associativity, containing an identity element and an inverse element. A transformation group is called a *symmetry group* if an

object is fixed under the action of the transformation group. More specifically, for a subset Y of X, $Y \subset X$, a *symmetry* of Y is an invertible transformation $\phi : X \to X$ that leaves Y unchanged, *i.e.*, $\phi(Y) = Y$. The *symmetry group* of Y is the collection of all symmetries of Y which form a subgroup of the group of all invertible transformations on X. A transformation group G is a *symmetry group* of the subset Y if each element $g \in G$ is a symmetry. Then Y is called a *G-invariant subset* of X.

An *orbit* of a transformation group is a minimal nonempty invariant subset. A *fixed-point* is a G-invariant point $x \in X$ such that $g \cdot x = x$.

Example 2.3. Consider actions by the space of planar rotations $SO(2)$ on elements of $(x, y) \in \mathbb{R}^2 \backslash \{\mathbf{0}\}$. Orbits of the transformation group $SO(2)$ are circles of radius $r = \sqrt{x^2 + y^2}$ centered at the origin.

Let G be a transformation group acting on the space X. An *invariant* is a real-valued function $I : X \to \mathbb{R}$ which satisfies $I(g \cdot x) = I(x)$ for all $g \in G$. The following are equivalent:

1. I is a G-invariant function.
2. I is constant on the orbits of G.
3. All level sets $\{I(x) = c\}$ are G-invariant subsets of X.

Example 2.4. For the action of the group of planar rotations $SO(2)$ on $\mathbb{R}^2$, the radius $r = \sqrt{x^2 + y^2}$ is an invariant function. The invariant function r distinguishes between the orbits: two points lie in the same orbit if they have the same value r.

Consider the action of a Lie group G on an n-dimensional manifold M with s-dimensional orbits. A local *cross-section* is an $(n - s)$-dimensional submanifold $K \subset M$ such that K

intersects each orbit transversally and at most once. That is, K does not share any common tangent directions of the orbits of M.

Let G act on M so that the orbits have the same dimension m as G. A coordinate cross-section, defined by m coordinates, $K = \{x_1 = c_1, \cdots, x_m = c_m\}$ is chosen. Let $g = (g_1, \cdots, g_m)$ on G be local coordinates in a neighborhood of the identity element. The formulae for the group transformations are then written as $\bar{x} = g \cdot x = w(g, x)$ in the given coordinates. The *normalization equations* for the coordinate cross-section are obtained by equating the first m components of the function w to the given constants,

$$\bar{x}_1 = w_1(g, x) = c_1, \qquad \cdots \qquad , \bar{x}_m = w_m(g, x) = c_m,$$

where the constants $(c_1, \cdots, c_m)$ must lie in the range of the function w. The assumption that K is a cross-section allows for the invocation of the Implicit Function Theorem which implies that the normalization equations can be locally solved for the group parameters in terms of the coordinates x. The solution is written as $g = \gamma(x)$ where the resulting map $\gamma : M \to G$ is the *moving frame* associated with the given cross-section.

The moving frame defining the group element $g = \gamma(x)$ maps the point x to its canonical form $k \in K$ where

$$k = \gamma(x) \cdot x = w(\gamma(x), x).$$

The components of the canonical form k are the invariants defined by the given cross-section. For the given cross-section, the first m components of k are the normalization constants $(c_1, \cdots, c_m)$, and the remaining $(n - m)$ components provide a complete set of functionally independent invariants. Theorem 8.25 in [23] states that given a Lie group action and a coordinate cross-section, and the solution to the normalization equations $g = \gamma(x)$, the

functions

$$I_1(x) = w_{m+1}(\gamma(x), x), \qquad \cdots \qquad , I_{n-m}(x) = w_n(\gamma(x), x),$$

are a complete system of functionally independent invariants for the action of the Lie group G. The functions $I_1, \cdots, I_{n-m}$ are obtained by substituting the moving frame formulae into the remaining $n - m$ components of the function w.

Chapter 3

Literature Review

The design of an invariant EKF for indirect wind estimation using a small UAV requires background knowledge in both wind estimation and symmetry-preserving observers. Wind estimation methods include direct and indirect estimation, where direct estimation involves mounting a dedicated wind sensor, such as an anemometer, on the aircraft to measure the wind velocity. Indirect wind estimation methods consider the aircraft's motion in response to wind disturbances. Indirect methods can be categorized as model-based, model-free, and combined where model-based wind estimation relies on knowledge of the aircraft's aerodynamic force and moment models and model-free wind estimation does not. Combined methods may use some pseudo-measurements or assumed force and moment models without knowledge of the true or most correct models. A detailed overview of indirect wind estimation literature follows the survey paper [27] and is provided in Section 3.1.

Indirect wind estimation methods require the implementation of an estimation scheme to estimate the extended state of the UAV. Common estimators used in indirect wind estimation include the KF, EKF, and UKF. The focus of this work is the design and implementation of the invariant EKF which is based on the work of Bonnabel *et al.* in [26]. The invariant EKF leverages the symmetries of a system to obtain state estimates. The relevant literature and applications related to symmetry-preserving observers, including the invariant EKF are discussed in Section 3.2.

3.1 Wind Estimation

Wind field estimation using UAVs can be accomplished by measuring the relative wind velocity directly or by inferring the wind velocity from the aircraft's motion. Wind estimates obtained using indirect methods are validated by comparing the obtained estimates with a truth source, such as wind measurements from a sonic anemometer or an air data unit installed on the aircraft [28]. Given the measurements or estimates of the inertial velocity and the air-relative velocity, the wind velocity can be obtained from the wind triangle relationship in Figure 3.1.

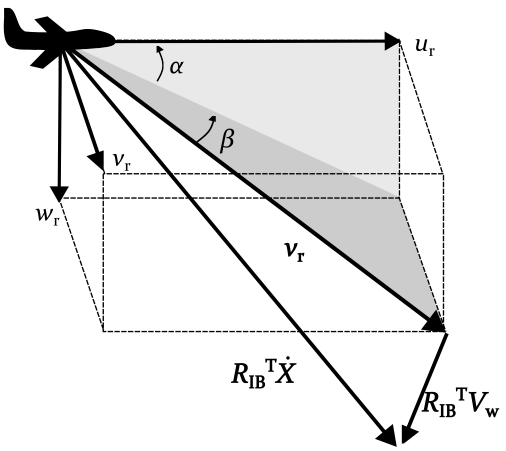

Figure 3.1: An illustration of the wind triangle including AoA and AoS.

The wind field can be separated into steady and turbulent wind components. Turbulence models can be incorporated into wind estimation algorithms. They are also used to construct realistic wind simulations as truth models to evaluate the quality of wind estimates obtained using different algorithms. When considering turbulent wind field effects on aircraft motion, the Dryden and von Kármán turbulence models for clear air turbulence are commonly used [29]. They can be used to model the dynamics of the wind in model-based wind estimation

as in [30], for example, where the Dryden model is used. Other turbulence models exist, such as the Kaimal [31] and Mann [32] turbulence models, but to the author's knowledge they have not been employed for wind estimation using UAVs. Turbulent wind can also be modeled as a simple Gauss-Markov sequence as in [33].

Indirect wind estimation methods using UAVs to solve the wind triangle relationship can be categorized as model-based and model-free. Model-based methods use the aircraft's kinematic and dynamic equations to estimate components of the wind vector whereas model-free methods do not require knowledge of the aircraft's dynamic model. These methods are coupled with different types of estimators to compute components of the wind vector and they require measurements from various operational sensors onboard a UAV. The UAVs used for wind estimation are typically equipped with a GNSS receiver that provides position and velocity with respect to the NED frame, an IMU that provides the aircraft's specific acceleration and angular velocity, a 3-axis magnetometer that provides heading, and a Pitot probe to measure airspeed. Additionally, aircraft may be instrumented with flow vanes or multi-hole Pitot probes to obtain AoA and AoS measurements. A sensor that provides airspeed, AoA, and AoS is referred to as an air data sensor (ADS).

Existing work on wind estimation formulations and different estimation techniques is summarized in Table 3.1. Table 3.1 also includes existing work where model-based and model-free methods are combined for wind estimation. Combined methods seek to use some knowledge of an aircraft's aerodynamic model and alleviate some restrictions from model-free estimation methods such as the requirement for persistent excitation of the aircraft to resolve 3D air relative velocity when 3D measurements are not available.

Model-based Methods

Model-based wind estimation methods rely on knowledge of the aircraft flight dynamic

Table 3.1: Summary of reviewed indirect wind estimation formulation and filtering methods using small UAVs. The symbols denote the type of aircraft used: ✈ = fixed-wing, ✕ = multirotor, and ✈✕ = lift+cruise.

Estimator	Model-based	Model-free	Combined
KF	Hattenberger *et al.* [34] ✕ Langelaan *et al.* [35] ✈ Xiang *et al.* [36] ✕ Petrich *et al.* [37] ✈	Balmer *et al.* [38] ✈	
EKF	Chen *et al.* [39] (IEKF) ✕ Lie *et al.* [40] ✈ Pappu *et al.* [41] ✕ Sun *et al.* [42] ✈ Tian *et al.* [43] ✈ Torgesen *et al.* [13] ✕	Cho *et al.* [44] ✈ Rautenberg *et al.* [45] ✈ Zhang *et al.* [46] ✈✕	Wenz *et al.* [47] ✈
UKF	Condomines *et al.* [48] ✈ Cooper *et al.* [49] ✕ Larrabee *et al.* [50] ✈ Lee *et al.* [51] ✈ Rhudy *et al.* [52, 53, 54] ✈	Rhudy *et al.* [54] ✈	
Deterministic Observer	Asignacion *et al.* [55] ✕ González-Rocha *et al.* [56, 57, 58] ✕		Borup *et al.* [59] ✈
Other	Azid *et al.* [60] (UIO) ✕ Hong *et al.* [61] (T-MPSP) ✈ Kumar *et al.*[12] (APF) ✕ Langelaan *et al.* [62] ✈ Marinescu *et al.* [63] (GPR) ✈ Meier *et al.* [64]✕ Neumann *et al.* [65] (Tilt) ✕ Palomaki *et al.* [66] (Tilt) ✕ Perozzi *et al.* [67] (FTE) Salazar *et al.* [68] ✈ Segales *et al.* [10] (Tilt) ✕ Shelekhov *et al.* [69] (Tilt) ✕ Velasco *et al.* [70] ✈ Wenz *et al.* [30] (MHE) ✈	Witte *et al.* [71] ✈	Benders *et al.* [15](MHE) ✈ Wenz *et al.* [30](MHE) ✈

model. Developing this model can involve ground testing to determine inertial properties, wind tunnel testing to determine propulsion models [48], and experimental and computational model identification to determine the aerodynamic force and moment structure and parameters [58, 72]. Model-based wind estimation schemes can be applied to deterministic or non-deterministic systems which use linear or nonlinear dynamic models. Deterministic observer-based wind estimation is applied to a deterministic system model. A Luenberger

observer, for example, can be used when the nonlinear flight dynamic equations are linearized about a nominal trajectory. The KF is also applied to a linearized flight dynamic model, but one in which random forcing makes the system non-deterministic. The EKF and invariant EKF-based wind estimation schemes are applied to nonlinear, non-deterministic systems. Other methods of wind estimation include optimization techniques, which rely on solving nonlinear optimal control problems, and include multi-objective optimization and model predictive static programming (MPSP).

References [10, 65, 66, 69] introduce tilt-based methods (denoted "tilt" in Table 3.1) for wind estimation using multirotor aircraft. The tilt-based wind estimation scheme is based on the deviation of the multirotor attitude from level when it hovers in place. It is assumed that the deviation is a result of a wind disturbance. This method requires only attitude and position data from the GNSS and IMU sensors onboard the multirotor aircraft. Palomaki *et al.* compare direct wind measurements using a sonic anemometer mounted on a hexacopter to indirect model-based estimation using attitude data from a quadcopter using only hovering flight [66]. Segales *et al.* fly the CopterSonde, a multirotor aircraft developed for remote sensing in the atmospheric boundary layer, to obtain experimental 2D estimates of the wind based on tilt measurements [10]. The wind velocity is calculated using pitch angle measurements by programming the CopterSonde to hover in "wind vane" mode where it orients itself to face the wind, keeping its roll angle near zero. Neumann *et al.* identify a quadcopter aerodynamic model with wind tunnel testing and perform tilt-based real-time wind estimation [65]. They solve the wind triangle relationship for the wind velocity using GNSS-based inertial velocity measurements and estimate air-relative velocity using the identified aerodynamic model with IMUand magnetometer measurements. Shelekhov *et al.* estimate atmospheric turbulence using three commercial off-the-shelf multirotor aircraft in hover at different vertically spaced points [69]. The time histories and spectral content of the quad-

copter wind estimation results are compared with measurements from three anemometers placed at different altitudes.

In [56, 57, 58] the wind is modeled as a deterministic process and the linearized equations of motion of the system are used to obtain wind estimates using a deterministic observer. González-Rocha *et al.* [57] present three quadrotor models: a kinematic particle model, a dynamic particle model, and a rigid body model. In [57], 2D estimates of the wind are obtained using both the kinematic and dynamic particle models by directly solving the wind triangle relationship for wind velocity using measurements of inertial and air-relative velocity from GNSS, IMU, magnetometer, and barometer data. In [58], the authors compare wind velocity estimates obtained using the three quadcopter models to measurements from a sonic anemometer. The rigid body model of the aircraft is linearized about steady straight and level forward flight and the state is augmented to include the wind velocity, assuming the wind to be slowly varying compared to the aircraft motion. It was found that increasing the fidelity of the model resulted in more accurate wind speed estimates, with the rigid body model providing the best wind speed estimates. In [56] the rigid body model is used to estimate wind velocity with a quadcopter in hover and in steady ascent where the quadcopter aerodynamic force and moment models were identified using stepwise regression and output error parameter estimation using flight test data. This study also assumed the wind to be slowly varying compared to the aircraft and compared wind velocity estimates in hover and steady ascent to wind velocities measured using sound detecting and ranging (SoDAR). The dynamic particle model of a multirotor is also used in [34] where wind estimation assuming a slowly varying wind field relative to the aircraft is presented using a KF along with a parameter identification method to estimate the drag model of the aircraft. Xiang *et al.* present quadcopter-based wind estimation using a KF where estimates were obtained experimentally with the quadcopter in steady flight in a straight line and in a steady hover

[36]. The estimates obtained in hover were in closer agreement with measurements obtained using digital anemometers attached to masts in the test environment.

Model-based wind estimation methods using either KFs or EKFs are applied in [34, 35, 36, 37, 39, 40, 42, 43] where both filters rely on linearizing the nonlinear system equations. The KF relies on linearization of the nonlinear equations of motion about a nominal state. The EKF requires linearizing the nonlinear system at each time step about the current best estimate of the state. Petrich *et al.* use a two-state KF that initially generates a GNSS-based position estimate and then estimates orientation, airspeed, angular rate, and 3D wind velocity based on measurements from an IMU and an air data sensor under the assumption of a constant wind field [37]. Langelaan *et al.* assume a polynomial structure for the wind to simplify the parameter estimation method which allows implementation of a KF for state estimation [35]. The motivation for obtaining wind estimates is to be able to query the wind field in real-time to facilitate autonomous dynamic soaring. Torgesen *et al.* estimate steady and turbulent air wake stream components using an error-state Kalman filter for a hexacopter tethered behind a cruising vessel [13]. Chen *et al.* design an invariant EKF (denoted "IEKF" in Table 3.1) that leverages the invariant dynamics of quadcopter kinematics and translational dynamics to obtain estimates with errors that are realistic with respect to the symmetries exhibited by the system [39]. Tian *et al.* propose an estimation method modeling the wind as a random walk process using two EKFs where the first EKF estimates AoA and AoS and the second estimates air-relative velocity, orientation, and wind velocity using measurements from GNSS, IMU, and a Pitot probe [43]. In [42], Sun *et al.* propose wind estimation, where the wind is modeled as a random walk process, using a tail-sitter UAV that is able to operate in three flight regimes: rotary, transitional, and wing-borne flight. They use the cascaded EKF structure from [40]. Pappu *et al.* use an EKF to estimate wind gusts with a quadcopter in hover using only GNSS, IMU, and control actuation sensors assuming that

gusts can be represented by filtered white noise [41]. Lie *et al.* present a wind estimation method that relies only on GNSS and inertial navigation system (INS) measurements using a cascaded EKF structure under the assumption of small AoA and constant thrust [40].

The invariant EKF is used for model-based wind estimation in [48, 49, 50, 51, 52, 53]. The invariant EKF does not require analytical linearization of the nonlinear equations of motion about a nominal state. Condomines *et al.* present wind estimation and aircraft parameter identification based on flight experiments using a fixed-wing UAV where a square root invariant EKF-based approach is proposed for simultaneous aircraft air-relative velocity and wind velocity estimation assuming the spatial gradient of the wind field to be zero [48]. Larrabee *et al.* investigate the use of a stand-alone invariant EKF and a cooperative UKF for a leader-follower formation of fixed-wing aircraft where the follower senses the wake of the leader [50]. Rhudy *et al.* estimate wind velocity and acceleration components assuming the wind acceleration is a random walk process using a UKF in [52] and in [53] UKF-based wind estimates are compared under two different models for the random wind variations: (1) a random walk and (2) a Gauss-Markov process. Lee *et al.* use a square-root UKF for wind and aircraft state estimation where the aircraft is exposed to time-varying prevailing wind and turbulence modeled using the Dryden turbulence model and both the wind velocity and its derivative are estimated [51]. Cooper *et al.* perform quadcopter wind estimation with a UKF where the motivation is to use wind estimates in a source localization algorithm in two scenarios: (1) a hovering quadcopter and (2) a quadcopter that hovers for 10 seconds then moves to a sequence of two waypoints, loitering at each for 10 seconds [49]. In this work, a flight dynamic model is identified which incorporates rotor blade flapping motion using blade element theory.

Optimization techniques such as multi-objective optimization and model predictive static programming (MPSP) are also employed in model-based wind estimation in [70] and [61, 73],

respectively. In [70], Velasco-Carrau *et al.* use multi-objective optimization (MO) for wind estimation and aircraft model identification where an aircraft model structure is provided and MO provides wind speed estimates that are used in model structure determination to correct airspeed-dependent terms and minimize the defined cost functions. Hong *et al.* use generalized MPSP (G-MPSP) in [73] and tracking MPSP (T-MPSP) in [61] to estimate 3D wind without requiring any airspeed measurements. The G-MPSP approach in [73] considers the wind as a virtual input to the model and uses measurements from a previous finite horizon of 0.2 seconds to reduce terminal errors using the measured and predicted states. In [61], the wind vector is estimated by considering it to be an input to the aircraft model that results in reduced error between the aircraft's measured and predicted kinematic states.

Other model-based wind estimation methods include frequency-based wind gust estimation using a nonlinear disturbance observer [55], wind gust estimation with a quadrotor in a quasi-hover using an unknown input observer (UIO) [60], direct computation of the wind velocities [62], wind velocity estimation using Gaussian process regression (GPR) [63], estimating time-varying wind parameters from quadrotor data using finite time estimation (FTE) [67], and wind velocity and aircraft aerodynamic coefficient estimation using a moving horizon estimator (MHE) [30].

Model-free Methods

Wind estimation methods that do not require a flight dynamic model are referred to as model-free methods. Model-free methods typically rely on airspeed measurements from a Pitot probe and inertial velocity from GNSS. These methods are attractive because they do not require a lengthy model identification effort. However, model-free estimation methods typically require persistent excitation of the aircraft motion to resolve the air-relative velocity from the scalar airspeed measurement provided by the Pitot probe. Model-free wind estimation with UAVs is used in [38, 44, 45, 46, 71].

The combination of operational sensors available on an aircraft guides the selection of a wind estimation approach. The different combinations of operational sensor suites and wind estimation methods described in the literature reviewed here are shown in Table 3.2. Model-free wind estimation methods typically rely only on GNSS and Pitot probe data, as described in [44] and [38]. Cho *et al.* describe model-free wind estimation where the aircraft is equipped with a single GNSS antenna/receiver and a Pitot probe [44]. They assume a constant 2D wind field and enforce persistent excitation of the aircraft motion, in the form of banking turns and circling maneuvers, to resolve the air-relative velocity and the wind velocity using an EKF. Balmer *et al.* adopt a KF to obtain wind estimates [38]. They assume a constant wind field and provide their algorithm with pseudo-measurements of AoA and AoS to calculate the air-relative velocity. These pseudo-measurements are the equilibrium values of AoA and AoS for the aircraft, assuming that pitch and yaw stability ensures only small deviations from these equilibrium values. This approach allows the authors to remove the requirement for persistent excitation or attitude variations typically seen in model-free wind estimation.

In addition to GNSS and Pitot probe measurements, instrumentation for model-free wind estimation can include IMU, magnetometer, and/or ADS data. Reference [45] describes wind estimation from data obtained using a fixed-wing UAV equipped with a multi-hole Pitot probe, an IMU, and a GNSS receiver. The authors compare the accuracy of estimates obtained when incorporating the air-relative velocity measurements in the filter with the accuracy of estimates obtained when omitting flow sensor data and using persistent excitation. Zhang *et al.* require GNSS, IMU, Pitot probe, and barometric pressure measurements for online calibration of a Pitot probe and wind field estimation with a quadcopter in hovering flight [46]. Witte *et al.* use GNSS, IMU, magnetometer, and a multihole Pitot probe data from a fixed-wing UAV to obtain wind velocity estimates where the GNSS measurements provide inertial velocity and the multihole Pitot probe provides the three components of air-

Table 3.2: Existing wind estimation formulations and operational sensor suite, where * indicates reference also uses linear optical sensor arrays, ** indicates reference also uses control inputs, *** indicates reference also uses a range sensor, † indicates reference uses a barometer and vision-based prose, and ‡ indicates reference also uses a multi-hole Pitot probe.

Sensors	Model-based	Model-free	Combined
IMU only	Segales *et al.* [10]		
IMU and magnetometer	Palomaki *et al.* [66]		
GNSS and Pitot probe	Hattenberger *et al.* [34] Hong *et al.* [61]	Balmer *et al.* [38] Cho *et al.* [44]	
GNSS and IMU	Cooper *et al.*** [49] Pappu *et al.*** [41] Phelps *et al.* [14] Salazar *et al.* [68] Sun *et al.* [42] Tian *et al.* [43] Torgesen *et al.*† [13] Velasco-Carrau *et al.*** [70] Xiang *et al.*[36]		
GNSS, IMU, and magnetometer	Chen *et al.* [39] Perozzi *et al.* [67] Kumar *et al.** [12]		
GNSS, IMU, barometer, and magnetometer	González-Rocha *et al.* [56, 57, 58] Neumann *et al.* [65] Shelekhov *et al.* [69]		
GNSS, IMU, and Pitot probe	Condomines *et al.* [48] Lie *et al.* [40]	Rautenberg *et al.* [45]	Benders *et al.* [15] Borup *et al.* [59] Wenz *et al.* [30, 47]
GNSS, IMU, Pitot probe, and magnetometer	Azid *et al.* [60] Langelaan *et al.* [35, 62] Marinescu *et al.* [63] Meier *et al.* [64]	Witte *et al.*‡ [71] Zhang *et al.* [46] (w/ barometer)	
GNSS, IMU, and ADS	Larrabee *et al.* [50]*** Petrich *et al.* [37] Rhudy *et al.* [52, 53, 54]	Rhudy *et al.* [54]	
GNSS, IMU, ADS, and magnetometer	Lee *et al.* [51]		

relative velocity. These measurements, along with an attitude estimate from the IMUand magnetometer, allow one to solve the wind triangle for the wind velocity [71]. In [54], Rhudy *et al.* present four different formulations for wind estimation using a UKF with two model-free methods, one of which is based on the work in [44], and two model-based methods. They

use GNSS, IMU, and ADS measurements in their estimation algorithms.

Combined Methods

In the literature reviewed here, the combined wind estimation methods used either EKFs [47], deterministic observers [59], or moving horizon estimators [15, 30]. Wenz *et al.* use an EKF with GNSS, IMU, and Pitot probe measurements to obtain steady wind and turbulent fluctuation estimates [47]. Attitude changes are required during the flight to maintain observability. Borup *et al.* implement a nonlinear observer for model-free wind estimation, eliminating the persistent excitation requirement by incorporating a simple aerodynamic model that is updated using propeller speed and Pitot probe measurements [59]. The authors note that the simple, assumed aerodynamic model introduces errors into the estimates. Benders *et al.* use a moving horizon estimator and combine wind velocity-based path planning with wind velocity estimation where wind is modeled using the Dryden turbulence model [15]. This method requires aircraft attitude changes during the flight to maintain observability. It is considered a combined method as the aerodynamic coefficients of the aircraft are determined online rather than beforehand. Wenz *et al.* [30] model the wind using the Dryden turbulence model and obtain wind velocity and turbulence estimates using a moving horizon estimator where persistent excitation is required to distinguish between changes in aerodynamic coefficients and the wind velocity.

3.2 Symmetry-Preserving Observers

The application of geometric mechanics and symmetry in the field of controls emerged when researchers sought to exploit the geometric properties of systems to develop and enhance control methodologies. Common textbooks on geometric mechanics and symmetry include [20] and [21]. In [22], Bullo and Lewis provide an introduction to mechanics and symmetry

before an in-depth discussion on geometric control of mechanical systems. Geometric control of nonlinear systems began to gain traction in the 1980s leading into the 1990s with work such as [74] and [75] where control of left-invariant systems on Lie groups and geometric methods for robust stabilization of autonomous underwater vehicles are considered, respectively. As geometric mechanics found a role in control theory, its use in observer theory was not discussed until the early 2000s when Aghannan and Rouchon introduced invariant asymptotic observers in 2002 [76]. This was followed by the development of an intrinsic observer for a class of Lagrangian systems in [77] where the notion of a state observer invariant to a change of the configuration coordinates is established. Mahoney *at al.* later designed two complementary filters on the special orthogonal group $SO(3)$ for application to attitude estimation in UAVs.

In [26], Bonnabel *et al.* develop symmetry-preserving observers where a constructive method is presented on how to leverage the symmetries of a dynamic system to produce estimates of the system state. Mahony *et al.* describe observers for kinematic systems with symmetry in [78] where nonlinear observer design is presented for finite-dimensional equivariant kinematics of mechanical systems. Symmetry-preserving observers inspired the development of an invariant EKF and an invariant UKF. Barrau *et al.* prove that the invariant EKF is an asymptotically stable observer for a class of nonlinear systems in [79] and explain that the error equation is autonomous and the calculated Kalman gain is independent of the system trajectory in [80]. In [81], Bonnabel uses the invariant EKF for attitude estimation of a flying rigid body. In [82], Bonnabel *et al.* use the invariant EKF for a velocity-aided attitude filtering problem and compare the results to estimation using a multiplicative EKF. References [81] and [82] use the invariant EKF for attitude estimation of flying rigid bodies using kinematic equations and only considering the body's translational velocity. The invariant EKF has also been applied to underwater localization in [83], where the Potokar *et*

al. note that the invariant EKF exhibited faster convergence when compared to a conventional EKF. Design of the invariant EKF for nonlinear systems subject to dynamic additive disturbances is presented in [84]. An advantage of the invariant EKF is that it uses a correction term based on an adapted invariant output error whereas a conventional EKF uses a linear correction term using a linear output error. The gain matrix in the invariant EKF algorithm is also calculated based on the invariant state error as opposed to a linear state error. Reference [82] remarks that leveraging the symmetries of the dynamic system using the invariant EKF results in constant state and output matrices on a larger subset of the state space when compared to the EKF, indicating that, in general, the invariant EKF has stronger convergence guarantees for a larger family of trajectories. The invariant UKF is described in [85] where using the principles of a UKF in an invariant framework Condomines *et al.* developed a compatibility condition on the observation equations to construct them in an invariant fashion. The invariant UKF, also referred to as the π-invariant UKF as the compatibility condition is a nonlinear function denoted by π, is applied to the aided inertial navigation problem for a mini remotely piloted aerial system in [86] and attitude estimation using quadrotor flight data in [87].

The application of the invariant EKF to wind estimation was first demonstrated by Chen *et al.* in [39] using a quadrotor model where aircraft translational dynamics are considered. Quadcopter-based wind estimation using the invariant EKF is also discussed in [88], where invariance of the dynamics using different thrust models is established. The present work is the first application of the invariant EKF to wind estimation using small, fixed-wing UAVs where the full translational and rotational dynamics of the aircraft are considered.

Chapter 4

Aircraft Equations in Wind

Indirect wind estimation requires the aircraft dynamic and kinematic equations in wind and a suitable estimation algorithm. The extended state of a UAV, which includes the wind velocity state, can be used in an estimation algorithm to estimate the aircraft state and the wind state. A description of the aircraft equations of motion in wind is given in Section 4.1. Common estimation algorithms such as a determinisitc (or Luenberger) observer, Kalman filter, extended Kalman filter, and unscented Kalman filter are provided in Section 4.2.

4.1 Aircraft Equations of Motion

Wind estimation schemes that use measurements obtained from UAVs are often informed by assumptions made about the wind field. For example, a model-based estimator might assume that the wind velocity is steady and uniform so that wind estimates are only updated based on measurements. Or the estimator might assume that the wind velocity varies as a random walk. For example, one may be using a UAV to estimate the wind velocity at a certain point in space and time, without the need to identify the wind's spatial and temporal gradients, so they might make the simplifying assumption that the wind velocity is not changing, *i.e.,* its time derivative is zero or is varying as a purely random process. Other applications of wind estimation may be to characterize a particular flow field, such as a ship's air wake, requiring temporal and spatial gradients in the wind field model.

Wind velocity is modeled as a vector-valued random process. It can be decomposed into (i) a deterministic mean value that varies slowly in time and space and (ii) random time- and space-varying fluctuations from this mean value.

Let $\boldsymbol{W}(\boldsymbol{X}, t)$ denote the wind field at the inertial position $\boldsymbol{X} = [x, y, z]^{\mathrm{T}}$ and time t. Then

$$\boldsymbol{W}(\boldsymbol{X}, t) = \bar{\boldsymbol{W}}(\boldsymbol{X}, t) + \tilde{\boldsymbol{W}}(\boldsymbol{X}, t) \tag{4.1}$$

where $\bar{\boldsymbol{W}}(\boldsymbol{X}, t)$ is the slow varying deterministic mean wind velocity vector and $\tilde{\boldsymbol{W}}(\boldsymbol{X}, t) = [\tilde{W}_x, \tilde{W}_y, \tilde{W}_z]^{\mathrm{T}}$ is the random fluctuation.

Associated with any given point $\boldsymbol{X}$ and time t, there is a 3×3 correlation matrix $\boldsymbol{R}(\boldsymbol{X}, t, \boldsymbol{\zeta}, \tau)$ defined as the ensemble average of the outer product of $\tilde{\boldsymbol{W}}(\boldsymbol{X}, t)$ with $\tilde{\boldsymbol{W}}(\boldsymbol{X}+\boldsymbol{\zeta}, t+\tau)$, where $\boldsymbol{\zeta}$ and τ are the spatial and temporal correlation variables, respectively. The components of the correlation matrix are

$$R_{ij}(\boldsymbol{X}, t, \boldsymbol{\zeta}, \tau) = < \tilde{W}_i(\boldsymbol{X}, t)\tilde{W}_j(\boldsymbol{X} + \boldsymbol{\zeta}, t + \tau) > \tag{4.2}$$

for $i, j \in \{x, y, z\}$, where $< \cdot, \cdot >$ denotes the ensemble average.

The component functions R_{ij} provide an incomplete description of the wind turbulence, modeled as a random process, but it is common to characterize turbulence using the information contained in R_{ij}. The functional form of these component functions and the corresponding parameter values depend on meteorological conditions, terrain, and other factors. Atmospheric turbulence is often well characterized by one or more of the following assumptions [89, Ch. 13].

Assumption 1. Common Assumptions Concerning Atmospheric Turbulence

(a) The joint probability density functions underlying the correlation functions (4.2) are

Gaussian.

(b) The process is stationary: R_{ij} does not depend on time t for $i, j \in \{x, y, z\}$.

(c) The process is homogeneous: R_{ij} does not depend on position $\boldsymbol{X}$ for $i, j \in \{x, y, z\}$.

(d) The process is isotropic: R_{ij} does not depend on the orientation of the frame in which the wind vector is defined. Equivalently, the mean-square velocity components are equal in every direction: $\langle \tilde{W}_x^2 \rangle = \langle \tilde{W}_y^2 \rangle = \langle \tilde{W}_z^2 \rangle = \sigma^2$.

At low altitudes, atmospheric turbulence varies with height, thus Assumption 1d does not hold. The rate of change of the wind velocity as seen by a particle moving along a trajectory $\boldsymbol{X}(t)$ is

$$\frac{d}{dt}\boldsymbol{W}(\boldsymbol{X}, t) = \left(\frac{\partial}{\partial t}\bar{\boldsymbol{W}}(\boldsymbol{X}, t) + \nabla\bar{\boldsymbol{W}}(\boldsymbol{X}, \boldsymbol{t}) \cdot \frac{d\boldsymbol{X}}{dt}\right) + \left(\frac{\partial}{\partial t}\tilde{\boldsymbol{W}}(\boldsymbol{X}, t) + \nabla\tilde{\boldsymbol{W}}(\boldsymbol{X}, t) \cdot \frac{d\boldsymbol{X}}{dt}\right) \tag{4.3}$$

where ∇ denotes the gradient with respect to three-dimensional position.

The nature of the aircraft's flight can produce additional simplifications to Eq. (4.3). For fixed-wing aircraft flying straight and level at a constant altitude and speed, the position of the aircraft typically changes much faster than the spatial profile of the velocity fluctuations. In this case, the turbulent fluctuations can be treated as a frozen pattern advecting with the mean wind velocity $\bar{\boldsymbol{W}}$ [89, Ch. 13]. This assumption is referred to as Taylor's frozen turbulence hypothesis. Kaimal and Finnigan remark that Taylor's hypothesis can be adopted for any *in situ* sensor as it is assumed that the turbulent eddies "change imperceptibly" as they are convected by the mean wind past the sensor [90, pg. 33]. While turbulence is neither frozen nor transported at mean wind speeds, the lifetime of an eddy is long compared to the travel time across a sensor. Experimental investigations find good agreement between atmospheric measurements made with moving and stationary probes when it is assumed

that eddies are convected by the mean wind without deforming. Thus, Taylor's hypothesis can be adopted for static or slowly moving objects, such as a hovering rotary-wing aircraft, as well as for fixed-wing airplanes in fast, forward flight through turbulence. Summarizing these points, one may adopt one or more of the following assumptions.

Assumption 2. (a) Steady Mean Wind: The mean wind velocity does not vary with time: $\frac{\partial}{\partial t}\bar{\boldsymbol{W}}(\boldsymbol{X},t) = \boldsymbol{0}$, thus $\bar{\boldsymbol{W}}(\boldsymbol{X},t) = \bar{\boldsymbol{W}}(\boldsymbol{X})$.

(b) Uniform Mean Wind: The mean wind velocity does not vary with position: $\nabla\bar{\boldsymbol{W}}(\boldsymbol{X},t) = \boldsymbol{0}$, thus $\bar{\boldsymbol{W}}(\boldsymbol{X},t) = \bar{\boldsymbol{W}}(t)$.

(c) Frozen Turbulence (Taylor's hypothesis): Random fluctuations from the mean wind velocity vary only in space: $\frac{\partial}{\partial t}\tilde{\boldsymbol{W}}(\boldsymbol{X},t) = \boldsymbol{0}$, so that $\tilde{\boldsymbol{W}}(\boldsymbol{X},t) = \tilde{\boldsymbol{W}}(\boldsymbol{X})$.

Assumptions 2a and 2b together imply that $\bar{\boldsymbol{W}}$ is a constant vector. In reality, the mean wind will always vary over a flight. If one adopts a steady, uniform flow model for the wind estimation problem, these variations must be captured by measurement updates in the model-based estimator. More commonly in wind estimation, the dynamics of the total wind velocity are assumed to be driven by Gaussian white noise. For the case characterized by Assumption 2, one has

$$\frac{d}{dt}\boldsymbol{W}(\boldsymbol{X},t) = \frac{d}{dt}\left(\bar{\boldsymbol{W}} + \tilde{\boldsymbol{W}}(\boldsymbol{X})\right) = \nabla\tilde{\boldsymbol{W}}(\boldsymbol{X})\dot{\boldsymbol{X}} = \tilde{\boldsymbol{w}}_W \tag{4.4}$$

where the stochastic wind velocity fluctuation $\tilde{\boldsymbol{W}}$ is assumed to be a Wiener process whose generalized derivative $\tilde{\boldsymbol{w}}_W$ is continuous-time white noise [91, Ch. 3]. In other words, the perturbations in wind velocity from its steady, uniform mean value are modeled as a random-walk process. Note that $\tilde{\boldsymbol{w}}_W$ captures the combined effect of the variability in the frozen turbulence field and the velocity of the aircraft through that flow field. The model (4.4) is a

commonly used representation of fluctuations from a constant, uniform mean wind, though a given wind estimation algorithm may or may not incorporate this representation.

The attitude kinematics and dynamics of a UAV flying in wind are

$$\dot{\boldsymbol{X}} = \boldsymbol{R}_{\mathrm{IB}}\boldsymbol{v}_r + \boldsymbol{V}_w \tag{4.5a}$$

$$\dot{\boldsymbol{R}}_{\mathrm{IB}} = \boldsymbol{R}_{\mathrm{IB}}\boldsymbol{\omega}^{\times} \tag{4.5b}$$

$$\dot{\boldsymbol{v}}_r = \boldsymbol{v}_r \times \boldsymbol{\omega} + \frac{1}{m}\boldsymbol{F}_A + \boldsymbol{R}_{\mathrm{IB}}^{\mathrm{T}}\boldsymbol{g} - \boldsymbol{R}_{\mathrm{IB}}^{\mathrm{T}}\tilde{\boldsymbol{w}}_W \tag{4.5c}$$

$$\dot{\boldsymbol{\omega}} = \boldsymbol{\omega} \times \boldsymbol{I}^{-1}\boldsymbol{\omega} + \boldsymbol{I}^{-1}\boldsymbol{M}_A \tag{4.5d}$$

$$\dot{\boldsymbol{V}}_w = \tilde{\boldsymbol{w}}_W \tag{4.5e}$$

where $\boldsymbol{X} = (X, Y, Z)^{\mathrm{T}} \in \mathbb{R}^3$ describes the position of the UAV expressed in the inertial frame, $\boldsymbol{v}_r = (v_{r,x}, v_{r,y}, v_{r,z})^{\mathrm{T}} \in \mathbb{R}^3$ is the air-relative velocity vector expressed in the body-fixed frame, $\boldsymbol{\omega} = (p, q, r)^{\mathrm{T}} \in \mathbb{R}^3$ is the angular rate vector of the aircraft expressed in the body frame, and $\boldsymbol{V}_w = (V_{w,x}, V_{w,y}, V_{w,z})^{\mathrm{T}} \in \mathbb{R}^3$ is the velocity of the wind expressed in the inertial frame. The aerodynamic force and moment of the aircraft are denoted by $\boldsymbol{F}_A$ and $\boldsymbol{M}_A$, respectively, and $\boldsymbol{g} = (0, 0, g)^{\mathrm{T}}$ where g is the gravitational acceleration. The rotation matrix $\boldsymbol{R}_{\mathrm{IB}} \in SO(3)$ maps free vectors expressed in the body-fixed frame to the inertial frame and is given by

$$\boldsymbol{R}_{\mathrm{IB}} = \begin{pmatrix} \cos\theta\cos\psi & \cos\psi\sin\theta\sin\phi - \cos\phi\sin\psi & \cos\psi\sin\theta\cos\phi + \sin\phi\sin\psi \\ \cos\theta\sin\psi & \sin\phi\sin\theta\sin\psi + \cos\phi\cos\psi & \sin\theta\cos\phi\sin\psi - \sin\phi\cos\psi \\ -\sin\theta & \cos\theta\sin\phi & \cos\theta\cos\phi \end{pmatrix} \tag{4.6}$$

The matrix $\boldsymbol{R}_{BI}$ that maps vectors from the inertial frame to the body-fixed frame is $\boldsymbol{R}_{BI} = \boldsymbol{R}_{\mathrm{IB}}^{-1} = \boldsymbol{R}_{\mathrm{IB}}^{\mathrm{T}}$. The notation $(\cdot)^{\times}$ in Eq. (4.5b) denotes the cross-product equivalent matrix of a 3×1 vector.

The system (4.5) can be written in first-order form (forgiving the abuse of notation of concatenating vector differential equations with matrix differential equations) as

$$\dot{\boldsymbol{x}} = \boldsymbol{f}(\boldsymbol{x}, \boldsymbol{u}) = \begin{pmatrix} \boldsymbol{R}_{\mathrm{IB}} \boldsymbol{v}_r + \boldsymbol{V}_w \\ \boldsymbol{R}_{\mathrm{IB}} \boldsymbol{\omega}^{\times} \\ \boldsymbol{v}_r \times \boldsymbol{\omega} + \frac{1}{m} \boldsymbol{F}_A + \boldsymbol{R}_{IB}^{\mathrm{T}} \boldsymbol{g} - \boldsymbol{R}_{\mathrm{IB}}^{\mathrm{T}} \tilde{\boldsymbol{w}}_W \\ \boldsymbol{\omega} \times \boldsymbol{I}^{-1} \boldsymbol{\omega} + \boldsymbol{I}^{-1} \boldsymbol{M}_A \\ \tilde{\boldsymbol{w}}_W \end{pmatrix} \tag{4.7}$$

where the state is defined as $\boldsymbol{x} = (\boldsymbol{X}^{\mathrm{T}}, \boldsymbol{R}_{IB}^{\mathrm{T}}, \boldsymbol{v}_r^{\mathrm{T}}, \boldsymbol{\omega}^{\mathrm{T}}, \boldsymbol{V}_w^{\mathrm{T}})^{\mathrm{T}}$ (again, the reader is asked to forgive the abuse of notation of mixing vector and matrix states) and the input is $\boldsymbol{u} = (\boldsymbol{F}_A^{\mathrm{T}}, \boldsymbol{M}_A^{\mathrm{T}})^{\mathrm{T}}$.

4.2 Estimation Methods

The selection of an estimation algorithm is guided by aircraft model assumptions and computational considerations. This section reviews common model assumptions and estimator choices described in the literature about wind estimation using UAVs and identifies some advantages and disadvantages of these model assumptions and estimator choices.

Model-based wind estimation requires a dynamic model of an aircraft and a wind model, which is chosen to be the system (4.5), a continuous-time, nonlinear system. Estimation algorithms that incorporate a system dynamic model, however, are typically implemented in discrete time. A continuous-time system such as (4.5) may be discretized by implementing a zero-order hold, for example, on the system inputs. Then, a numerical integration scheme such as Euler or Runge-Kutta integration may be used to obtain model updates. In addition to being implemented in discrete time, many observer structures assume the system dynamics

are linear. Equations (4.5) may be linearized about a given state and input, such as a nominal steady motion or just the most current state and input values, however, the domain in which this model is an accurate approximation of (4.5) will be limited. An overview of the observers and algorithms is given below.

4.2.1 Deterministic Observer

In cases where measurement noise is absent from a dynamic system, one can construct a Luenberger observer [92] to estimate the states of a discrete-time dynamic system as done in [56, 57, 58] for wind estimation. The dynamic model of a linear time-varying system in the absence of process and measurement noise is

$$\boldsymbol{x}(i) = \boldsymbol{A}(i-1)\boldsymbol{x}(i-1) + \boldsymbol{B}(i-1)\boldsymbol{u}(i-1) \tag{4.8a}$$

$$\boldsymbol{y}(i-1) = \boldsymbol{C}(i-1)\boldsymbol{x}(i-1) \tag{4.8b}$$

where $\boldsymbol{x}(i) \in \mathbb{R}^n$ denotes the state vector, $\boldsymbol{u}(i) \in \mathbb{R}^m$ is the vector of inputs, $\boldsymbol{y}(i) \in \mathbb{R}^p$ is the vector of outputs, $\boldsymbol{A}(i) \in \mathbb{R}^{n\times n}$ is the state matrix, $\boldsymbol{B}(i) \in \mathbb{R}^{n\times m}$ is the control input matrix, and $\boldsymbol{C}(i) \in \mathbb{R}^{p\times n}$ is the output matrix. (The output model in (4.8) includes no direct throughput of the input $\boldsymbol{u}(i)$.) The integer $i \in \{1, \ldots, N\}$ denotes the sample index up to some total number of measurements N. For a constant sample time Δt, the time that has elapsed since time $t = 0$ is $(i-1)\Delta t$. In order to estimate the state of this linear system, the pair $(\boldsymbol{A}(i), \boldsymbol{C}(i))$ must be observable. For the pair to be observable on the finite time interval from time step $i = 0$ to $i = N$, the matrix

$$\mathcal{O}(0, N) = \sum_{i=0}^{N} \overline{\boldsymbol{\Phi}}^T(i, 0)\overline{\boldsymbol{C}}^T(i)\boldsymbol{C}(i)\boldsymbol{\Phi}(i, 0)$$

must be positive-definite [93]. Here, $\boldsymbol{\Phi}(i,0)$ is the discrete-time state transition matrix

$$\boldsymbol{\Phi}(i,0) = \prod_{j=0}^{i-1} \boldsymbol{A}(j)$$

If the pair $(\boldsymbol{A}(i), \boldsymbol{C}(i))$ is observable, then the measurements can be used to reconstruct the state using the Luenberger observer defined by

$$\hat{\boldsymbol{x}}(i) = \boldsymbol{A}(i-1)\hat{\boldsymbol{x}}(i-1) + \boldsymbol{L}(i-1)(\boldsymbol{y}(i-1) - \hat{\boldsymbol{y}}(i-1)) + \boldsymbol{B}(i-1)\boldsymbol{u}(i-1) \tag{4.9a}$$

$$\hat{\boldsymbol{y}}(i-1) = \boldsymbol{C}(i-1)\hat{\boldsymbol{x}}(i-1) \tag{4.9b}$$

where $\hat{\boldsymbol{x}}$ is the state estimate and $\hat{\boldsymbol{y}}$ is the corresponding output. For a well-designed observer, the observer gain $\boldsymbol{L}(i)$ is chosen such that the observer error $\boldsymbol{e}(i) = \hat{\boldsymbol{x}}(i) - \boldsymbol{x}(i)$ converges to zero as i approaches infinity, so that the estimate $\hat{\boldsymbol{x}}(i)$ approaches the true state $\boldsymbol{x}(i)$. The observer error can be rewritten as $\boldsymbol{e}(i) = (\boldsymbol{A}(i-1) - \boldsymbol{L}(i-1)\boldsymbol{C}(i-1))\boldsymbol{e}(i-1)$ using (4.8) and (4.9). The origin is a uniformly exponentially stable equilibrium of the observer error equation if and only if a symmetric matrix sequence $\boldsymbol{Q}(i) \in \mathbb{R}^{n\times n}$ exists for all i such that $\eta\mathbb{I} \preceq \boldsymbol{Q}(i) \preceq \rho\mathbb{I}$ and

$$(\boldsymbol{A}(i) - \boldsymbol{L}(i)\boldsymbol{C}(i))^T\boldsymbol{Q}(i+1)(\boldsymbol{A}(i) - \boldsymbol{L}(i)\boldsymbol{C}(i)) - \boldsymbol{Q}(i) \preceq \nu\mathbb{I}$$

for some finite positive constants η, ρ, and ν [94]. The matrix sequences $\boldsymbol{L}(i)$ and $\boldsymbol{Q}(i)$ must be chosen to satisfy the above conditions; see Chapters 23 and 29 of [94] for more details about stability and state estimation for discrete-time linear, time-varying systems.

Figure 4.1 shows the Luenberger observer divided into initialization, model-based prediction, and measurement-based correction steps. As stated earlier, $\hat{\boldsymbol{x}}$ and $\hat{\boldsymbol{y}}$ denote the estimated state and output in Figure 4.1. For the system (4.8), the state $\boldsymbol{x}$ and output $\boldsymbol{y}$ are deter-

ministic. In the following sections, concerning the KF, EKF, and UKF, the state $\boldsymbol{x}$ and the output $\boldsymbol{y}$ will be subject to random inputs. For these systems, the notation $\hat{\boldsymbol{x}}$ and $\hat{\boldsymbol{y}}$ will indicate conditional probabilities, as defined and discussed in Section 4.2.2.

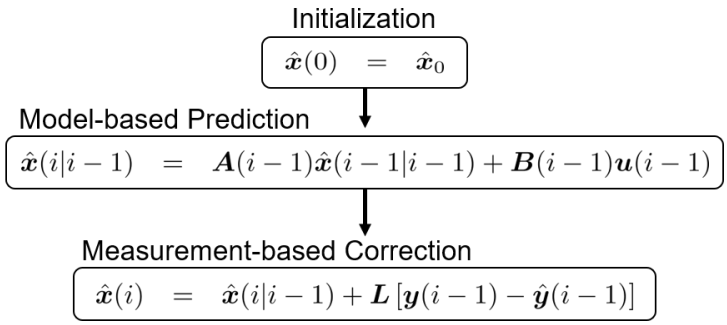

Figure 4.1: The Luenberger observer split into initialization, model-based prediction, and measurement-based correction steps where $\hat{\boldsymbol{x}}_0$ is the initial state estimate. See [92], for example.

4.2.2 Kalman Filter

The KF is used to estimate the state of a non-deterministic, discrete-time, linear dynamic system. The general form of this system follows, including equations for both the output $\boldsymbol{y}$ and the (noisy) measurement $\boldsymbol{z}$ and omitting direct throughput from both:

$$\boldsymbol{x}(i) = \boldsymbol{A}(i-1)\boldsymbol{x}(i-1) + \boldsymbol{B}(i-1)\boldsymbol{u}(i-1) + \boldsymbol{\Gamma}(i-1)\tilde{\boldsymbol{w}}(i-1) \tag{4.10a}$$

$$\boldsymbol{y}(i) = \boldsymbol{C}(i)\boldsymbol{x}(i) \tag{4.10b}$$

$$\boldsymbol{z}(i) = \boldsymbol{y}(i) + \tilde{\boldsymbol{v}}(i) \tag{4.10c}$$

where $\boldsymbol{\Gamma}(i) \in \mathbb{R}^{n\times q}$ is the disturbance input matrix, $\tilde{\boldsymbol{w}}(i) \in \mathbb{R}^q$ is the process noise vector, $\boldsymbol{z}(i) \in \mathbb{R}^p$ is the measurement vector, and $\tilde{\boldsymbol{v}}(i) \in \mathbb{R}^p$ is the vector of measurement noise. For a KF, the measurement and process noise are assumed to be Gaussian, zero mean, white noise sequences [95]. The random forcing $\tilde{\boldsymbol{w}}$ makes the system non-deterministic. When

estimating the states of a non-deterministic system, we define the state estimate $\hat{\boldsymbol{x}}$ at a time step i as the expected value of the random variable $\boldsymbol{x}$ at i given the measurement $\boldsymbol{z}$ at $k \leq i$. This conditional probability is denoted

$$\hat{\boldsymbol{x}}(i|k) = E\{\boldsymbol{x}(i)|\boldsymbol{z}(k)\}$$

The state estimate $\hat{\boldsymbol{x}}$ has an associated covariance

$$\boldsymbol{X}(i|k) = E\{[\boldsymbol{x}(i) - \hat{\boldsymbol{x}}(i|k)][\boldsymbol{x}(i) - \hat{\boldsymbol{x}}(i|k)]^T|\boldsymbol{z}(k)\}$$

for $k \leq i$. The steps of Kalman filtering, as described in [95], are shown in Figure 4.2. The steps are grouped into three categories: initialization, prediction, and correction. The matrix $\boldsymbol{P}_0$ is the covariance of the initial state estimate $\hat{\boldsymbol{x}}(0|0)$. The covariance matrix sequences $\boldsymbol{Q}(i)$ and $\boldsymbol{R}(i)$ of the zero-mean, white, Gaussian process and measurement noise, respectively, are assumed to be known.

KF-based wind estimation is used in [34, 35, 36, 37, 38]. These estimation schemes assume the UAV is operating about some nominal trajectory, such as wings-level, constant-altitude flight for fixed-wing UAVs, or hovering flight for multirotors.

4.2.3 Extended Kalman Filter

The EKF is an adaptation of the KF's linear minimum mean square error estimation algorithm to nonlinear systems. In the EKF, nonlinear terms in the state and output equations are linearized at each time step about the current state estimate and input. A discrete-time

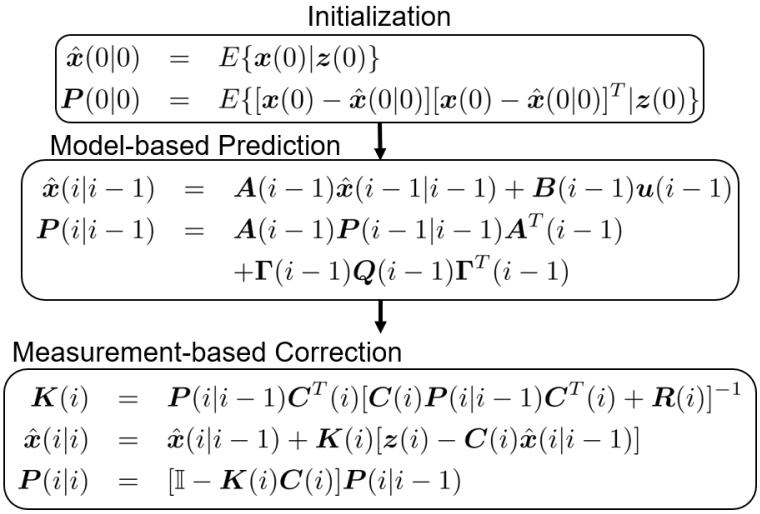

Figure 4.2: The KF algorithm based on the linear system (4.10) split into initialization, model-based prediction, and measurement-based correction steps, where $\mathbb{I}$ is the $n \times n$ identity matrix. See [95], for example.

nonlinear dynamic system takes the form

$$\boldsymbol{x}(i) = \boldsymbol{f}\Big(\boldsymbol{x}(i-1), \boldsymbol{u}(i-1), \tilde{\boldsymbol{w}}(i-1)\Big) \tag{4.11a}$$

$$\boldsymbol{y}(i) = \boldsymbol{h}\Big(\boldsymbol{x}(i)\Big) \tag{4.11b}$$

$$\boldsymbol{z}(i) = \boldsymbol{y}(i) + \tilde{\boldsymbol{v}}(i) \tag{4.11c}$$

where the vector fields $\boldsymbol{f}$ and $\boldsymbol{h}$ are assumed to contain once continuously differentiable nonlinear functions of the states, process noise, and inputs. The measurement and process noise are assumed to be Gaussian, zero mean, white noise sequences. Figure 4.3 shows the steps of EKF implementation for the system (4.11).

Wind estimation using an EKF is described in [39, 40, 42, 43, 44, 46, 47]. Since the EKF requires linearization at each time step, it can be computationally expensive and difficult to implement in real-time wind field estimation. Although the sequence of local linearizations can still fail to accurately capture the true nonlinear system behavior, the EKF relaxes the

requirement that the system state remain within a small neighborhood of a nominal state.

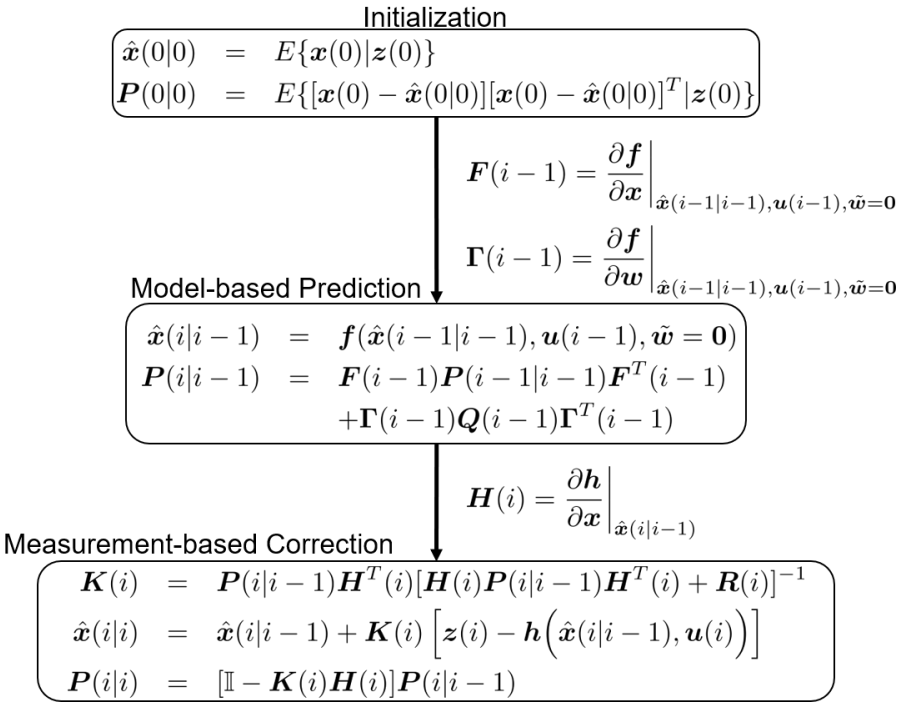

Figure 4.3: The EKF algorithm based on the nonlinear system (4.11) split into initialization, model-based prediction, and measurement-based correction steps with recursive linearization. See [95], for example.

4.2.4 Unscented Kalman Filter

The UKF provides another approach to nonlinear estimation for non-deterministic systems. First described by Julier and Uhlmann in [96], the UKF is based on the unscented transformation which is a method for approximating a random variable that undergoes a nonlinear transformation. The UKF does not require the computation of Jacobian matrices, which can make its implementation simpler [52]. For the system (4.11), the state vector $\boldsymbol{x}$ is a random variable, with expected value $\hat{\boldsymbol{x}}$ and covariance $\boldsymbol{P}_{xx}$, which is propagated through the nonlinear functions $\boldsymbol{f}$ and $\boldsymbol{h}$. The unscented transformation involves selecting n-dimensional vectors, called sigma points, around $\hat{\boldsymbol{x}}$ and then computing weights associated with each

sigma point based on the statistics of $\boldsymbol{x}$. For the system (4.11), the $2(n+q)+1$ sigma points are [97]:

$$
\begin{aligned}
\boldsymbol{\chi}_0 &= \hat{\boldsymbol{x}} \\
\boldsymbol{\chi}_j &= \hat{\boldsymbol{x}} + \sqrt{(n+p+q+\lambda)\boldsymbol{P}_{xx}}, && j = 1, \ldots, n \\
\boldsymbol{\chi}_j &= \hat{\boldsymbol{x}} - \sqrt{(n+p+q+\lambda)\boldsymbol{P}_{xx}}, && j = n+1, \ldots, 2n \\
\boldsymbol{\chi}_j &= \hat{\boldsymbol{x}} && j = 2n+1, \ldots, 2n+2q \\
\boldsymbol{\chi}_j^w &= \mathbf{0}, && j = 0, \ldots, 2n \\
\boldsymbol{\chi}_j^w &= \sqrt{(n+p+q+\lambda)\boldsymbol{Q}}, && j = 2n+1, \ldots, 2n+q \\
\boldsymbol{\chi}_j^w &= -\sqrt{(n+p+q+\lambda)\boldsymbol{Q}}, && j = 2n+q+1, \ldots, 2n+2q
\end{aligned}
$$

where $\lambda = \alpha^2(n+q+\kappa) - (n+q)$ is a sigma point scaling parameter. The scaling parameter λ depends on two other parameters, α and κ, where α is a small, positive value reflecting the spread of the sigma points (typically, $10^{-4} < \alpha < 1$) and κ is a secondary scaling parameter tuned to reduce prediction error [96]. For a Gaussian distribution, it is recommended to set $\kappa = 0$ [97].

The general steps of the UKF including initialization, prediction, and correction are provided in Figure 4.4, where each of the weights W_j^m and W_j^c for each vector of sigma points are

$$
\begin{aligned}
W_0^m &= \frac{\lambda}{n+q+\lambda} \\
W_0^c &= \frac{\lambda}{n+q+\lambda} + 1 - \alpha^2 + \beta \\
W_j^m &= W_j^c = \frac{1}{2(\lambda+n+q)}
\end{aligned}
$$

for $j = 1, \ldots, 2n+2q$ and where β is used to incorporate knowledge of the distribution of $\boldsymbol{x}$. The authors of [97] note, for example, that a Gaussian distribution is best represented by $\beta = 2$. Compared to the EKF algorithm, the UKF algorithm requires the additional step

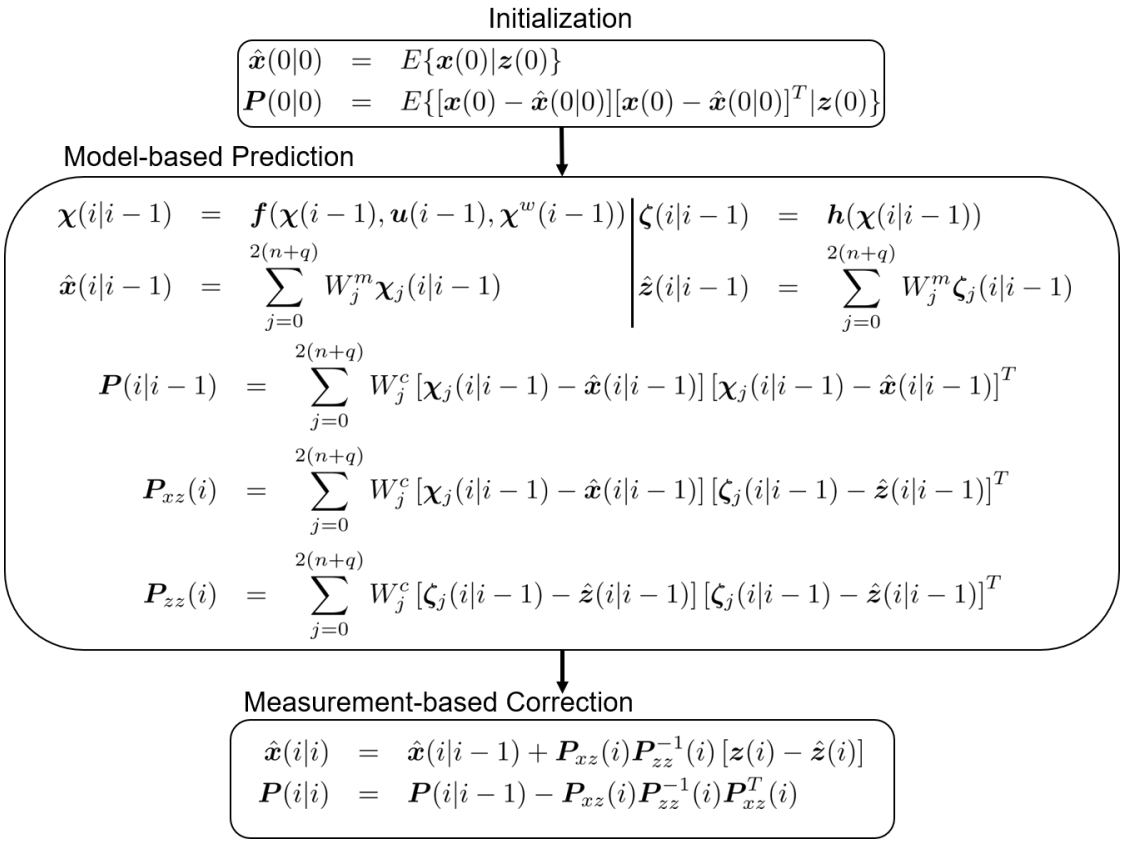

Figure 4.4: The UKF algorithm based on the nonlinear system (4.11) split into initialization, model-based prediction, and measurement-based correction steps using computed sigma points and weights. See [97], for example.

of computing sigma points and weights; the computational cost is about twice that of an EKF. As noted earlier, though, the approach does not require the computation of Jacobian matrices and the UKF exhibits other performance and accuracy advantages. Examples of wind estimation using a UKF can be found in [48, 50, 51, 52, 53, 54].

Chapter 5

An Invariant Extended Kalman Filter for Wind Estimation in Horizontal-Plane Flight

This chapter considers a 3DOF fixed-wing aircraft model where the UAV flies at constant altitude so that the motion occurs in a horizontal plane. We prove invariance of the planar dynamics and equivariance of the output with respect to the Lie group $SE(2)$ corresponding to planar rigid motions. The invariant EKF is designed to estimate position, orientation, velocity, and wind velocity using measurements from the onboard sensor suite of the UAV. The UAV is simulated in two different flow field scenarios – one-dimensional and two-dimensional von Kármán turbulence – and the wind estimation results using the invariant EKF are compared to estimates obtained using a conventional EKF. The rest of this chapter is organized as follows. In Section 5.1 the aircraft equations of motion and the measurement model are introduced. In Section 5.2, invariance of the UAV dynamics and equivariance of the measurement model are shown. The invariant EKF design is presented in Section 5.3. A simulation of the aircraft in different wind conditions and a comparison of wind estimation results using an invariant EKF and an EKF are described in Section 5.4.

5.1 Problem Description

We consider a fixed-wing UAV flying at a constant altitude under the influence of wind. We assume that the aircraft maintains wings level flight, even when turning. This assumption simplifies analysis, but it is not consistent with the normal operation of fixed-wing aircraft which bank to turn. Subsequent work involving a 6DOF flight dynamic model has relaxed this assumption, but we retain the simplifying assumption for the 3DOF model considered here for tutorial purposes. To describe the aircraft kinematics and dynamics, we first need to establish the relevant reference frames: the two-dimensional *inertial* and *body-fixed* reference frames.

- The *inertial* reference frame is given by the orthonormal pair $(\boldsymbol{i}_X, \boldsymbol{i}_Y)$. The origin of the inertial frame is fixed and its orientation has been chosen such that the positive $\boldsymbol{i}_X$ axis points towards geographic North and the positive $\boldsymbol{i}_Y$ axis points East. The location of the origin of the inertial reference frame is arbitrary (except at the poles, where North and East are ambiguous).

- The *body-fixed* reference frame is given by the orthonormal pair $(\boldsymbol{b}_x, \boldsymbol{b}_y)$. The origin of the body-fixed reference frame is the aircraft's center of gravity. The positive $\boldsymbol{b}_x$ axis coincides with the line defined by the intersection of the aircraft's longitudinal plane of symmetry and the horizontal plane in which the motion takes place. The positive $\boldsymbol{b}_y$ axis points to the right, as viewed from above.

The attitude kinematics and dynamics of the UAV flying in wind can be written as

$$\dot{\boldsymbol{X}} = \boldsymbol{R}_{\mathrm{IB}}\boldsymbol{v}_{\mathrm{r}} + \boldsymbol{V}_{\mathrm{w}} \tag{5.1a}$$

$$\dot{\psi} = r \tag{5.1b}$$

$$\dot{\boldsymbol{v}}_{\mathrm{r}} = \begin{bmatrix} v_y r \\ -v_x r \end{bmatrix} + \boldsymbol{f}_{\mathrm{A}} \tag{5.1c}$$

$$\dot{r} = m_{\mathrm{A}} \tag{5.1d}$$

$$\dot{\boldsymbol{V}}_{\mathrm{w}} = \boldsymbol{0} \tag{5.1e}$$

where $\boldsymbol{X}(t) = (X(t), Y(t))^T \in \mathbb{R}^2$ is the position of the UAV expressed in the inertial frame, $\psi(t) \in \mathbb{R}$ is the heading angle which relates the body-fixed frame to the inertial frame, $\boldsymbol{v}_{\mathrm{r}}(t) = (v_x(t), v_y(t))^T \in \mathbb{R}^2$ is the air-relative velocity of the UAV expressed in the body-fixed frame, $r(t) \in \mathbb{R}$ is the yaw rate of the UAV expressed in the body-fixed frame, $\boldsymbol{V}_{\mathrm{w}}(t) = (V_{wx}(t), V_{wy}(t))^T \in \mathbb{R}^2$ is the velocity of the wind expressed in the inertial frame, $\boldsymbol{f}_{\mathrm{A}} = (x_{\mathrm{A}}, y_{\mathrm{A}})^T$ is the *specific force* – force divided by mass – acting on the aircraft due to aerodynamic effects, and m_{A} is the *specific yaw moment* – moment premultiplied by inverse inertia – acting on the aircraft. The rotation matrix $\boldsymbol{R}_{\mathrm{IB}} \in SO(2)$ maps free vectors from the body-fixed frame to the inertial frame of reference and is given by

$$\boldsymbol{R}_{\mathrm{IB}} = \begin{pmatrix} \cos\psi & -\sin\psi \\ \sin\psi & \cos\psi \end{pmatrix}$$

The system (5.1) can be written in the vector form

$$\dot{\boldsymbol{x}} = \boldsymbol{f}(\boldsymbol{x}, \boldsymbol{u}) = \begin{pmatrix} \boldsymbol{R}_{\mathrm{IB}}\boldsymbol{v}_{\mathrm{r}} + \boldsymbol{V}_{\mathrm{w}} \\ r \\ \begin{bmatrix} v_y r \\ -v_x r \end{bmatrix} + \boldsymbol{f}_{\mathrm{A}} \\ m_{\mathrm{A}} \\ \boldsymbol{0} \end{pmatrix} \tag{5.2}$$

with state vector $\boldsymbol{x} = (\boldsymbol{X}^T, \psi, \boldsymbol{v}_{\mathrm{r}}^T, r, \boldsymbol{V}_{\mathrm{w}}^T)^T \in \mathbb{R}^{n=8}$ and input $\boldsymbol{u} = (\boldsymbol{f}_{\mathrm{A}}^T, m_{\mathrm{A}})^T \in \mathbb{R}^{p=3}$. We assume that the UAV is equipped with a GNSS receiver, IMU, magnetometer, angular accelerometer, and Pitot probe. The formulation of this problem assumes that $\boldsymbol{f}_{\mathrm{A}}$ and m_{A} are inputs thus aerodynamic force and moment models are not required. The output equation $\boldsymbol{y} \in \mathbb{R}^{q=6}$ is

$$\boldsymbol{y} = \boldsymbol{h}(\boldsymbol{x}, \boldsymbol{u}) = \begin{pmatrix} \boldsymbol{X} \\ \psi \\ \boldsymbol{v}_{\mathrm{i}} \\ r \end{pmatrix} \tag{5.3}$$

where $\boldsymbol{v}_{\mathrm{i}} = \boldsymbol{v}_r + \boldsymbol{R}_{\mathrm{IB}}^{\mathrm{T}}\boldsymbol{V}_{\mathrm{w}}$ is the aircraft's total velocity expressed in the body frame. Accordingly, we set up the problem for model-based wind estimation for the fixed-wing UAV assuming constant altitude flight with dynamics (5.1) and output (5.3).

5.2 Invariant Dynamics and Equivariant Output

In this section, we establish invariance of the dynamics (5.1) and equivariance of the output (5.3) with respect to the Lie group $G = SE(2)$, the space of planar translations and

rotations, which is the configuration manifold for the UAV under the assumption of planar motion. Let $g = (\boldsymbol{X}_g, \boldsymbol{R}_g) \in G = SE(2)$ where $\boldsymbol{X}_g \in \mathbb{R}^2$ denotes the position of the aircraft and where the planar rotation matrix $\boldsymbol{R}_g \in SO(2)$ is parameterized by the heading angle ψ_g:

$$\boldsymbol{R}_g = \begin{pmatrix} \cos\psi_g & \sin\psi_g \\ -\sin\psi_g & \cos\psi_g \end{pmatrix}$$

Definition 5.1. (Adapted from [26]). The system

$$\begin{aligned} \dot{\boldsymbol{x}} &= \boldsymbol{f}(\boldsymbol{x}, \boldsymbol{u}) \\ \boldsymbol{y} &= \boldsymbol{h}(\boldsymbol{x}, \boldsymbol{u}) \end{aligned}$$

has *G-invariant* dynamics and *G-equivariant* output if there exist transformations $\boldsymbol{\phi}_g(\boldsymbol{x}(t))$ and $\boldsymbol{\psi}_g(\boldsymbol{u}(t))$ on the state and input, respectively, such that

$$D\boldsymbol{\phi}_g(\boldsymbol{x}) \cdot \boldsymbol{f}(\boldsymbol{x}, \boldsymbol{u}) = \boldsymbol{f}(\boldsymbol{\phi}_g(\boldsymbol{x}), \boldsymbol{\psi}_g(\boldsymbol{u})) \tag{5.4}$$

$$\boldsymbol{\rho}_g(\boldsymbol{y}) = \boldsymbol{h}(\boldsymbol{\phi}_g(\boldsymbol{x}), \boldsymbol{\psi}_g(\boldsymbol{u})) \tag{5.5}$$

for all $g \in G, \boldsymbol{x}$, and $\boldsymbol{u}$. The invariance property also reads $\frac{d}{dt}\boldsymbol{\mathcal{X}} = \boldsymbol{f}(\boldsymbol{\mathcal{X}}, \boldsymbol{\psi}_g(\boldsymbol{u}))$ for $\boldsymbol{\mathcal{X}} = \boldsymbol{\phi}_g(\boldsymbol{x})$.

Proposition 5.2. *The dynamics (5.1) are left-invariant under the state and input transformations*

$$\boldsymbol{\phi_g} = \begin{pmatrix} \boldsymbol{X}_g + \boldsymbol{X} \\ \psi_g + \psi \\ \boldsymbol{R}_g \boldsymbol{v}_{\mathrm{r}} \\ r \\ \boldsymbol{V}_{\mathrm{w}} \end{pmatrix} \tag{5.6}$$

and

$$\boldsymbol{\psi}_g = \begin{pmatrix} \boldsymbol{R}_g \boldsymbol{f}_{\mathrm{A}} \\ m_{\mathrm{A}} \end{pmatrix} \tag{5.7}$$

Proof. According to the definition (5.4) with state and input transformations (5.6) and (5.7), respectively, the system is invariant if it satisfies the condition $\frac{d}{dt}\boldsymbol{\mathcal{X}} = \boldsymbol{f}(\boldsymbol{\phi}_g(\boldsymbol{x}), \boldsymbol{\psi}_g(\boldsymbol{u}))$, for all $g \in G, \boldsymbol{x}$, and $\boldsymbol{u}$. We write the dynamics of the transformed state as

$$\frac{d}{dt}\begin{pmatrix} \boldsymbol{X}_g + \boldsymbol{X} \\ \psi_g + \psi \\ \boldsymbol{R}_g \boldsymbol{v}_{\mathrm{r}} \\ r \\ \boldsymbol{V}_{\mathrm{w}} \end{pmatrix} = \begin{pmatrix} \boldsymbol{R}_{\mathrm{IB}} \boldsymbol{R}_g^T \boldsymbol{R}_g \boldsymbol{v}_{\mathrm{r}} + \boldsymbol{V}_{\mathrm{w}} \\ r \\ \boldsymbol{R}_g \begin{bmatrix} v_y r \\ -v_x r \end{bmatrix} + \boldsymbol{R}_g \boldsymbol{f}_{\mathrm{A}} \\ m_{\mathrm{A}} \\ \boldsymbol{0} \end{pmatrix}$$

We can rewrite the angular rate r and body velocity $\boldsymbol{v}_{\mathrm{r}}$ as vectors in three dimensions, given by $\boldsymbol{\omega} = (0, 0, r)^T$ and $\tilde{\boldsymbol{v}}_{\mathrm{r}} = (vx, vy, 0)^T$. The 2×2 rotation matrix $\boldsymbol{R}_g$ can be written in three dimensions as a rotation about the third body axis, which is an additional axis $\boldsymbol{b}_z$ that is mutually orthogonal to the body-fixed reference frame axes $(\boldsymbol{b}_x, \boldsymbol{b}_y)$ and points down from the center of gravity through the bottom of the aircraft. The rewritten rotation matrix is given by

$$\tilde{\boldsymbol{R}}_g = \begin{pmatrix} \cos\psi_g & \sin\psi_g & 0 \\ -\sin\psi_g & \cos\psi_g & 0 \\ 0 & 0 & 1 \end{pmatrix}$$

Any rotation $\tilde{\boldsymbol{R}}_g$ will be applied to the angular rate vector, and is given by $\tilde{\boldsymbol{R}}_g \boldsymbol{\omega} = (0, 0, r)^T$, which shows that $\boldsymbol{\omega}$ is invariant to rotations about the $\boldsymbol{b}_z$ axis. The third component of

dynamics of the transformed state is rewritten in terms of $\boldsymbol{\omega}, \tilde{\boldsymbol{v}}_{\mathrm{r}}$, and $\tilde{\boldsymbol{R}}_g$ as

$$\frac{d}{dt}\tilde{\boldsymbol{R}}_g\tilde{\boldsymbol{v}}_{\mathrm{r}} = \tilde{\boldsymbol{R}}_g\tilde{\boldsymbol{v}}_{\mathrm{r}} \times \tilde{\boldsymbol{R}}_g\boldsymbol{\omega} + \tilde{\boldsymbol{R}}_g\tilde{\boldsymbol{f}}_{\mathrm{A}}$$

where $\tilde{\boldsymbol{f}}_{\mathrm{A}} = (x_{\mathrm{A}}, y_{\mathrm{A}}, 0)^T$ is the augmented specific aerodynamic force $\boldsymbol{f}_{\mathrm{A}}$ that includes 0 as its third component. This equation then becomes

$$\tilde{\boldsymbol{R}}_g\dot{\tilde{\boldsymbol{v}}}_{\mathrm{r}} = \tilde{\boldsymbol{R}}_g\left(\tilde{\boldsymbol{v}}_{\mathrm{r}} \times \boldsymbol{\omega} + \tilde{\boldsymbol{f}}_{\mathrm{A}}\right)$$

This will result in

$$\begin{pmatrix} \boldsymbol{R}_g\dot{\boldsymbol{v}}_{\mathrm{r}} \\ 0 \end{pmatrix} = \begin{pmatrix} \boldsymbol{R}_g\left(\begin{bmatrix} v_y r \\ -v_x r \end{bmatrix} + \boldsymbol{f}_{\mathrm{A}}\right) \\ 0 \end{pmatrix}$$

Then, removing the row with the equation $0 = 0$, the dynamics of the transformed state are given by

$$\begin{pmatrix} \dot{\boldsymbol{X}} \\ \dot{\psi} \\ \boldsymbol{R}_g\dot{\boldsymbol{v}}_{\mathrm{r}} \\ \dot{r} \\ \dot{\boldsymbol{V}}_{\mathrm{w}} \end{pmatrix} = \begin{pmatrix} \boldsymbol{R}_{\mathrm{IB}}\boldsymbol{v}_{\mathrm{r}} + \boldsymbol{V}_{\mathrm{w}} \\ r \\ \boldsymbol{R}_g\left(\begin{bmatrix} v_y r \\ -v_x r \end{bmatrix} + \boldsymbol{f}_{\mathrm{A}}\right) \\ m_{\mathrm{A}} \\ \boldsymbol{0} \end{pmatrix}$$

The dynamics under the transformations $\boldsymbol{\phi}_g$ and $\boldsymbol{\psi}_g$ satisfy the condition (5.4), thus the system (5.1) is invariant under the transformations (5.6) and (5.7). □

Proposition 5.3. *The output equation (5.3) is G-equivariant given the output transforma-*

tion

$$\boldsymbol{\rho}_g(\boldsymbol{y}) = \begin{pmatrix} \boldsymbol{X}_g + \boldsymbol{X} \\ \psi_g + \psi \\ \boldsymbol{R}_g \boldsymbol{v}_{\mathrm{r}} + \boldsymbol{R}_g \boldsymbol{R}_{\mathrm{IB}}^{\mathrm{T}} \boldsymbol{V}_{\mathrm{w}} \\ r \end{pmatrix} \tag{5.8}$$

Proof. We can write the output (5.3) using the defined state and input transformations (5.6) and (5.7), respectively, as

$$\boldsymbol{h}(\boldsymbol{\phi}_g(\boldsymbol{x}), \boldsymbol{\psi}_g(\boldsymbol{u})) = \begin{pmatrix} \boldsymbol{X}_g + \boldsymbol{X} \\ \psi_g + \psi \\ \boldsymbol{R}_g \boldsymbol{v}_{\mathrm{r}} + \boldsymbol{R}_g \boldsymbol{R}_{\mathrm{IB}}^{\mathrm{T}} \boldsymbol{V}_{\mathrm{w}} \\ r \end{pmatrix} \tag{5.9}$$

The transformed output (5.9) is equivalent to (5.8), thus the output equation (5.3) is G-equivariant. □

We showed that a fixed-wing UAV in horizontal flight under a wind disturbance is invariant to left actions of $SE(2)$. In the following section, the G-invariant dynamics and G-equivariant output are used to design the invariant EKF, where we assume that the specific aerodynamic force and moment are directly measured.

5.3 The Invariant EKF for the 3DOF Fixed-Wing UAV

The invariant EKF for the fixed-wing UAV in horizontal flight is designed using the invariant dynamics and equivariant output from Section 5.2. The design of the invariant EKF can be summarized by the following steps [26] which are explained in detail in subsequent

paragraphs.

1. Solve the *normalization equations*.
2. Build an *invariant output error* and a set of *scalar invariants*.
3. Build the *invariant frame*.
4. Define an *invariant state estimate error* and then, using the *pre-observer* defined in [26], determine the *invariant state error dynamics*.
5. Design the invariant EKF by linearizing the invariant state error dynamics and invariant output error about zero state error.

Normalization Equations

For a Lie group of dimension m, the m normalization equations are obtained by taking the transformed state $\boldsymbol{\phi}_g(\boldsymbol{x})$ and separating it into two components – an m-dimensional component $\boldsymbol{\phi}_g^a(\boldsymbol{x})$ and an $(n-m)$-dimensional component $\boldsymbol{\phi}_g^b(\boldsymbol{x})$ – where $\boldsymbol{\phi}_g^a(\boldsymbol{x})$ is invertible with respect to the group action g. We then set $\boldsymbol{\phi}_g^a(\boldsymbol{x}) = \boldsymbol{c}$ where $\boldsymbol{c}$ is a constant in the range of $\boldsymbol{\phi}_g^a$.

For $G = SE(2)$, $m = 3$ and we get

$$\boldsymbol{\phi}_g^a(\boldsymbol{x}) = \begin{pmatrix} \boldsymbol{X} + \boldsymbol{X}_g \\ \psi + \psi_g \end{pmatrix} = \begin{pmatrix} \boldsymbol{0} \\ 0 \end{pmatrix} \tag{5.10}$$

Solving for $g = \boldsymbol{\gamma}(\boldsymbol{x})$ we obtain

$$\boldsymbol{\gamma}(\boldsymbol{x}) = \begin{pmatrix} -\boldsymbol{X} \\ -\psi \end{pmatrix} = \begin{pmatrix} \boldsymbol{X} \\ \psi \end{pmatrix}^{-1} \tag{5.11}$$

where $(\cdot)^{-1}$ indicates the inverse action.

Invariants and Invariant Output Error

The $n - m + p$ scalar invariants $\boldsymbol{I}(\hat{\boldsymbol{x}}, \boldsymbol{u}) := ((\boldsymbol{\phi}^b_{\boldsymbol{\gamma}(\hat{\boldsymbol{x}})}(\hat{\boldsymbol{x}}))^T, (\boldsymbol{\psi}_{\boldsymbol{\gamma}(\hat{\boldsymbol{x}})}(\boldsymbol{u}))^T)^T$ are

$$\boldsymbol{I}(\hat{\boldsymbol{x}}, \boldsymbol{u}) = \begin{pmatrix} \boldsymbol{R}_{\boldsymbol{\gamma}(\hat{\boldsymbol{x}})}\hat{\boldsymbol{v}}_{\mathrm{r}} \\ \hat{r} \\ \hat{\boldsymbol{V}}_{\mathrm{w}} \\ \boldsymbol{R}_{\boldsymbol{\gamma}(\hat{\boldsymbol{x}})}\boldsymbol{f}_{\mathrm{A}} \\ N \end{pmatrix} \tag{5.12}$$

The invariant output error is defined as $\boldsymbol{E} := \boldsymbol{\rho}_{\boldsymbol{\gamma}(\hat{\boldsymbol{x}})}(\hat{\boldsymbol{y}}) - \boldsymbol{\rho}_{\boldsymbol{\gamma}(\hat{\boldsymbol{x}})}(\boldsymbol{y})$. We determine that

$$\boldsymbol{E} = \begin{pmatrix} \hat{\boldsymbol{X}} - \boldsymbol{X} \\ \hat{\psi} - \psi \\ \boldsymbol{R}_{\boldsymbol{\gamma}(\hat{\boldsymbol{x}})}(\hat{\boldsymbol{v}}_{\mathrm{r}} - \boldsymbol{v}_{\mathrm{r}}) + \boldsymbol{R}_{\boldsymbol{\gamma}(\hat{\boldsymbol{x}})}\left(\hat{\boldsymbol{R}}^{\mathrm{T}}_{\mathrm{IB}}\hat{\boldsymbol{V}}_{\mathrm{w}} - \boldsymbol{R}^{\mathrm{T}}_{\mathrm{IB}}\boldsymbol{V}_{\mathrm{w}}\right) \\ \hat{r} - r \end{pmatrix} = \boldsymbol{T}\begin{pmatrix} \hat{\boldsymbol{X}} - \boldsymbol{X} \\ \hat{\psi} - \psi \\ \hat{\boldsymbol{v}}_{\mathrm{r}} - \boldsymbol{v}_{\mathrm{r}} + \hat{\boldsymbol{R}}^{\mathrm{T}}_{\mathrm{IB}}\hat{\boldsymbol{V}}_{\mathrm{w}} - \boldsymbol{R}^{\mathrm{T}}_{\mathrm{IB}}\boldsymbol{V}_{\mathrm{w}} \\ \hat{r} - r \end{pmatrix} \tag{5.13}$$

where $\boldsymbol{T} = \mathrm{diag}(\mathbb{I}_3, \hat{\boldsymbol{R}}_{\mathrm{IB}}, 1)$.

Invariant Frame

The invariant frame is given by

$$\boldsymbol{W} = (D\boldsymbol{\phi}_{\boldsymbol{\gamma}(\boldsymbol{x})}(\boldsymbol{x}))^{-1} \cdot \frac{\partial}{\partial \boldsymbol{x}} = \mathrm{diag}(\mathbb{I}_3, \boldsymbol{R}_g, \mathbb{I}_3) \tag{5.14}$$

where $\frac{\partial}{\partial \boldsymbol{x}}$ is the canonical frame of $\boldsymbol{x}$ and $\mathbb{I}_n$ denotes the $n \times n$ identity matrix.

Invariant State Estimate Error

The invariant state error is defined as $\boldsymbol{\eta} := \boldsymbol{\phi}_{\boldsymbol{\gamma}(\hat{\boldsymbol{x}})}(\hat{\boldsymbol{x}}) - \boldsymbol{\phi}_{\boldsymbol{\gamma}(\hat{\boldsymbol{x}})}(\boldsymbol{x})$ and is given by

$$\boldsymbol{\eta} = \begin{pmatrix} \hat{\boldsymbol{X}} - \boldsymbol{X} \\ \hat{\psi} - \psi \\ (\hat{v}_x - v_x)\cos\hat{\psi} - (\hat{v}_y - v_y)\sin\hat{\psi} \\ (\hat{v}_x - v_x)\sin\hat{\psi} - (\hat{v}_y - v_y)\sin\hat{\psi} \\ \hat{r} - r \\ \hat{\boldsymbol{V}}_{\mathrm{w}} - \boldsymbol{V}_{\mathrm{w}} \end{pmatrix} = \boldsymbol{W}^{\mathrm{T}} \begin{pmatrix} \boldsymbol{\eta}_X \\ \eta_\psi \\ \boldsymbol{\eta}_{v_{\mathrm{r}}} \\ \eta_r \\ \boldsymbol{\eta}_{V_{\mathrm{w}}} \end{pmatrix} \tag{5.15}$$

where $(\boldsymbol{\eta}_X^T, \eta_\psi, \boldsymbol{\eta}_{v_{\mathrm{r}}}^T, \eta_r, \boldsymbol{\eta}_{V_{\mathrm{w}}}^T) = ((\hat{\boldsymbol{X}} - \boldsymbol{X})^T, \hat{\psi} - \psi, (\hat{\boldsymbol{v}}_{\mathrm{r}} - \boldsymbol{v}_{\mathrm{r}})^T, \hat{r} - r, (\hat{\boldsymbol{V}}_{\mathrm{w}} - \boldsymbol{V}_{\mathrm{w}})^T)$. We now determine the dynamics of the invariant state error by taking the time derivative of (5.15) and introducing the symmetry-preserving pre-observer defined in [26]:

$$\frac{d}{dt}\hat{\boldsymbol{x}} = \boldsymbol{f}(\hat{\boldsymbol{x}}, \boldsymbol{u}) + \boldsymbol{W}\boldsymbol{K}\boldsymbol{E} \tag{5.16}$$

where $\boldsymbol{K}$ is the $n \times q$ observer gain matrix. Per Definition 6 in [26], the system (5.16) is a *pre-observer* for the given system and output if the error correction term $\boldsymbol{W}\boldsymbol{K}\boldsymbol{E}$ vanishes when $\hat{\boldsymbol{x}} = \boldsymbol{x}$. (A pre-observer is an *observer* if, furthermore, $\hat{\boldsymbol{x}}$ converges asymptotically to $\boldsymbol{x}$ when $\|\hat{\boldsymbol{x}} - \boldsymbol{x}\|$ is sufficiently small.) An *invariant* pre-observer is obtained by using the invariant frame $\boldsymbol{W}$ and the invariant output error $\boldsymbol{E}$ in the output injection term $\boldsymbol{W}\boldsymbol{K}\boldsymbol{E}$.

In the end, we obtain

$$\begin{aligned}\dot{\boldsymbol{\eta}} &= \boldsymbol{W}^T \begin{pmatrix} \hat{\boldsymbol{R}}_{\mathrm{IB}}\hat{\boldsymbol{v}}_{\mathrm{r}} - \boldsymbol{R}_{\mathrm{IB}}\boldsymbol{v}_{\mathrm{r}} + \boldsymbol{\eta}_{V_{\mathrm{w}}} \\ \eta_r \\ \begin{bmatrix} \hat{v}_y\hat{r} \\ -\hat{v}_x\hat{r} \end{bmatrix} - \begin{bmatrix} v_y r \\ -v_x r \end{bmatrix} \\ 0 \\ \mathbf{0} \end{pmatrix} + \boldsymbol{W}^T\boldsymbol{W}\boldsymbol{K} \begin{pmatrix} \boldsymbol{\eta}_X \\ \eta_\psi \\ \hat{\boldsymbol{R}}_{\mathrm{IB}}\boldsymbol{\eta}_{v_{\mathrm{r}}} + \boldsymbol{\eta}_{V_{\mathrm{w}}} + \boldsymbol{V}_{\mathrm{w}} - \hat{\boldsymbol{R}}_{\mathrm{IB}}\boldsymbol{R}_{\mathrm{IB}}^{\mathrm{T}}\boldsymbol{V}_{\mathrm{w}} \\ \eta_r \end{pmatrix} \\ &\quad + \dot{\boldsymbol{W}}^T \begin{pmatrix} \boldsymbol{\eta}_X \\ \eta_\psi \\ \hat{\boldsymbol{R}}_{\mathrm{IB}}^T\boldsymbol{\eta}_{v_{\mathrm{r}}} \\ \eta_r \\ \boldsymbol{\eta}_{V_{\mathrm{w}}} \end{pmatrix} \end{aligned} \tag{5.17}$$

Following [39] to design the invariant EKF, we linearize the invariant state error dynamics about $\boldsymbol{\eta} = \mathbf{0}$. Letting $\dot{\boldsymbol{\eta}}$ represent the vector field that defines the $\boldsymbol{\eta}$ dynamics, in a slight abuse of notation, we obtain the state matrix

$$\boldsymbol{A}_k = \left.\frac{\partial\dot{\boldsymbol{\eta}}}{\partial\boldsymbol{\eta}}\right|_{\boldsymbol{\eta}=\mathbf{0}} = \begin{pmatrix} 0 & 0 & 0 & 1 & 0 & 0 & 1 & 0 \\ 0 & 0 & 0 & 0 & 1 & 0 & 0 & 1 \\ 0 & 0 & 0 & 0 & 0 & 1 & 0 & 0 \\ 0 & 0 & 0 & 0 & 0 & \hat{v}_x\sin\hat{\psi} + \hat{v}_y\cos\hat{\psi} & 0 & 0 \\ 0 & 0 & 0 & 0 & 0 & -\hat{v}_x\cos\hat{\psi} + \hat{v}_y\sin\hat{\psi} & 0 & 0 \\ 0 & 0 & 0 & 0 & 0 & 0 & 0 & 0 \\ 0 & 0 & 0 & 0 & 0 & 0 & 0 & 0 \\ 0 & 0 & 0 & 0 & 0 & 0 & 0 & 0 \end{pmatrix} \tag{5.18}$$

We also obtain the output matrix

$$\boldsymbol{H}_k = \frac{\partial \boldsymbol{E}}{\partial \boldsymbol{\eta}}\bigg|_{\boldsymbol{\eta}=\mathbf{0}} = \begin{pmatrix} 1 & 0 & 0 & 0 & 0 & 0 & 0 & 0 \\ 0 & 1 & 0 & 0 & 0 & 0 & 0 & 0 \\ 0 & 0 & 1 & 0 & 0 & 0 & 0 & 0 \\ 0 & 0 & 0 & \cos\hat{\psi} & -\sin\hat{\psi} & 0 & 1 & 0 \\ 0 & 0 & 0 & \sin\hat{\psi} & \cos\hat{\psi} & 0 & 0 & 1 \\ 0 & 0 & 0 & 0 & 0 & 1 & 0 & 0 \end{pmatrix} \tag{5.19}$$

The invariant EKF algorithm

The invariant EKF is obtained by augmenting the symmetry-preserving pre-observer (5.16) with an $n \times 1$ vector of zero-mean, Gaussian, white process noise $\tilde{\boldsymbol{w}}$ with covariance matrix $\boldsymbol{Q}$. The output equation (5.3) is also augmented with a $q \times 1$ vector of zero-mean, Gaussian, white measurement noise $\tilde{\boldsymbol{v}}$ with covariance matrix $\boldsymbol{R}$. The invariant EKF algorithm is then defined by the following iterative sequence:

1. Initialize the filter with the initial state and error covariance $\hat{\boldsymbol{x}}(0)$ and $\boldsymbol{P}(0)$ using the original state variables $\boldsymbol{x}$.

2. Set $\hat{\boldsymbol{x}}^+(0) = \hat{\boldsymbol{x}}(0)$ and $\boldsymbol{P}^+(0) = \boldsymbol{W}(0)\boldsymbol{P}(0)\boldsymbol{W}(0)^T$.

3. Set $k = 0$.

4. Perform model-based prediction by propagating the state estimate and error covariance through the dynamic model:

$$\hat{\boldsymbol{x}}_{k+1}^- = \boldsymbol{f}(\hat{\boldsymbol{x}}_k^+, \boldsymbol{u}_k) \tag{5.20a}$$

$$\boldsymbol{P}_{k+1}^- = \boldsymbol{A}_k\boldsymbol{P}_k^+ + \boldsymbol{P}_k^+\boldsymbol{A}_k^T + \tilde{\boldsymbol{Q}} \tag{5.20b}$$

where $\tilde{\boldsymbol{Q}} = \frac{\partial \boldsymbol{\eta}}{\partial \tilde{\boldsymbol{w}}} \boldsymbol{Q} \frac{\partial \boldsymbol{\eta}}{\partial \tilde{\boldsymbol{w}}}^T$.

5. Perform the measurement-based correction by computing

$$\boldsymbol{K}_{k+1} = \boldsymbol{P}^-_{k+1} \boldsymbol{H}^T_{k+1} \left(\boldsymbol{H}_{k+1} \boldsymbol{P}^-_{k+1} \boldsymbol{H}^T_{k+1} + \tilde{\boldsymbol{R}}_{k+1} \right)^{-1} \tag{5.21a}$$

$$\hat{\boldsymbol{x}}^+_{k+1} = \hat{\boldsymbol{x}}^-_{k+1} + \boldsymbol{W}_{k+1} \boldsymbol{K}_{k+1} \boldsymbol{E}_{k+1} \tag{5.21b}$$

$$\boldsymbol{P}^+_{k+1} = \left(\mathbb{I} - \boldsymbol{K}_{k+1} \boldsymbol{H}_{k+1} \right) \boldsymbol{P}^-_{k+1} \tag{5.21c}$$

where $\tilde{\boldsymbol{R}}_{k+1} = \boldsymbol{T}_{k+1} \boldsymbol{R} \boldsymbol{T}^T_{k+1}$ and where $\boldsymbol{T}$ was defined following (5.13).

6. Set $k = k + 1$ and return to Step 4.

5.4 Simulation Results and Discussion

The fixed-wing UAV with parameters given in Table 5.1 was simulated in both 1D and 2D von Kármán turbulence so that the aircraft is continually perturbed from its nominal motion. The 1D von Kármán turbulence model is characterized by power spectral density functions of the spatial frequency Ω. Assuming that the nominal aircraft motion is due North, the gust spectrum components in the North and East directions are, respectively,

$$\Phi_{11}(\Omega) = \frac{L\sigma^2}{\pi} \frac{1}{(1 + (1.339 L \Omega)^2)^{5/6}} \tag{5.22a}$$

$$\Phi_{22}(\Omega) = \frac{L\sigma^2}{2\pi} \frac{1 + \frac{8}{3}(1.339 L \Omega)^2}{(1 + (1.339 L \Omega)^2)^{11/6}} \tag{5.22b}$$

where L is the turbulence length scale in feet, σ is the turbulence intensity in feet per second, and Ω has units of radians per foot. For the simulated wind conditions, the turbulence length scale was chosen to be $L = 20$ ft, the turbulence intensity was $\sigma = 10$ ft/s, and the spatial frequency Ω ranged from 10^{-4} to 10^{-1} rad/ft.

The 2D von Kármán turbulence model is characterized by power spectral density functions of two spatial frequencies Ω_1 and Ω_2.The gust spectrum components in the North and East directions are, respectively,

$$\Phi_{11}(\Omega) = \frac{(1.339L\sigma)^2}{6\pi}\frac{((1+(1.339L\Omega_1)^2+\frac{11}{3}(1.339L\Omega_2)^2)}{(1+(1.339L\Omega)^2(\Omega_1^2+\Omega_2^2))^{7/3}} \tag{5.23a}$$

$$\Phi_{22}(\Omega) = \frac{(1.339L\sigma)^2}{6\pi}\frac{((1+(1.339L\Omega_1)^2+\frac{11}{3}(1.339L\Omega_2)^2)}{(1+(1.339L\Omega)^2(\Omega_1^2+\Omega_2^2))^{7/3}} \tag{5.23b}$$

The same length scale, turbulence intensity, and spatial frequency range were chosen for the 2D von Kármán turbulence model as for the 1D model.

Table 5.1: Fixed-wing UAV parameters [98].

Parameter	Value
Mass, m	0.211 slugs
Moment of inertia, I_{zz}	0.3369 slug-ft^2
Wing span, b	5.91 ft
Wing surface area, S	4.92 ft^2
Mean aerodynamic chord, c	0.833 ft

The invariant EKF was used to estimate the inertial position, yaw angle, body velocity, and yaw rate of the aircraft as well as the velocity of the wind. The aircraft was simulated in an equilibrium flight condition with desired airspeed $V_t = ||\boldsymbol{v}_{\mathrm{r}}|| = 20$ ft/s and $\beta_* = \sin^{-1}\left(\frac{v_y}{V_t}\right) = 0$ using the aircraft dynamic equations presented in Section 5.1. Process noise was superposed on the dynamics with covariance matrix $\boldsymbol{Q} = \mathrm{diag}(0_{3\times3}, \sigma_{v_{\mathrm{r}}}^2\mathbb{I}_2, \sigma_r^2, \sigma_{V_{\mathrm{w}}}^2\mathbb{I}_2)$ where $\sigma_{v_{\mathrm{r}}} = 0.5$, $\sigma_r = 0.05$, and $\sigma_{V_{\mathrm{w}}} = 0.5$ (with commensurate units). Measurement noise was superposed on the output equation with covariance matrix $\boldsymbol{R} = \sigma_v^2\mathbb{I}_6$ where $\sigma_v = 0.01$ (with commensurate units). The aerodynamic force and moment coefficients from an identified flight dynamic model of a fixed-wing UAV from [98] were used to simulate the motion of the aircraft.

To initialize the filter, the initial state estimate was $\hat{\boldsymbol{x}}(0) = (0, 0, \pi/12, V_t \cos\beta_*, V_t \sin\beta_*, 0, 0, 0)^T$. The initial state error covariance matrix was $\boldsymbol{P}(0) = \text{diag}(1, 1, 1, 1, 1, 1, 10, 10)$. The invariant EKF estimates are compared to estimates using the conventional EKF. Figure 5.1 shows the aircraft trajectory and wind estimates using the invariant EKF and a conventional EKF for the aircraft in a constant altitude cruise subject to 1D von Kármán turbulence. Figure 5.2 shows the aircraft trajectory and wind estimates using the invariant EKF and a conventional EKF for the aircraft in a constant altitude cruise where a 40° yaw doublet is applied while in 1D von Kármán turbulence. Finally, Fig. 5.3 shows the aircraft trajectory and wind velocity estimates for the aircraft in a constant altitude cruise subject to 2D von Kármán turbulence. In all the simulated conditions, the invariant EKF outperforms the conventional EKF, providing more accurate wind velocity estimates.

To observe the effects of measurement noise on the invariant EKF wind estimates, the measurement noise covariance σ_v was varied from 0.01 to 0.2, thus changing the $\boldsymbol{R}$ matrix. The results of wind estimation with varying measurement noise covariance are presented in Fig. 5.4 where the aircraft is simulated in a constant altitude cruise in 1D von Kármán turbulence and subject to a 40° yaw doublet. It is shown that while the invariant EKF estimates degrade as measurement noise increases, they do not diverge whereas the estimates obtained using a conventional EKF do diverge. These results suggest that the invariant EKF provides more accurate wind velocity estimates than a conventional EKF for model-based wind estimation using a small fixed-wing UAV, where the specific aerodynamic force and moment are known inputs. Estimates of the position, attitude, yaw rate, and total velocity are provided in the appendix. While the EKF provides accurate estimates of $\boldsymbol{X}, \psi, r$ and $\boldsymbol{v}_{\text{i}}$, it does not accurately resolve $\boldsymbol{V}_w$ and $\boldsymbol{v}_r$, whereas the invariant EKF provides accurate estimates of all these quantities.

Figures 5.5, 5.6 and 5.7 show additional results including position, attitude, yaw rate, and

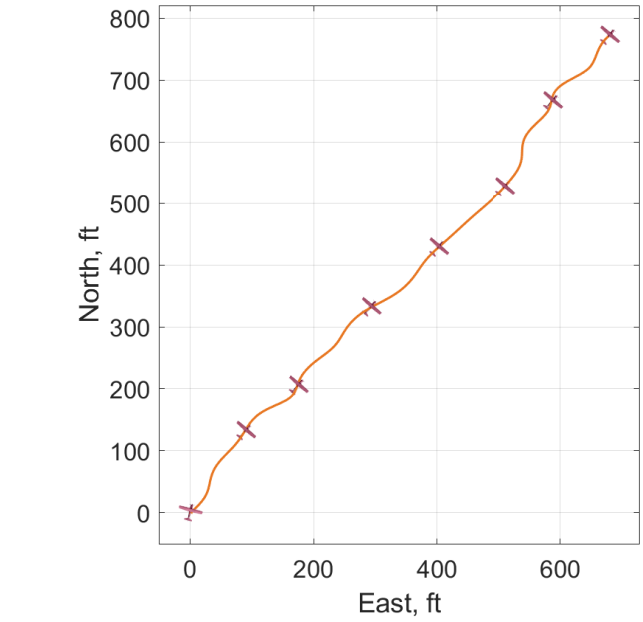

(a)

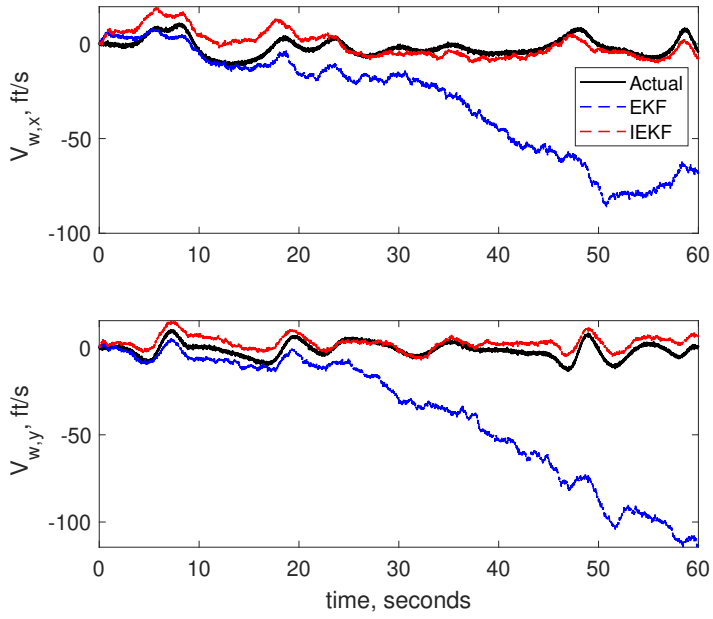

(b)

Figure 5.1: Simulation results for a fixed-wing UAV at constant altitude subject to 1D von Kármán turbulence: (a) the aircraft trajectory and (b) wind velocity estimates using the invariant EKF compared to a conventional EKF. The nominal condition is straight and level flight at constant speed.

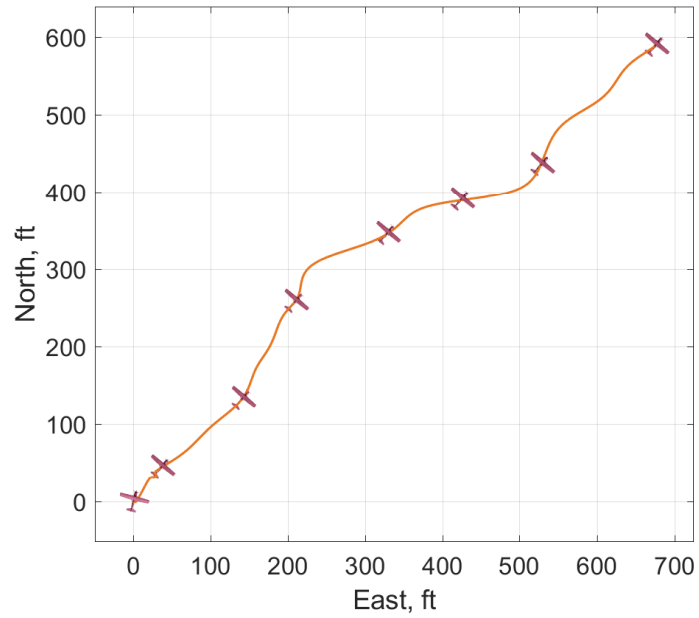

(a)

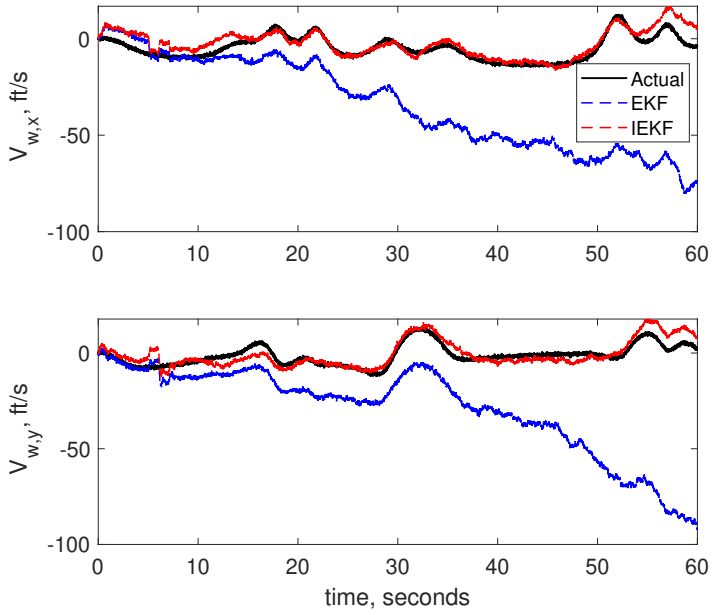

(b)

Figure 5.2: Simulation results for a fixed-wing UAV at constant altitude subject to 1D von Kármán turbulence: (a) the aircraft trajectory and (b) wind velocity estimates using the invariant EKF compared to a conventional EKF. The nominal condition is straight and level flight at constant speed, with a 40° yaw doublet applied at $t = 8$ seconds.

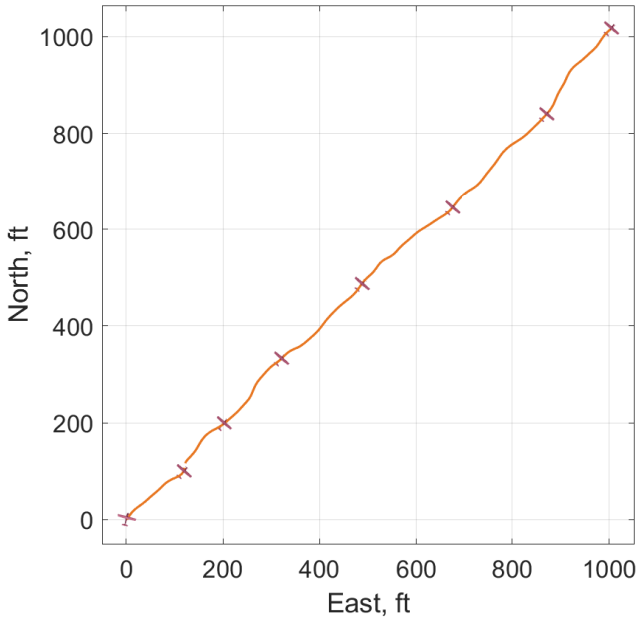

(a)

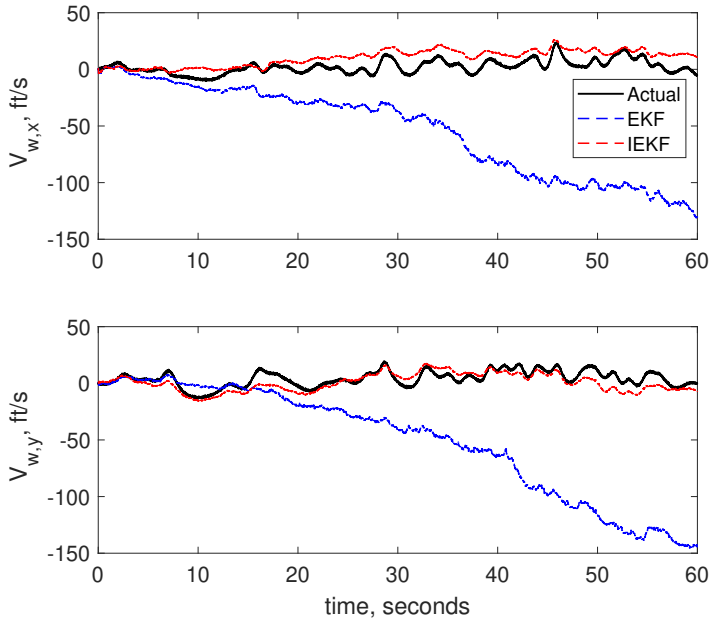

(b)

Figure 5.3: Simulation results for a fixed-wing UAV at constant altitude subject to 2D von Kármán turbulence: (a) the aircraft trajectory and (b) wind velocity estimates using the invariant EKF compared to a conventional EKF. The nominal condition is straight and level flight at constant speed.

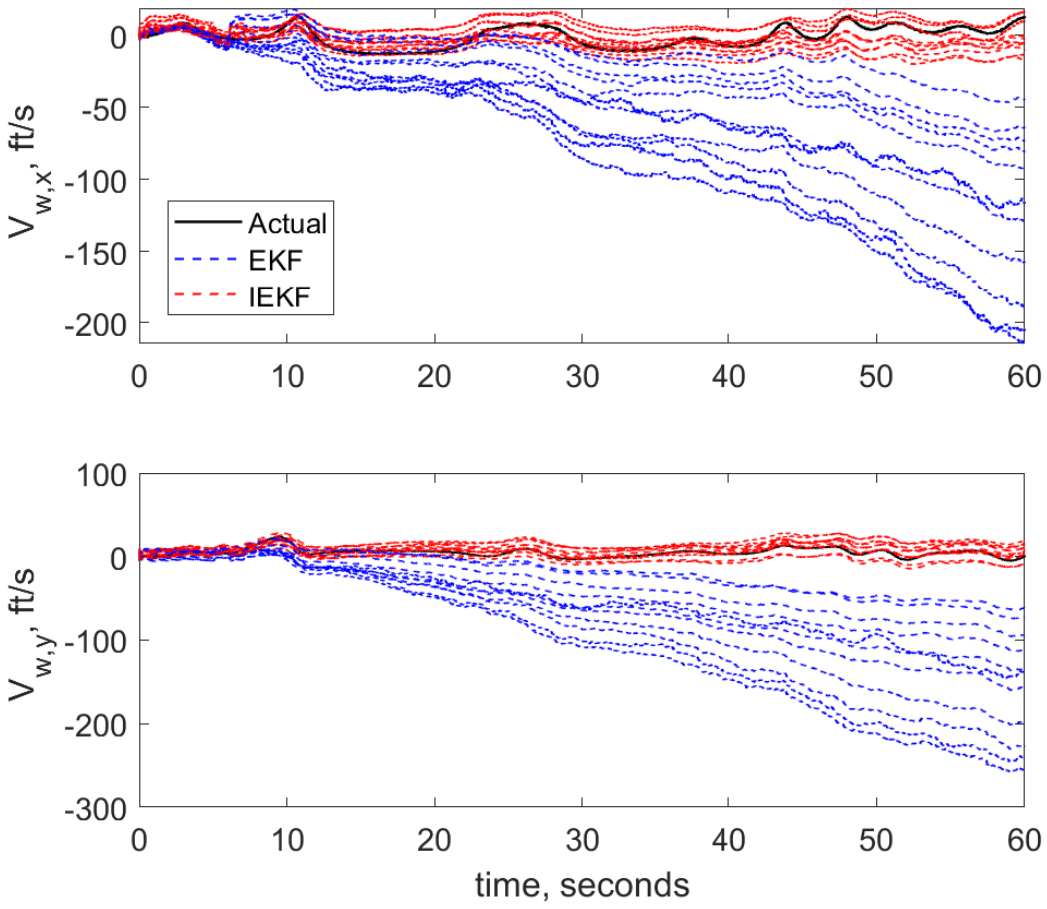

Figure 5.4: Wind estimates using the invariant EKF and a conventional EKF for the aircraft in a constant altitude cruise in 1D von Kármán turbulence subject to a 40° yaw doublet where measurement noise covariance σ_v is varied from 0.01 to 0.2 (with commensurate units).

total velocity estimates obtained using the invariant EKF and EKF in the different simulated flight conditions.

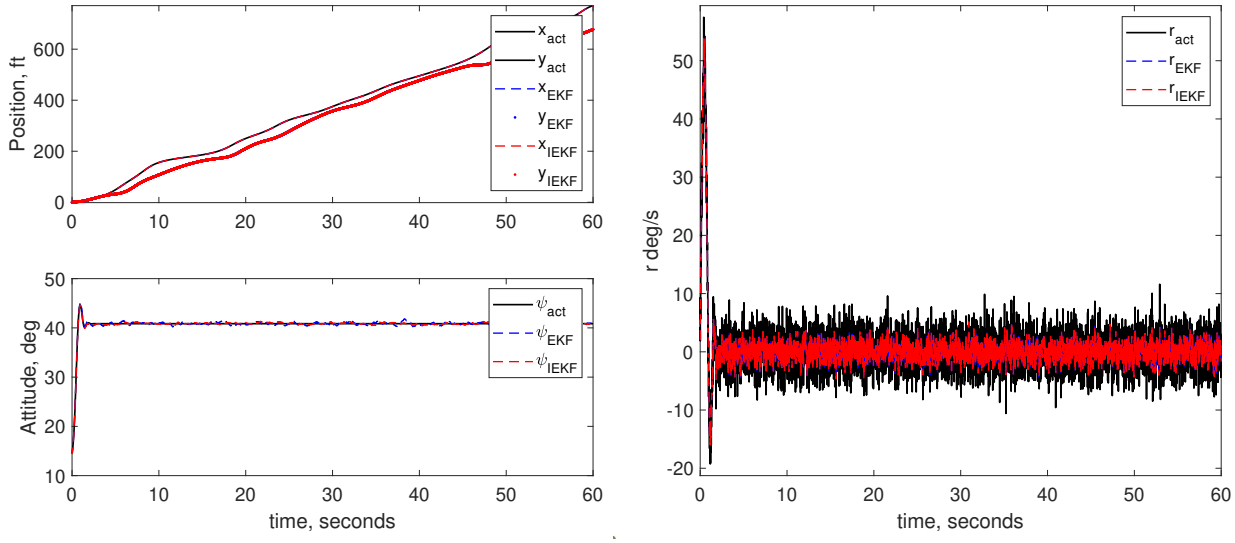

(a)

(b)

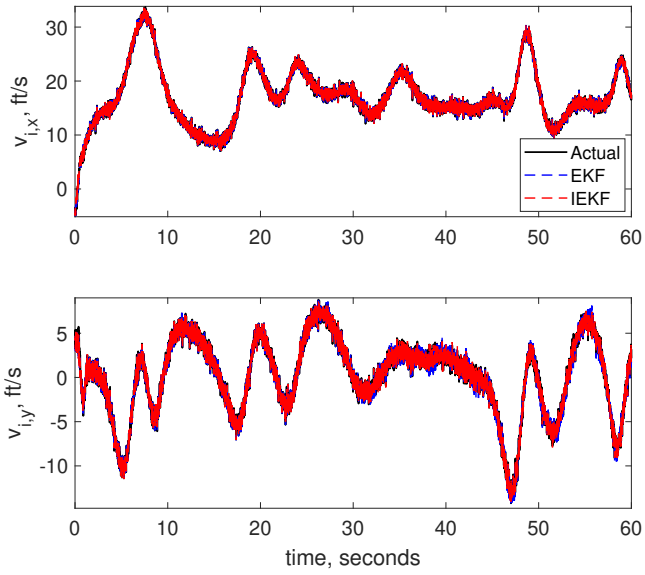

(c)

Figure 5.5: Estimates of (a) position (top) and attitude (bottom), (b) yaw rate, and (c) total velocity for the UAV simulated in 1D von Kármán turbulence along a constant altitude cruise.

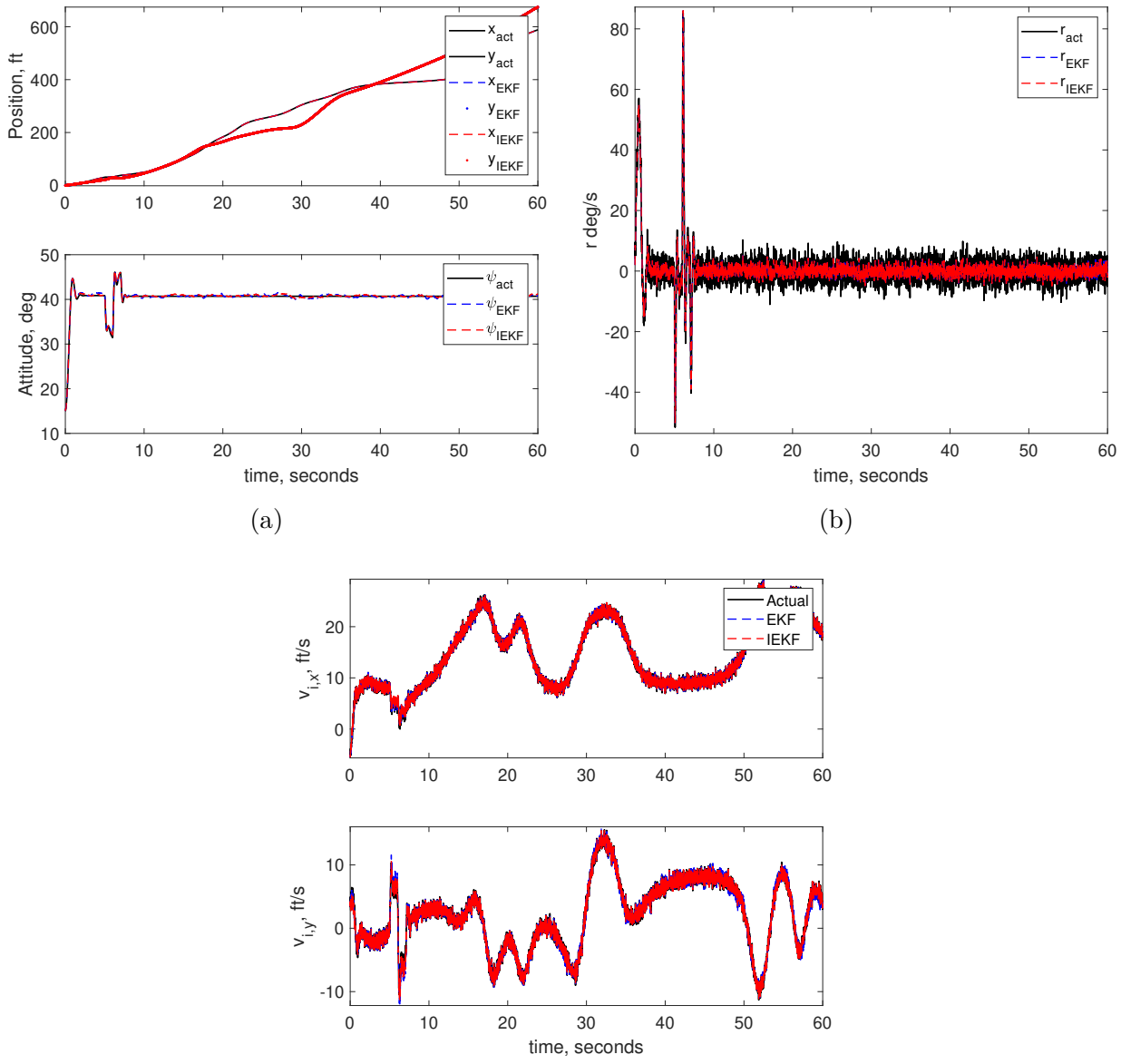

Figure 5.6: Estimates of (a) position (top) and attitude (bottom), (b) yaw rate, and (c) total velocity for the UAV simulated in 1D von Kármán turbulence along a constant altitude cruise subject to a 40° yaw doublet at $t = 8$ seconds.

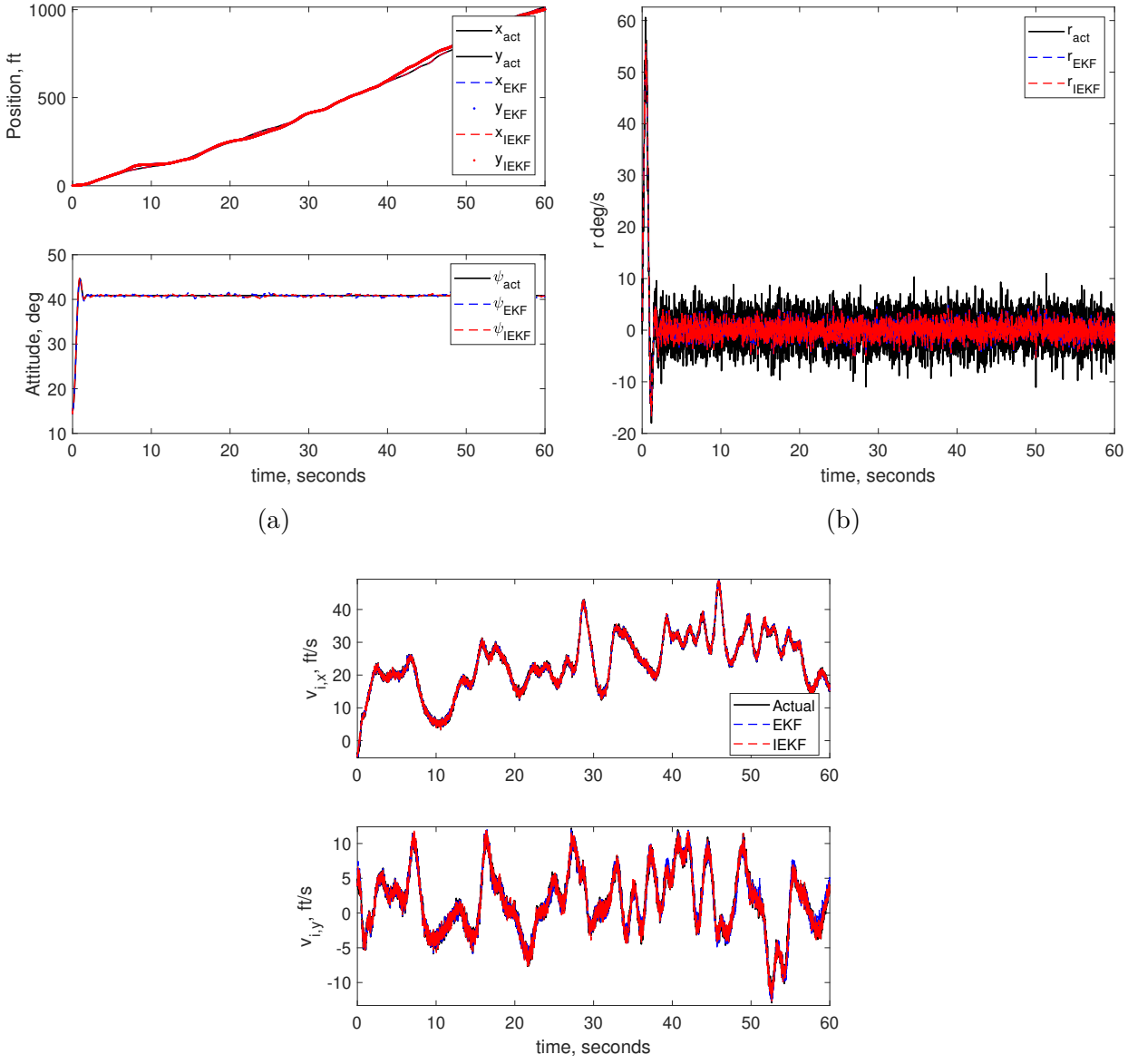

(a) (b)

(c)

Figure 5.7: Estimates of (a) position (top) and attitude (bottom), (b) yaw rate, and (c) total velocity for the UAV simulated in 2D von Kármán turbulence along a constant altitude cruise.

Chapter 6

A Left-Invariant Extended Kalman Filter for Indirect Wind Estimation

This chapter extends the results of Chapter 5 which concerned wind estimation using a small, fixed-wing UAV in constant altitude flight. Wind estimates were obtained using both the invariant EKF and a conventional EKF. For the 3DOF model of horizontal-plane motion used Chapter 5, a comparison of wind estimates obtained using the two filters showed that the invariant EKF outperformed the EKF. In this chapter, a simulation of a full 6DOF aircraft dynamic model is used for wind estimation in two nominal flight conditions: (i) steady, wings level flight at constant altitude and (ii) steady descending flight along a helical path of constant pitch and radius. In both cases, the nominal motion is disturbed by one-dimensional (1D) von Kármán turbulence and in case (i) the motion is also disturbed by a large pitch doublet. The nominal motion (i) is an example of a "permanent trajectory" [99] of the invariant rigid aircraft dynamics. (For case (i), the more general permanent trajectory allows for constant forward acceleration.) The invariant EKF is also applied to experimental flight data obtained using a small, fixed-wing UAV where some changes are made to the dynamic and measurement equations to make the wind estimation scheme more practical in regard to available measurements from the onboard sensor suite of the aircraft.

The rest of this chapter is organized as follows. Section 6.1 reviews the aircraft equations of motion and the measurement model that is used for filter design. In Section 6.2, it is

shown that the UAV dynamics are invariant under the left action of the Lie group $SE(3)$ of rigid body transformations and that the measurement model is equivariant under the left action of $SE(3)$. The invariant EKF design is presented in Section 6.3. Wind estimates obtained using the invariant EKF and a conventional EKF are presented in Section 6.4. The estimates are computed from simulations of aircraft motion for two nominal flight conditions, both subject to 1D von Kármán wind turbulence. The application of the invariant EKF to experimental flight data is given in Section 6.5 where local observability of the system is also discussed.

6.1 Problem Description

This chapter concerns estimating wind velocity using a 6DOF aircraft. The relevant reference frames for the 3DOF UAV in two-dimensional space in Chapter 5 are extended for the 6DOF UAV in three-dimensional space. The relevant reference frames required to discuss the aircraft's kinematics and dynamics are the *inertial* and *body-fixed* reference frames.

- The *inertial* reference frame is given by the orthonormal triad $(\boldsymbol{i}_X, \boldsymbol{i}_Y, \boldsymbol{i}_Z)$. The origin of the inertial frame is fixed and its orientation has been chosen such that the positive $\boldsymbol{i}_X$ axis points towards geographic North, the positive $\boldsymbol{i}_Y$ axis points East, and the positive $\boldsymbol{i}_Z$ axis points down completing the orthonormal frame. The location of the origin of the inertial reference frame is arbitrary.

- The *body-fixed* reference frame is given by the orthonormal triad $(\boldsymbol{b}_x, \boldsymbol{b}_y, \boldsymbol{b}_z)$. The origin of the body-fixed reference frame is the aircraft's center of gravity. The positive $\boldsymbol{b}_x$ axis points forward through the nose of the aircraft. The positive $\boldsymbol{b}_y$ axis points to the right, as viewed from above. The positive $\boldsymbol{b}_z$ axis points down through the underside

of the aircraft.

The attitude kinematics and dynamics of a UAV flying in wind are

$$\dot{\boldsymbol{X}} = \boldsymbol{R}_{\mathrm{IB}}\boldsymbol{v}_{\mathrm{r}} + \boldsymbol{V}_w \tag{6.1a}$$

$$\dot{\boldsymbol{R}}_{\mathrm{IB}} = \boldsymbol{R}_{\mathrm{IB}}\boldsymbol{\omega}^{\times} \tag{6.1b}$$

$$\dot{\boldsymbol{v}}_r = \boldsymbol{v}_{\mathrm{r}} \times \boldsymbol{\omega} + \boldsymbol{f}_{\mathrm{A}} + \boldsymbol{R}_{\mathrm{IB}}^{\mathrm{T}}\boldsymbol{g} \tag{6.1c}$$

$$\dot{\boldsymbol{\omega}} = \boldsymbol{I}^{-1}\left(\boldsymbol{I}\boldsymbol{\omega} \times \boldsymbol{\omega}\right) + \boldsymbol{m}_{\mathrm{A}} \tag{6.1d}$$

$$\dot{\boldsymbol{V}}_w = \boldsymbol{0} \tag{6.1e}$$

where $\boldsymbol{X} = (X, Y, Z)^{\mathrm{T}} \in \mathbb{R}^3$ denotes the inertial position of the UAV, $\boldsymbol{v}_{\mathrm{r}} = (v_{r,x}, v_{r,y}, v_{r,z})^{\mathrm{T}} \in \mathbb{R}^3$ is the air-relative velocity vector expressed in the body-fixed reference frame, $\boldsymbol{\omega} = (p, q, r)^{\mathrm{T}} \in \mathbb{R}^3$ is the angular velocity expressed in the body frame, and $\boldsymbol{V}_w = (V_{w,x}, V_{w,y}, V_{w,z})^{\mathrm{T}} \in \mathbb{R}^3$ is the wind velocity expressed in the inertial frame. The rotation matrix $\boldsymbol{R}_{\mathrm{IB}} \in SO(3)$ maps free vectors expressed in the body-fixed frame to the inertial frame. The matrix $\boldsymbol{R}_{BI}$ that maps vectors from the inertial frame to the body-fixed frame is $\boldsymbol{R}_{BI} = \boldsymbol{R}_{\mathrm{IB}}^{-1} = \boldsymbol{R}_{\mathrm{IB}}^{\mathrm{T}}$. The notation $(\cdot)^{\times}$ denotes the *cross-product equivalent matrix* satisfying $\boldsymbol{a}^{\times}\boldsymbol{b} = \boldsymbol{a} \times \boldsymbol{b}$ for 3×1 vectors $\boldsymbol{a}$ and $\boldsymbol{b}$. For the vector $\boldsymbol{\omega}$, for example, we have

$$\boldsymbol{\omega}^{\times} = \begin{pmatrix} 0 & -r & q \\ r & 0 & -p \\ -q & p & 0 \end{pmatrix}$$

The term $\boldsymbol{f}_{\mathrm{A}}$ in (6.1c) represents the *specific force* – force divided by mass – acting on the aircraft due to aerodynamic effects such as thrust, drag, side force, and lift. Similarly, $\boldsymbol{m}_{\mathrm{A}}$ in (6.1d) represents the *specific moment* – moment premultiplied by inverse inertia – due to aerodynamic effects such as pitch stiffness and yaw damping. The vector $\boldsymbol{g} = (0, 0, g)^{\mathrm{T}}$ is

the specific force due to gravity, where g is the magnitude of gravitational acceleration.

The system (6.1) can be written in terms of the state $\boldsymbol{x}(t)$ as

$$\dot{\boldsymbol{x}}(t) = \boldsymbol{f}(\boldsymbol{x}(t), \boldsymbol{u}(t)) = \begin{pmatrix} \boldsymbol{R}_{\mathrm{IB}}\boldsymbol{v}_{\mathrm{r}} + \boldsymbol{V}_w \\ \boldsymbol{R}_{\mathrm{IB}}\boldsymbol{\omega}^{\times} \\ \boldsymbol{v}_{\mathrm{r}} \times \boldsymbol{\omega} + \boldsymbol{f}_{\mathrm{A}} + \boldsymbol{R}_{\mathrm{IB}}^{\mathrm{T}}\boldsymbol{g} \\ \boldsymbol{I}^{-1}\left(\boldsymbol{I}\boldsymbol{\omega} \times \boldsymbol{\omega}\right) + \boldsymbol{m}_{\mathrm{A}} \\ \boldsymbol{0} \end{pmatrix} \tag{6.2}$$

where the state $\boldsymbol{x}(t)$ and input $\boldsymbol{u}(t)$ are

$$\boldsymbol{x}(t) = \begin{pmatrix} \boldsymbol{X} \\ \boldsymbol{R}_{\mathrm{IB}} \\ \boldsymbol{v}_{\mathrm{r}} \\ \boldsymbol{\omega} \\ \boldsymbol{V}_w \end{pmatrix} \qquad \text{and} \qquad \boldsymbol{u}(t) = \begin{pmatrix} \boldsymbol{f}_{\mathrm{A}} \\ \boldsymbol{m}_{\mathrm{A}} \end{pmatrix} \tag{6.3}$$

The reader is asked to forgive the abuse of notation in Eqs. (6.2), (6.3), and (6.4) where matrix differential equations and matrix state are concatenated with vector differential equations and vector state. This abuse of notation is used only to establish the invariance and equivariance of the dynamics and output, respectively. The invariant EKF formulation later uses a vector state in terms of Euler angles to parameterize the rotation matrix bmR_{IB}. We assume that the UAV is equipped with a GNSS receiver, IMU, magnetometer, and 5-hole

probe. The measurement equation $\boldsymbol{y}(t)$ is

$$\boldsymbol{y}(t) = \boldsymbol{h}(\boldsymbol{x}(t), \boldsymbol{u}(t)) = \begin{pmatrix} \boldsymbol{X} \\ \boldsymbol{R}_{\mathrm{IB}} \\ \boldsymbol{v}_{\mathrm{r}} \\ \boldsymbol{\omega} \\ \boldsymbol{f}_{\mathrm{A}} \\ \boldsymbol{m}_{\mathrm{A}} \end{pmatrix} \tag{6.4}$$

Note that the problem formulation assumes that $\boldsymbol{f}_{\mathrm{A}}$ and $\boldsymbol{m}_{\mathrm{A}}$ can be directly measured, e.g., using linear and angular accelerometers, so that aerodynamic force and moment models are not required. The time dependence of the state, input, and measurement are later dropped for simplicity.

6.2 Invariant Dynamics and Equivariant Output

In this section, the invariance of the dynamics (6.2) and the equivariance of the output (6.4) are established with respect to the Lie group $G = SE(3)$ of rigid body transformations (i.e., translations and rotations), which is the configuration manifold for a rigid UAV. Let $g = (\boldsymbol{X}_g, \boldsymbol{R}_g) \in G = SE(3)$ where $\boldsymbol{X}_g \in \mathbb{R}^3$ and $\boldsymbol{R}_g \in SO(3)$.

Definition 6.1. (Adapted from [26]). The system

$$\begin{aligned} \dot{\boldsymbol{x}} &= \boldsymbol{f}(\boldsymbol{x}, \boldsymbol{u}) \\ \boldsymbol{y} &= \boldsymbol{h}(\boldsymbol{x}, \boldsymbol{u}) \end{aligned}$$

has *G-invariant* dynamics and *G-equivariant* output if there exist transformations $\boldsymbol{\phi}_g(\boldsymbol{x}(t))$

and $\boldsymbol{\psi}_g(\boldsymbol{u}(t))$ on the state and input, respectively, such that

$$D\boldsymbol{\phi}_g(\boldsymbol{x}) \cdot \boldsymbol{f}(\boldsymbol{x}, \boldsymbol{u}) = \boldsymbol{f}(\boldsymbol{\phi}_g(\boldsymbol{x}), \boldsymbol{\psi}_g(\boldsymbol{u})) \tag{6.5a}$$

$$\boldsymbol{\rho}_g(\boldsymbol{y}) = \boldsymbol{h}(\boldsymbol{\phi}_g(\boldsymbol{x}), \boldsymbol{\psi}_g(\boldsymbol{u})) \tag{6.5b}$$

for all $g \in G, \boldsymbol{x}$, and $\boldsymbol{u}$. The invariance property also reads $\frac{d}{dt}\boldsymbol{\mathcal{X}} = \boldsymbol{f}(\boldsymbol{\phi}_g(\boldsymbol{x}), \boldsymbol{\psi}_g(\boldsymbol{u}))$ for $\boldsymbol{\mathcal{X}} = \boldsymbol{\phi}_g(\boldsymbol{x})$.

Definition 6.2. (Adapted from [20]). A smooth action of G on an element of a manifold M is a left (or right) action when an element $g \in G$ acts on some $\boldsymbol{z} \in M$ from the left (or right). Define a differentiable mapping $\phi_g : G \times M \to M$ such that the left and right actions are

$$\phi_g^l(\boldsymbol{z}) = g\boldsymbol{z}$$

$$\phi_g^r(\boldsymbol{z}) = \boldsymbol{z}g$$

Remark 6.3. (Adapted from [20]) Any left action $g\boldsymbol{z}$ gives rise to a right action $g^{-1}\boldsymbol{z}$, and vice versa, where any right action $\boldsymbol{z}g$ gives rise to a left action $\boldsymbol{z}g^{-1}$. The notation $(\cdot)^{-1}$ indicates the inverse action of G.

We consider only left actions of G on the state and input of the aircraft *i.e.*, the state and input transformations $\boldsymbol{\phi}_g$ and $\boldsymbol{\psi}_g$ represent transformations under the left action of $G = SE(3)$.

Proposition 6.4. *The dynamics (6.1) are invariant under the left action of* $SE(3)$ *on the*

state and input as given below:

$$\boldsymbol{\phi}_g(\boldsymbol{x}) = \begin{pmatrix} \boldsymbol{X} + \boldsymbol{X}_g \\ \boldsymbol{R}_{IB}\boldsymbol{R}_g^{\mathrm{T}} \\ \boldsymbol{R}_g\boldsymbol{v}_r \\ \boldsymbol{R}_g\boldsymbol{\omega} \\ \boldsymbol{V}_w \end{pmatrix} \tag{6.6}$$

and

$$\boldsymbol{\psi}_g(\boldsymbol{u}) = \begin{pmatrix} \boldsymbol{R}_g\boldsymbol{F}_A \\ \boldsymbol{R}_g\boldsymbol{M}_A \end{pmatrix} \tag{6.7}$$

Proof. According to the definition (6.5a) with state and input transformations (6.6) and (6.7), respectively, the system is invariant if it satisfies the condition $\frac{d}{dt}\boldsymbol{\mathcal{X}} = \boldsymbol{f}(\boldsymbol{\phi}_g(\boldsymbol{x}), \boldsymbol{\psi}_g(\boldsymbol{u}))$, for all $g \in G$ and for all $\boldsymbol{x}$ and $\boldsymbol{u}$. We write the dynamics of the transformed state as

$$\frac{d}{dt}\begin{pmatrix} \boldsymbol{X} + \boldsymbol{X}_g \\ \boldsymbol{R}_{\mathrm{IB}}\boldsymbol{R}_g^{\mathrm{T}} \\ \boldsymbol{R}_g\boldsymbol{v}_r \\ \boldsymbol{R}_g\boldsymbol{\omega} \\ \boldsymbol{V}_w \end{pmatrix} = \begin{pmatrix} \boldsymbol{R}_{\mathrm{IB}}\boldsymbol{R}_g^{\mathrm{T}}\boldsymbol{R}_g\boldsymbol{v}_r + \boldsymbol{V}_w \\ \boldsymbol{R}_{\mathrm{IB}}\boldsymbol{R}_g^{\mathrm{T}}\boldsymbol{R}_g\boldsymbol{\omega}^{\times}\boldsymbol{R}_g^{\mathrm{T}} \\ \boldsymbol{R}_g\boldsymbol{v}_r \times \boldsymbol{R}_g\boldsymbol{\omega} + \frac{1}{m}\boldsymbol{R}_g\boldsymbol{F}_A + \frac{1}{m}\boldsymbol{R}_g\boldsymbol{R}_{\mathrm{IB}}^{\mathrm{T}}\boldsymbol{F}_g \\ \boldsymbol{R}_g\boldsymbol{I}^{-1}\boldsymbol{R}_g^{\mathrm{T}}\left(\boldsymbol{R}_g\boldsymbol{\omega} \times \boldsymbol{R}_g\boldsymbol{\omega}\right) + \boldsymbol{R}_g\boldsymbol{I}^{-1}\boldsymbol{R}_g^{\mathrm{T}}\boldsymbol{R}_g\boldsymbol{M}_A \\ \boldsymbol{0} \end{pmatrix}$$

or

$$\begin{pmatrix} \dot{\boldsymbol{X}} \\ \dot{\boldsymbol{R}}_{\mathrm{IB}}\boldsymbol{R}_g^{\mathrm{T}} \\ \boldsymbol{R}_g\dot{\boldsymbol{v}}_r \\ \boldsymbol{R}_g\dot{\boldsymbol{\omega}} \\ \dot{\boldsymbol{V}}_w \end{pmatrix} = \begin{pmatrix} \boldsymbol{R}_{\mathrm{IB}}\boldsymbol{v}_r + \boldsymbol{V}_w \\ \boldsymbol{R}_{\mathrm{IB}}\boldsymbol{\omega}^{\times}\boldsymbol{R}_g^{\mathrm{T}} \\ \boldsymbol{R}_g(\boldsymbol{v}_r \times \boldsymbol{\omega} + \frac{1}{m}\boldsymbol{F}_A + \frac{1}{m}\boldsymbol{R}_{\mathrm{IB}}^{\mathrm{T}}\boldsymbol{F}_g) \\ \boldsymbol{R}_g(\boldsymbol{\omega} \times \boldsymbol{I}^{-1}\boldsymbol{\omega} + \boldsymbol{I}^{-1}\boldsymbol{M}_A) \\ \boldsymbol{0} \end{pmatrix}$$

The dynamics under the transformations $\boldsymbol{\phi}_g$ and $\boldsymbol{\psi}_g$ satisfy the condition (6.5a), thus the system described by Eqs. (6.1*a*)−(6.1*e*) is invariant under the transformations (6.6) and (6.7).

□

Proposition 6.5. *The output (6.4) is equivariant under the left action of* $SE(3)$ *with state and input transformations* $\boldsymbol{\phi}_g(\boldsymbol{x})$ *and* $\boldsymbol{\psi}_g(\boldsymbol{u})$*, respectively, with output transformation*

$$\boldsymbol{\rho}_g(\boldsymbol{y}) = \begin{pmatrix} \boldsymbol{X} + \boldsymbol{X}_g \\ \boldsymbol{R}_{\mathrm{IB}}\boldsymbol{R}_g^{\mathrm{T}} \\ \boldsymbol{R}_g\boldsymbol{v}_r \\ \boldsymbol{R}_g\boldsymbol{\omega} \\ \boldsymbol{R}_g\boldsymbol{a}_A \\ \boldsymbol{R}_g\boldsymbol{\alpha}_A \end{pmatrix} \tag{6.8}$$

Proof. Using the defined output transformation (6.8) it can be shown that condition (6.5b)

is satisfied.

$$\begin{aligned} \boldsymbol{\rho}_g(\boldsymbol{y}) &= \boldsymbol{y}(\boldsymbol{\phi}_g(\boldsymbol{x}), \boldsymbol{\psi}_g(\boldsymbol{u})) \\ \begin{pmatrix} \boldsymbol{X} + \boldsymbol{X}_g \\ \boldsymbol{R}_{\mathrm{IB}} \boldsymbol{R}_g^{\mathrm{T}} \\ \boldsymbol{R}_g \boldsymbol{v}_r \\ \boldsymbol{R}_g \boldsymbol{\omega} \\ \boldsymbol{R}_g \boldsymbol{a}_A \\ \boldsymbol{R}_g \boldsymbol{\alpha}_A \end{pmatrix} &= \begin{pmatrix} \boldsymbol{X} + \boldsymbol{X}_g \\ \boldsymbol{R}_{\mathrm{IB}} \boldsymbol{R}_g^{\mathrm{T}} \\ \boldsymbol{R}_g \boldsymbol{v}_r \\ \boldsymbol{R}_g \boldsymbol{\omega} \\ \boldsymbol{R}_g \boldsymbol{a}_A \\ \boldsymbol{R}_g \boldsymbol{\alpha}_A \end{pmatrix} \end{aligned}$$

The transformed output satisfies the condition (6.5b), thus the output equation (6.4) is $SE(3)$-equivariant. □

It has been shown that a fixed-wing UAV flying under a wind disturbance is invariant under the left action of $SE(3)$ and the given measurements are $SE(3)$-equivariant. In the following section, the $SE(3)$-invariant dynamics and $SE(3)$-equivariant output are used to design the invariant EKF.

6.3 The Invariant Extended Kalman Filter for the 6DOF Fixed-Wing UAV

The invariant EKF for the fixed-wing UAV is designed using the invariant dynamics and equivariant output from Section 6.2. This follows from Section 5.3 where the invariant EKF is developed for the 3DOF UAV. In developing the invariant EKF for a 6DOF fixed-wing aircraft, we first rewrite the attitude kinematics in the matrix differential equation (6.1b) in

the vector form:

$$\dot{\boldsymbol{\Theta}} = \underbrace{\begin{pmatrix} 1 & \sin\phi\tan\theta & \cos\phi\tan\theta \\ 0 & \cos\phi & -\sin\phi \\ 0 & \sin\phi\sec\theta & \cos\phi\sec\theta \end{pmatrix}}_{\boldsymbol{L}_{\mathrm{IB}}(\boldsymbol{\Theta})} \boldsymbol{\omega} \tag{6.9}$$

where $\boldsymbol{\Theta} = (\phi, \theta, \psi)^{\mathrm{T}} \in \mathbb{R}^3$ contains the roll, pitch, and yaw angles that parameterize the rotation matrix $\boldsymbol{R}_{\mathrm{IB}}$ as follows:

$$\boldsymbol{R}_{\mathrm{IB}}(\boldsymbol{\Theta}) = \begin{pmatrix} \cos\theta\cos\psi & \cos\psi\sin\theta\sin\phi - \cos\phi\sin\psi & \cos\psi\sin\theta\cos\phi + \sin\phi\sin\psi \\ \cos\theta\sin\psi & \sin\phi\sin\theta\sin\psi + \cos\phi\cos\psi & \sin\theta\cos\phi\sin\psi - \sin\phi\cos\psi \\ -\sin\theta & \cos\theta\sin\phi & \cos\theta\cos\phi \end{pmatrix} \tag{6.10}$$

We note that there is no global three-parameter representation for $SO(3)$. The Euler angle parameterization, for example, is singular at pitch angles $\theta = \pm\frac{\pi}{2}$. (The matrix $\boldsymbol{L}_{\mathrm{IB}}(\boldsymbol{\Theta})$ defined in (6.9) is not invertible for these values of θ.) We adopt these local coordinates for calculations, in any case, and with the expectation that the aircraft will not pass through this singular attitude in wind estimation applications.

6.3.1 Invariant EKF design steps

We consider the (extended) state and output vectors

$$\boldsymbol{x} = \begin{pmatrix} \boldsymbol{X} \\ \boldsymbol{\Theta} \\ \boldsymbol{v}_r \\ \boldsymbol{\omega} \\ \boldsymbol{V}_w \end{pmatrix} \quad \text{and} \quad \boldsymbol{y} = \boldsymbol{h}(\boldsymbol{x}, \boldsymbol{u}) = \begin{pmatrix} \boldsymbol{X} \\ \boldsymbol{\Theta} \\ \boldsymbol{v}_r \\ \boldsymbol{\omega} \\ \boldsymbol{a}_A \\ \boldsymbol{\alpha}_A \end{pmatrix} \tag{6.11}$$

As described in Section 5.3, the design of the invariant EKF can be summarized by the following steps [26]:

1. Solve the normalization equations.
2. Build an invariant output error and a set of scalar invariants.
3. Build the invariant frame.
4. Define an invariant state estimate error and then, using the pre-observer defined in [26], determine the invariant state error dynamics.
5. Design the invariant EKF by linearizing the invariant state error dynamics and invariant output error about zero state error.

Normalization Equations

A brief description of how the normalization equations are obtained is given adapting definitions and Theorem 8.25 from [23]. A Lie group H with elements $\boldsymbol{h}$ can act on a manifold

Q with elements $\boldsymbol{q}$. The action of $\boldsymbol{h}$ on $\boldsymbol{q}$ defines a transformation of the element $\boldsymbol{q} \in Q$. The group H is then referred to as the transformation group acting on the manifold Q. The transformation group has associated orbits and local cross-sections of those orbits, where the cross-sections form a submanifold that intersects each orbit at most once and transversally, that is the submanifold does not share any common tangent directions with the orbit. For example, consider a transformation by the action of the Lie group $SO(2)$, the space of planar rotations, on elements of a manifold $\boldsymbol{q} \in Q = \mathbb{R}^2 \setminus \{0\}$. The orbits of the transformation acting on points in $\mathbb{R}^2$ are circles centered at the origin with radius $r = \sqrt{q_1^2 + q_2^2}$ where $\boldsymbol{q} = (q_1, q_2)^{\mathrm{T}} \in Q$. A cross-section of the orbits can be given by a ray that intersects each orbit transversally and at most once. The normalization equations then arise from the process of defining a *moving frame* associated with the given cross-sections of the orbits of the transformation group. Define the group transformation $\bar{\boldsymbol{q}} = \boldsymbol{h} \cdot \boldsymbol{q} = \boldsymbol{w}(\boldsymbol{h}, \boldsymbol{q})$. The functions $\boldsymbol{w}$ are equated to some constants $\boldsymbol{c} = (c_1, \ldots, c_s)^{\mathrm{T}}$ where $s = \dim(H)$ and the constants $\boldsymbol{c}$ are in the range of the functions $\boldsymbol{w}$. The Implicit Function Theorem implies that the equations $\boldsymbol{w}(\boldsymbol{h}, \boldsymbol{q}) = \boldsymbol{h} \cdot \boldsymbol{q}$ can be locally solved for the group parameters in terms of the coordinates $\boldsymbol{q}$. The solution is written as $\boldsymbol{h} = \boldsymbol{\gamma}(\boldsymbol{q})$ where the map $\boldsymbol{\gamma} : Q \to H$ is the moving frame associated with the given cross-section. The equations $\boldsymbol{h} \cdot \boldsymbol{q} = \boldsymbol{c}$ are called the *normalization equations.*

The normalization equations associated with the aircraft system considered in this work are obtained by first separating the state transformation $\boldsymbol{\phi}_g(\boldsymbol{x})$ can be separated into two parts: $\boldsymbol{\phi}_g^a$ and $\boldsymbol{\phi}_g^b$. The first part $\boldsymbol{\phi}_g^a$ has dimension m where $m = dim(G)$ and is invertible with respect to the group action of G. The second portion of the state transformation $\boldsymbol{\phi}_g^b$ will be used in the following step to solve for the functionally independent invariants. We set $\boldsymbol{\phi}_g^a = \boldsymbol{c}$ where $\boldsymbol{c}$ is a constant in the range of $\boldsymbol{\phi}_g^a$. In this case, the constants c were chosen to be $\boldsymbol{c} = (\boldsymbol{0}_{1\times 3}, \boldsymbol{0}_{1\times 3})^{\mathrm{T}}$.

For $G = SE(3)$, and working in coordinates, we have

$$\boldsymbol{\phi}_g^a(\boldsymbol{x}) = \begin{pmatrix} \boldsymbol{X} + \boldsymbol{X}_g \\ \boldsymbol{\Theta} + \boldsymbol{\Theta}_g \end{pmatrix} = \begin{pmatrix} \mathbf{0} \\ \mathbf{0} \end{pmatrix} \tag{6.12}$$

An alternative representation of the last 3 equations of (6.12) could be to continue working in terms of rotation matrices where the left-hand side of the equations would be $\boldsymbol{R}_g \boldsymbol{R}_{\mathrm{IB}}$ which one could equate to the 3×3 identity matrix $\mathbb{I}_3$, which is a constant in the range of the transformation $\boldsymbol{R}_g \boldsymbol{R}_{\mathrm{IB}}$. Solving Eq. (6.12) for $g = \boldsymbol{\gamma}(\boldsymbol{x})$ we obtain

$$\boldsymbol{\gamma}(\boldsymbol{x}) = \begin{pmatrix} -\boldsymbol{X} \\ -\boldsymbol{\Theta} \end{pmatrix} = \begin{pmatrix} \boldsymbol{X} \\ \boldsymbol{\Theta} \end{pmatrix}^{-1} \tag{6.13}$$

where $(\cdot)^{-1}$ indicates the inverse action.

Invariants and Invariant Output Error

The $n - m + p$ scalar invariants $\boldsymbol{I}$, where $n = \dim(\boldsymbol{x})$ and $p = \dim(\boldsymbol{u})$, are the functions $\boldsymbol{I}(\hat{\boldsymbol{x}}, \boldsymbol{u}) := ((\boldsymbol{\phi}^b_{\boldsymbol{\gamma}(\hat{\boldsymbol{x}})}(\hat{\boldsymbol{x}}))^{\mathrm{T}}, (\boldsymbol{\psi}_{\boldsymbol{\gamma}(\hat{\boldsymbol{x}})}(\boldsymbol{u}))^{\mathrm{T}})^{\mathrm{T}}$ where $\hat{\boldsymbol{x}}$ will later denote an estimate of the system state $\boldsymbol{x}$. The invariants $\boldsymbol{I}$ are functions that are constant on orbits of the transformation group G. For the given problem, we have

$$\boldsymbol{I}(\hat{\boldsymbol{x}}, \boldsymbol{u}) = \begin{pmatrix} \boldsymbol{R}_{\boldsymbol{\gamma}(\hat{\boldsymbol{x}})} \hat{\boldsymbol{v}}_r \\ \boldsymbol{R}_{\boldsymbol{\gamma}(\hat{\boldsymbol{x}})} \hat{\boldsymbol{\omega}} \\ \hat{\boldsymbol{V}}_w \\ \boldsymbol{R}_{\boldsymbol{\gamma}(\hat{\boldsymbol{x}})} \boldsymbol{a}_A \\ \boldsymbol{R}_{\boldsymbol{\gamma}(\hat{\boldsymbol{x}})} \boldsymbol{\alpha}_A \end{pmatrix} \tag{6.14}$$

The invariant output error is defined as $\boldsymbol{E} := \boldsymbol{\rho}_{\boldsymbol{\gamma}(\hat{\boldsymbol{x}})}(\hat{\boldsymbol{y}}) - \boldsymbol{\rho}_{\boldsymbol{\gamma}(\hat{\boldsymbol{x}})}(\boldsymbol{y})$ where $\hat{\boldsymbol{y}}$ will later denote the output corresponding to the state estimate $\hat{\boldsymbol{x}}$. For the given system, we find

$$\begin{aligned}
\boldsymbol{E}: &= \boldsymbol{\rho}_{\boldsymbol{\gamma}(\hat{\boldsymbol{x}})}(\hat{\boldsymbol{y}}) - \boldsymbol{\rho}_{\boldsymbol{\gamma}(\hat{\boldsymbol{x}})}(\boldsymbol{y}) \\
&= \begin{pmatrix} \hat{\boldsymbol{X}} - \boldsymbol{X} \\ \hat{\boldsymbol{\Theta}} - \boldsymbol{\Theta} \\ \tilde{\boldsymbol{R}}_{\mathrm{IB}}^{\mathrm{T}}(\hat{\boldsymbol{v}}_r - \boldsymbol{v}_r) \\ \tilde{\boldsymbol{R}}_{\mathrm{IB}}^{\mathrm{T}}(\hat{\boldsymbol{\omega}} - \boldsymbol{\omega}) \\ \tilde{\boldsymbol{R}}_{\mathrm{IB}}^{\mathrm{T}}(\hat{\boldsymbol{a}}_A - \boldsymbol{a}_A) \\ \tilde{\boldsymbol{R}}_{\mathrm{IB}}^{\mathrm{T}}(\hat{\boldsymbol{\alpha}}_A - \boldsymbol{\alpha}_A) \end{pmatrix} = \boldsymbol{T} \begin{pmatrix} \hat{\boldsymbol{X}} - \boldsymbol{X} \\ \hat{\boldsymbol{\Theta}} - \boldsymbol{\Theta} \\ \hat{\boldsymbol{v}}_r - \boldsymbol{v}_r \\ \hat{\boldsymbol{\omega}} - \boldsymbol{\omega} \\ \hat{\boldsymbol{a}}_A - \boldsymbol{a}_A \\ \hat{\boldsymbol{\alpha}}_A - \boldsymbol{\alpha}_A \end{pmatrix}
\end{aligned} \tag{6.15}$$

where $\tilde{\boldsymbol{R}}_{\mathrm{IB}} = \boldsymbol{R}_{\mathrm{IB}}(-\boldsymbol{\Theta})$ and $\boldsymbol{T} = \mathrm{diag}(\mathbb{I}_6, \tilde{\boldsymbol{R}}_{\mathrm{IB}}^{\mathrm{T}}, \tilde{\boldsymbol{R}}_{\mathrm{IB}}^{\mathrm{T}}, \tilde{\boldsymbol{R}}_{\mathrm{IB}}^{\mathrm{T}}, \tilde{\boldsymbol{R}}_{\mathrm{IB}}^{\mathrm{T}})$.

Invariant Frame

The method of moving frames from step 1 allows for the construction of an invariant frame which forms a basis of the tangent space at $\boldsymbol{x}$ to the configuration manifold M. The invariant frame is given by

$$\begin{aligned}
\boldsymbol{W} &:= \left(D\boldsymbol{\phi}_{\boldsymbol{\gamma}(\boldsymbol{x})}(\boldsymbol{x})\right)^{-1} \cdot \frac{\partial}{\partial \boldsymbol{x}} \\
&= D\boldsymbol{\phi}_{\boldsymbol{\gamma}^{-1}(\boldsymbol{x})}(\boldsymbol{x}) \cdot \frac{\partial}{\partial \boldsymbol{x}} \\
&= \mathrm{diag}(\mathbb{I}_6, \boldsymbol{R}_{\boldsymbol{\gamma}(\boldsymbol{x})}, \boldsymbol{R}_{\boldsymbol{\gamma}(\boldsymbol{x})}, \mathbb{I}_3)
\end{aligned} \tag{6.16}$$

where $\frac{\partial}{\partial \boldsymbol{x}}$ is the canonical frame of $\boldsymbol{x}$ and $\mathbb{I}_n$ denotes the $n \times n$ identity matrix.

Invariant State Estimate Error

The invariant state estimate error is defined as $\boldsymbol{\eta} := \boldsymbol{\phi}_{\boldsymbol{\gamma}(\hat{\boldsymbol{x}})}(\hat{\boldsymbol{x}}) - \boldsymbol{\phi}_{\boldsymbol{\gamma}(\hat{\boldsymbol{x}})}(\boldsymbol{x})$. For the given problem,

$$\boldsymbol{\eta} = \begin{pmatrix} \boldsymbol{\eta}_X \\ \boldsymbol{\eta}_\Theta \\ \boldsymbol{\eta}_{v_r} \\ \boldsymbol{\eta}_\omega \\ \boldsymbol{\eta}_{V_w} \end{pmatrix} = \begin{pmatrix} \hat{\boldsymbol{X}} - \boldsymbol{X} \\ \hat{\boldsymbol{\Theta}} - \boldsymbol{\Theta} \\ \tilde{\boldsymbol{R}}_{\mathrm{IB}}^{\mathrm{T}}(\hat{\boldsymbol{v}}_r - \boldsymbol{v}_r) \\ \tilde{\boldsymbol{R}}_{\mathrm{IB}}^{\mathrm{T}}(\hat{\boldsymbol{\omega}} - \boldsymbol{\omega}) \\ \hat{\boldsymbol{V}}_w - \boldsymbol{V}_w \end{pmatrix} \tag{6.17}$$

We determine the dynamics of the invariant state error by taking the time derivative of (6.17) and introducing the symmetry-preserving pre-observer defined in [26]:

$$\frac{d}{dt}\hat{\boldsymbol{x}} = \boldsymbol{f}(\hat{\boldsymbol{x}}, \boldsymbol{u}) + \boldsymbol{W}\boldsymbol{K}\boldsymbol{E} \tag{6.18}$$

where $\boldsymbol{K}$ is the $n \times p$ observer gain matrix. The invariant pre-observer is obtained by taking the definition of a pre-observer $(d/dt)\hat{\boldsymbol{x}} = \boldsymbol{F}(\hat{\boldsymbol{x}}, \boldsymbol{u}, \boldsymbol{y})$ and ensuring that it preserves the system geometry by using an invariant output error $\boldsymbol{E}$ where $\boldsymbol{F} = \boldsymbol{f}(\hat{\boldsymbol{x}}, \boldsymbol{u}) + \boldsymbol{W}\boldsymbol{K}\boldsymbol{E}$. Doing

so, we obtain

$$\begin{aligned}\dot{\boldsymbol{\eta}} &= \begin{pmatrix} \dot{\hat{\boldsymbol{X}}} - \dot{\boldsymbol{X}} \\ \dot{\hat{\boldsymbol{\Theta}}} - \dot{\boldsymbol{\Theta}} \\ \dot{\hat{\boldsymbol{R}}}_{\mathrm{IB}}^{\mathrm{T}}(\hat{\boldsymbol{v}}_r - \boldsymbol{v}_r) - \tilde{\boldsymbol{R}}_{\mathrm{IB}}^{\mathrm{T}}(\dot{\hat{\boldsymbol{v}}}_r - \dot{\boldsymbol{v}}_r) \\ \dot{\hat{\boldsymbol{R}}}_{\mathrm{IB}}^{\mathrm{T}}(\hat{\boldsymbol{\omega}} - \boldsymbol{\omega}) - \tilde{\boldsymbol{R}}_{\mathrm{IB}}^{\mathrm{T}}(\dot{\hat{\boldsymbol{\omega}}} - \dot{\boldsymbol{\omega}}) \\ \dot{\hat{\boldsymbol{V}}}_w - \dot{\boldsymbol{V}}_w \end{pmatrix} \\ &= \underbrace{\begin{pmatrix} \hat{\boldsymbol{R}}_{\mathrm{IB}}\hat{\tilde{\boldsymbol{R}}}_{\mathrm{IB}}\boldsymbol{\eta}_{v_r} + (\hat{\boldsymbol{R}}_{\mathrm{IB}} - \boldsymbol{R}_{\mathrm{IB}})\boldsymbol{v}_r + \boldsymbol{\eta}_{V_w}) \\ \hat{\boldsymbol{L}}_{\mathrm{IB}}\hat{\tilde{\boldsymbol{R}}}_{\mathrm{IB}}\boldsymbol{\eta}_{\omega} + (\hat{\boldsymbol{L}}_{\mathrm{IB}} - \boldsymbol{L}_{\mathrm{IB}})\boldsymbol{\omega} \\ \hat{\tilde{\boldsymbol{R}}}_{\mathrm{IB}}(\boldsymbol{\eta}_{v_r} \times \boldsymbol{\eta}_{\omega}) + \boldsymbol{v}_r \times \hat{\tilde{\boldsymbol{R}}}_{\mathrm{IB}}\boldsymbol{\eta}_{\omega} + (\hat{\tilde{\boldsymbol{R}}}_{\mathrm{IB}} + \mathbb{I}_3)\boldsymbol{\eta}_{v_r} \times \boldsymbol{\omega} \\ \hat{\tilde{\boldsymbol{R}}}_{\mathrm{IB}}\boldsymbol{\eta}_{\omega} \times \boldsymbol{I}^{-1}\hat{\tilde{\boldsymbol{R}}}_{\mathrm{IB}}\boldsymbol{\eta}_{\omega} + (\mathbb{I}_3 - \boldsymbol{I}^{-1}\hat{\tilde{\boldsymbol{R}}}_{\mathrm{IB}})\boldsymbol{\eta}_{\omega} \times \boldsymbol{\omega} + \hat{\tilde{\boldsymbol{R}}}_{\mathrm{IB}}\boldsymbol{\eta}_{\omega} \times \boldsymbol{I}^{-1}\boldsymbol{\omega} \\ \boldsymbol{0}_{3\times 1} \end{pmatrix}}_{\boldsymbol{f}_\eta} + \boldsymbol{WKE}\end{aligned} \tag{6.19}$$

Following [39] to design the IEKF, we linearize the invariant state error dynamics about $\boldsymbol{\eta} = \boldsymbol{0}$ to obtain the state matrix

$$\boldsymbol{A}_k = \left.\frac{\partial \boldsymbol{f}_\eta}{\partial \boldsymbol{\eta}}\right|_{\boldsymbol{\eta}=\boldsymbol{0}} = \begin{pmatrix} \boldsymbol{0}_3 & \boldsymbol{0}_3 & \hat{\boldsymbol{R}}_{\mathrm{IB}}\hat{\tilde{\boldsymbol{R}}}_{\mathrm{IB}} & \boldsymbol{0}_3 & \mathbb{I}_3 \\ \boldsymbol{0}_3 & \boldsymbol{0}_3 & \boldsymbol{0}_3 & \hat{\boldsymbol{L}}_{\mathrm{IB}}\hat{\tilde{\boldsymbol{R}}}_{\mathrm{IB}} & \boldsymbol{0}_3 \\ \boldsymbol{0}_3 & \boldsymbol{0}_3 & -\boldsymbol{\omega}^{\times}(\hat{\tilde{\boldsymbol{R}}}_{\mathrm{IB}} + \mathbb{I}_3) & \boldsymbol{v}_r^{\times}\hat{\tilde{\boldsymbol{R}}}_{\mathrm{IB}} & \boldsymbol{0}_3 \\ \boldsymbol{0}_3 & \boldsymbol{0}_3 & \boldsymbol{0}_3 & \begin{matrix} -\boldsymbol{\omega}^{\times} - \boldsymbol{I}^{-1}\boldsymbol{\omega}^{\times}\boldsymbol{I}\hat{\tilde{\boldsymbol{R}}}_{\mathrm{IB}}^{\mathrm{T}} \\ +\boldsymbol{I}^{-1}(\boldsymbol{I}\boldsymbol{\omega})^{\times}\hat{\tilde{\boldsymbol{R}}}_{\mathrm{IB}}^{\mathrm{T}} \end{matrix} & \boldsymbol{0}_3 \\ \boldsymbol{0}_3 & \boldsymbol{0}_3 & \boldsymbol{0}_3 & \boldsymbol{0}_3 & \boldsymbol{0}_3 \end{pmatrix} \tag{6.20}$$

where $\mathbf{0}_3$ denotes a 3×3 matrix of zeros. We also obtain the output matrix

$$\boldsymbol{H}_k = \left.\frac{\partial \boldsymbol{E}}{\partial \boldsymbol{\eta}}\right|_{\boldsymbol{\eta}=\mathbf{0}} = \begin{pmatrix} \mathbb{I}_3 & \mathbf{0}_3 & \mathbf{0}_3 & \mathbf{0}_3 & \mathbf{0}_3 \\ \mathbf{0}_3 & \mathbb{I}_3 & \mathbf{0}_3 & \mathbf{0}_3 & \mathbf{0}_3 \\ \mathbf{0}_3 & \mathbf{0}_3 & \mathbb{I}_3 & \mathbf{0}_3 & \mathbf{0}_3 \\ \mathbf{0}_3 & \mathbf{0}_3 & \mathbf{0}_3 & \mathbb{I}_3 & \mathbf{0}_3 \\ \mathbf{0}_3 & \mathbf{0}_3 & \mathbf{0}_3 & \mathbf{0}_3 & \mathbb{I}_3 \\ \mathbf{0}_3 & \mathbf{0}_3 & \mathbf{0}_3 & \mathbf{0}_3 & \mathbf{0}_3 \\ \mathbf{0}_3 & \mathbf{0}_3 & \mathbf{0}_3 & \mathbf{0}_3 & \mathbf{0}_3 \end{pmatrix} \tag{6.21}$$

Invariant EKF

As with the conventional EKF, the invariant EKF is formulated for systems subject to zero-mean, Gaussian white process and measurement noise. Accordingly, in order to define the invariant EKF, we append to the symmetry-preserving pre-observer (6.18) an $n \times 1$ vector of zero-mean, Gaussian, white process noise $\tilde{\boldsymbol{w}}$ with covariance matrix $\boldsymbol{Q}$. We also append to the output equation (6.11) a $q \times 1$ vector of zero-mean, Gaussian, white measurement noise $\tilde{\boldsymbol{v}}$ with covariance matrix $\boldsymbol{R}$.

The IEKF algorithm is then defined by the following iterative sequence:

1. Initialize the filter with the initial state estimate $\hat{\boldsymbol{x}}(0)$ and state estimate error covariance $\boldsymbol{P}(0)$.

   - Set the iteration index $k = 0$.
   - Set $\hat{\boldsymbol{x}}^+(0) = \hat{\boldsymbol{x}}(0)$
   - Set $\boldsymbol{P}^+(0) = \boldsymbol{W}(0)\boldsymbol{P}(0)\boldsymbol{W}(0)^{\mathrm{T}}$.

2. Model-based prediction: Compute

$$\hat{\boldsymbol{x}}_{k+1}^{-} = \boldsymbol{f}(\hat{\boldsymbol{x}}_{k}^{+}, \boldsymbol{u}_k) \tag{6.22a}$$

$$\boldsymbol{P}_{k+1}^{-} = \boldsymbol{A}_k \boldsymbol{P}_{k}^{+} + \boldsymbol{P}_{k}^{+} \boldsymbol{A}_k^{\mathrm{T}} + \tilde{\boldsymbol{Q}} \tag{6.22b}$$

where $\tilde{\boldsymbol{Q}} = \frac{\partial \boldsymbol{\eta}}{\partial \tilde{\boldsymbol{w}}} \boldsymbol{Q} \frac{\partial \boldsymbol{\eta}}{\partial \tilde{\boldsymbol{w}}}^{\mathrm{T}}$.

3. Measurement-based correction: Compute

$$\boldsymbol{K}_{k+1} = \boldsymbol{P}_{k+1}^{-} \boldsymbol{H}_{k+1}^{\mathrm{T}} \left(\boldsymbol{H}_{k+1} \boldsymbol{P}_{k+1}^{-} \boldsymbol{H}_{k+1}^{\mathrm{T}} + \tilde{\boldsymbol{R}}_{k+1} \right)^{-1} \tag{6.23a}$$

$$\hat{\boldsymbol{x}}_{k+1}^{+} = \hat{\boldsymbol{x}}_{k+1}^{-} + \boldsymbol{W}_{k+1} \boldsymbol{K}_{k+1} \boldsymbol{E}_{k+1} \tag{6.23b}$$

$$\boldsymbol{P}_{k+1}^{+} = \left(\mathbb{I} - \boldsymbol{K}_{k+1} \boldsymbol{H}_{k+1} \right) \boldsymbol{P}_{k+1}^{-} \tag{6.23c}$$

where $\tilde{\boldsymbol{R}}_{k+1} = \boldsymbol{T}_{k+1} \boldsymbol{R} \boldsymbol{T}_{k+1}^{\mathrm{T}}$ and where $\boldsymbol{T}$ was defined following (6.15).

4. Set $k = k + 1$ and return to Step 2.

6.3.2 Convergence of the invariant EKF

The invariant EKF has local convergence guarantees along a *permanent trajectory* [99]. A trajectory of the system (6.2) is permanent if $\bar{\boldsymbol{I}} = \boldsymbol{\psi}_{\boldsymbol{x}^{-1}}(\boldsymbol{u}) = \bar{\boldsymbol{u}}$ where $\bar{\boldsymbol{u}}$ is constant.For the fixed-wing aircraft model (6.1) with input transformation (6.7), the permanent trajectories correspond to flight trajectories along which the following transformed inputs are constant:

$$\bar{\boldsymbol{I}} = \begin{pmatrix} \tilde{\boldsymbol{R}}_{\mathrm{IB}}^{\mathrm{T}} \boldsymbol{a}_A \\ \tilde{\boldsymbol{R}}_{\mathrm{IB}}^{\mathrm{T}} \boldsymbol{\alpha}_A \end{pmatrix} \tag{6.24}$$

There are two qualitatively distinct types of permanent trajectory associated with the constant input indicated by $\bar{\boldsymbol{I}}$. The first type of permanent trajectory corresponds to the case where $\boldsymbol{a}_A = \text{constant}$ and $\boldsymbol{\alpha}_A = \boldsymbol{0}$ so that $\tilde{\boldsymbol{R}}_{\text{IB}} = \text{constant}$. For the general case of this permanent trajectory, the aircraft experiences constant, rectilinear acceleration with a fixed attitude. It might be accelerating forward in wings level, constant altitude flight, for example. The second type of permanent trajectory corresponds to the case where $\boldsymbol{a}_A = \boldsymbol{0}$ and $\tilde{\boldsymbol{R}}_{\text{IB}}^{\text{T}}\boldsymbol{\alpha}_A = \text{constant}$. For the general case of this permanent trajectory, the aircraft moves with constant airspeed along a helical path with constant pitch and radius. This allows for planar rotations with some constant angular acceleration in the direction of rotation. For example, one such trajectory corresponds to rotations about the $\boldsymbol{b}_z$ in the body-fixed reference frame where the inclination of the plane $\boldsymbol{b}_x - \boldsymbol{b}_y$ is constant relative to the North-East plane in the inertial frame with constant acceleration $\boldsymbol{\alpha}_A = (0, 0, \alpha_3)^{\text{T}}$. For such a trajectory, considering, for example, some fixed pitch angle θ^*, zero roll angle ($\phi = 0$), and allowing for the yaw angle ψ to change over time, the quantity $\tilde{\boldsymbol{R}}_{\text{IB}}^{\text{T}}\boldsymbol{\alpha}_A$ becomes

$$\begin{pmatrix} \cos\theta^*\cos\psi & -\cos\theta^*\sin\psi & \sin\theta^* \\ \sin\psi & \cos\psi & 0 \\ -\sin\theta^*\cos\psi & \sin\theta^*\sin\psi & \cos\theta^* \end{pmatrix} \begin{pmatrix} 0 \\ 0 \\ \alpha_3 \end{pmatrix} = \begin{pmatrix} -\alpha_3\sin\theta^* \\ 0 \\ \alpha_3\cos\theta^* \end{pmatrix}$$

which is constant. The invariant EKF has local converge guarantees along such trajectories. The EKF is expected to converge exponentially satisfying conditions listed in [100] where one of the requirements is that the difference between the initial state estimate and the actual initial state is sufficiently small and that the initial state estimate covariance matrix is positive definite.

6.4 Simulation Results and Discussion

The fixed-wing UAV was simulated in two flight conditions corresponding two permanent trajectories introduced in Section 6.3.2 in a 1D von Kármán wind field. The invariant EKF was used to estimate the inertial position, orientation, body velocity, and body angular rate of the aircraft as well as the velocity of the wind. The aircraft was simulated to fly starting from the permanent trajectory corresponding to constant altitude, constantly linearly accelerated wings level flight, and was perturbed from the flight condition with a 10 degree elevator doublet before returning to the permanent trajectory as shown in Fig. 6.1a. In Fig. 6.1b, the aircraft begins from constant altitude, wings-level flight to transition to a non-accelerated helical turn. The desired airspeed in simulation was $V_t = ||\boldsymbol{v}_r|| = 20$ m/s. Process noise was superposed on the dynamics with covariance matrix $\boldsymbol{Q} = \text{diag}(\boldsymbol{0}_6, \sigma_{v_r}^2 \mathbb{I}_3, \sigma_{\omega}^2 \mathbb{I}_3, \sigma_{V_w}^2 \mathbb{I}_3)$ with $\sigma_{v_r} = 0.01$, $\sigma_{\omega} = 0.001$, and $\sigma_{V_w} = 0.05$. Measurement noise with covariance matrix $\boldsymbol{R} = \sigma_v^2 \mathbb{I}_{18}$ with $\sigma_v = 0.01$ was superposed on the output equation. The aerodynamic force and moment coefficients from an identified flight dynamic model of a fixed-wing UAV were used to simulate the motion of the aircraft. All aircraft parameters and model details can be found in Appendix A.0.1.

To initialize the filter, the initial state estimate was set $\hat{\boldsymbol{x}}(0) = (\boldsymbol{X}_0^{\mathrm{T}}, \boldsymbol{\Theta}_0^{\mathrm{T}}, \boldsymbol{v}_0^{\mathrm{T}}, \boldsymbol{\omega}_0^{\mathrm{T}}, \boldsymbol{V}_{w_0}^{\mathrm{T}})^{\mathrm{T}}$ where $\boldsymbol{X}_0 = (0, 0, -200)^{\mathrm{T}}$ m, $\boldsymbol{\Theta}_0 = (\frac{4\pi}{3}, \frac{5\pi}{4}, \frac{7\pi}{6})^{\mathrm{T}}$ rad, $\boldsymbol{v}_0 = (-20, 5, 50)^{\mathrm{T}}$ m/s, $\boldsymbol{\omega}_0 = (5, -5, 1)^{\mathrm{T}}$ rad/s, and $\boldsymbol{V}_{w_0} = (-25, -10, 15)^{\mathrm{T}}$ m/s. The filter was intentionally initialized using an initial condition 'far' from the actual initial condition of the simulated flight data to test if it converges for different initial conditions. The initial state error covariance matrix was set to $\boldsymbol{P}(0) = \mathbb{I}_{15}$. The invariant EKF estimates are compared to estimates using the conventional EKF. Figures 6.2a and 6.3a present results of wind estimation using the invariant EKF and EKF in a 1D von Kármán wind field for both simulated trajectories. The EKF and invariant

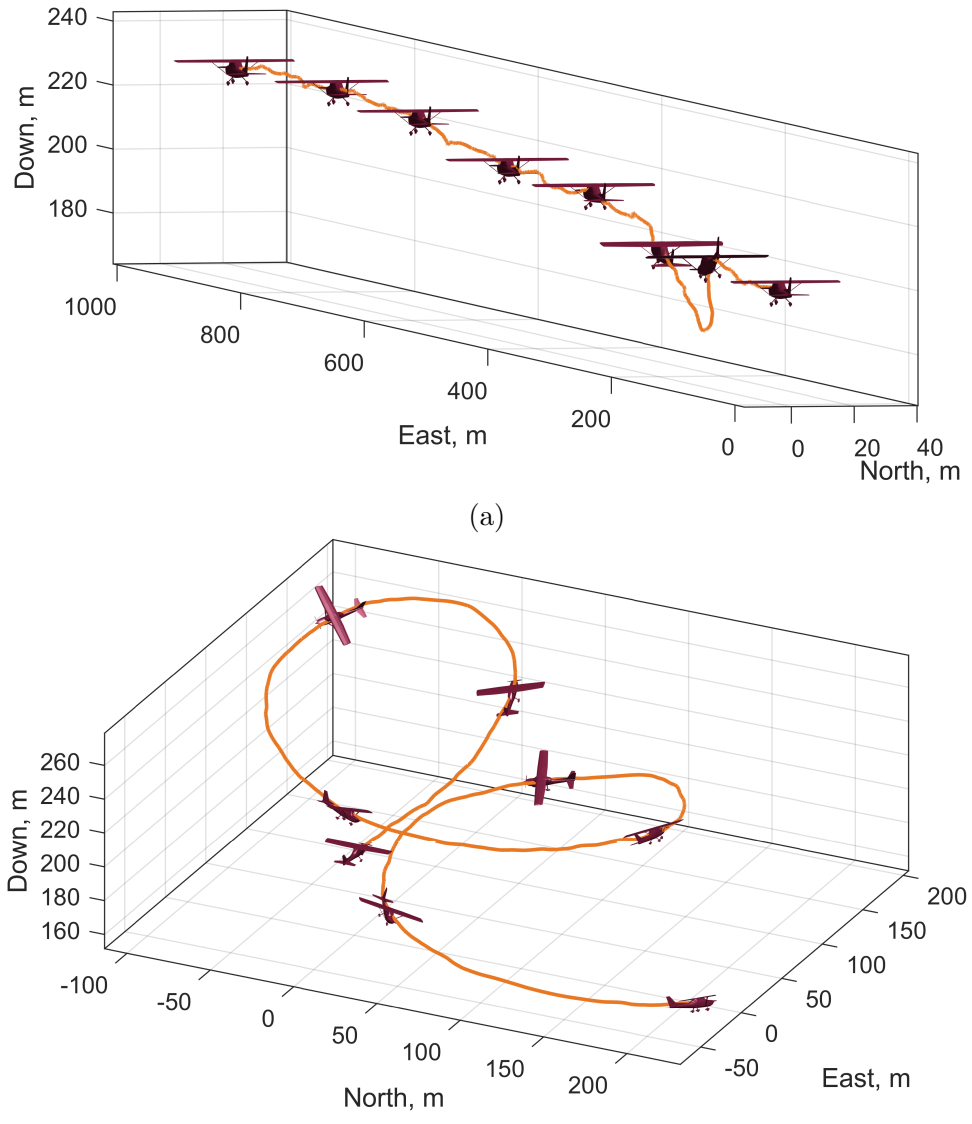

Figure 6.1: Trajectory of the fixed-wing UAV in (a) constant altitude, constantly linearly accelerated wings level flight subject to a 1D von Kármán wind field and (b) a non-accelerated helical turn subject to a 1D von Kármán wind field.

EKF were tuned using the same values for process and measurement noise covariance. A 10-second window of the wind estimation results is presented in Figs. 6.2b and 6.3b. These results show that both the EKF and the invariant EKF perform well in providing accurate estimates of wind velocity, however, it is observed that the invariant EKF outperforms the conventional EKF. In Fig. 6.2, a 10 degree elevator doublet is commanded at $t = 8$ seconds where the aircraft is perturbed from the permanent trajectory corresponding to constant altitude, constantly linearly accelerated wings level flight. The invariant EKF is able to better estimate the wind velocity under this perturbation. In Fig. 6.3, it is shown that the invariant EKF provides more accurate wind estimates when the aircraft is flying along the permanent trajectory corresponding to a non-accelerated helical turn when subject to a 1D von Kármán wind field. The root mean square (RMS) error of the wind velocity estimates for for both simulated cases are presented in Fig. 6.4 where it is observed that the invariant EKF wind estimates have lower RMS error when compared to the EKF wind estimates. The results of state estimation using the invariant EKF and conventional EKF for the remaining 12 states: $(X, Y, Z, \phi, \theta, \psi, u, v, w, p, q, r)$ are provided in Appendix A.0.2.

6.5 Application to Experimental Flight Data

The application of the invariant EKF to experimental flight data requires consideration of the onboard sensor suite of the UAV and available sensor measurements. The fixed-wing UAV used in simulation, the MTD2 aircraft, has available as measurements the GNSS position and velocity of the UAV (in the inertial frame), the attitude of the aircraft from the IMU, and the airspeed from the Pitot probe. The inputs to the system are the specific force and body angular rates from the IMU.

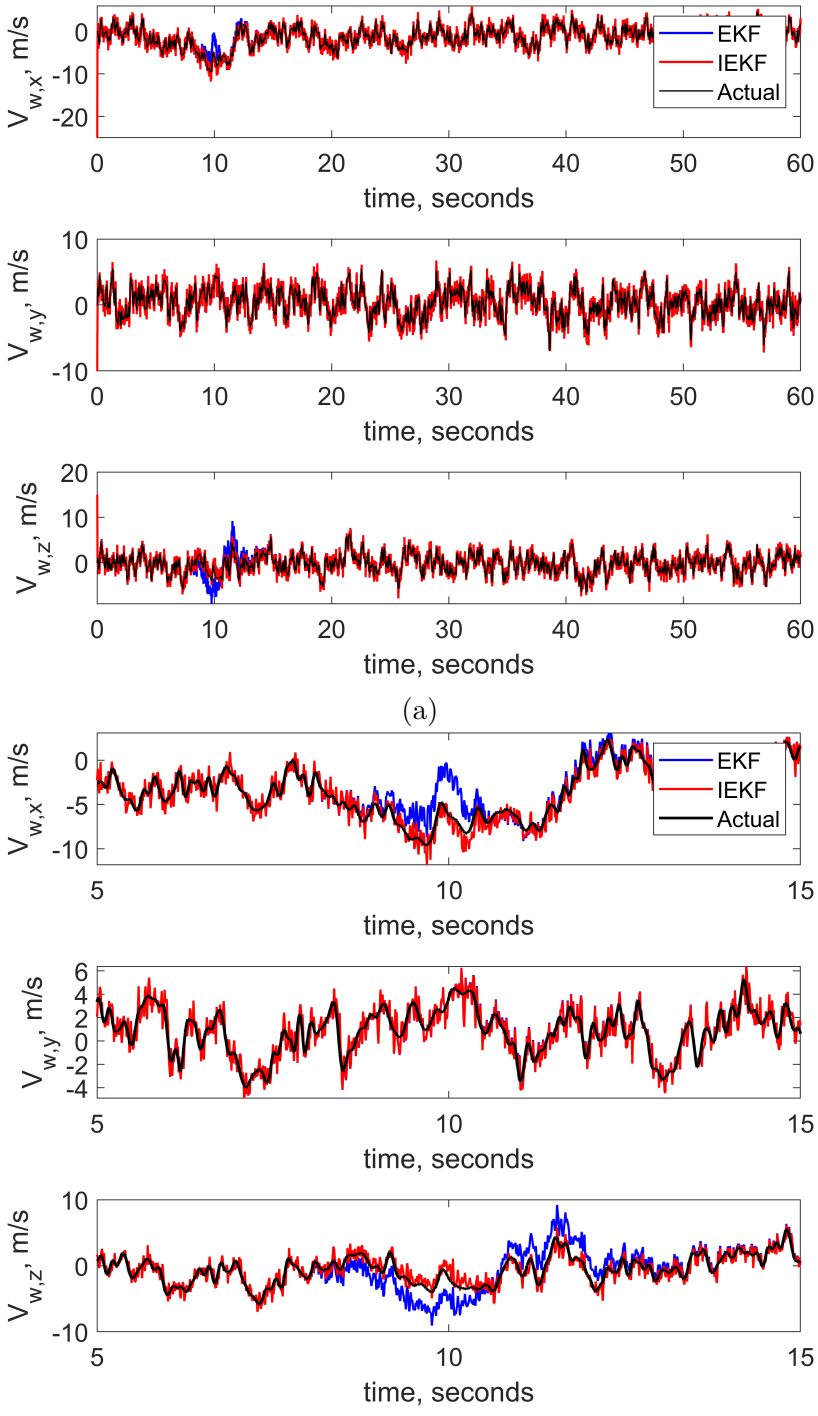

(a)

(b)

Figure 6.2: Wind estimation results using both the invariant EKF and the conventional EKF compared to the actual simulated wind velocity values in constant altitude, wings level flight where an elevator doublet is applied where in (a) the results are shown for the full simulation time and in (b) a 10-second window of the estimates is shown.

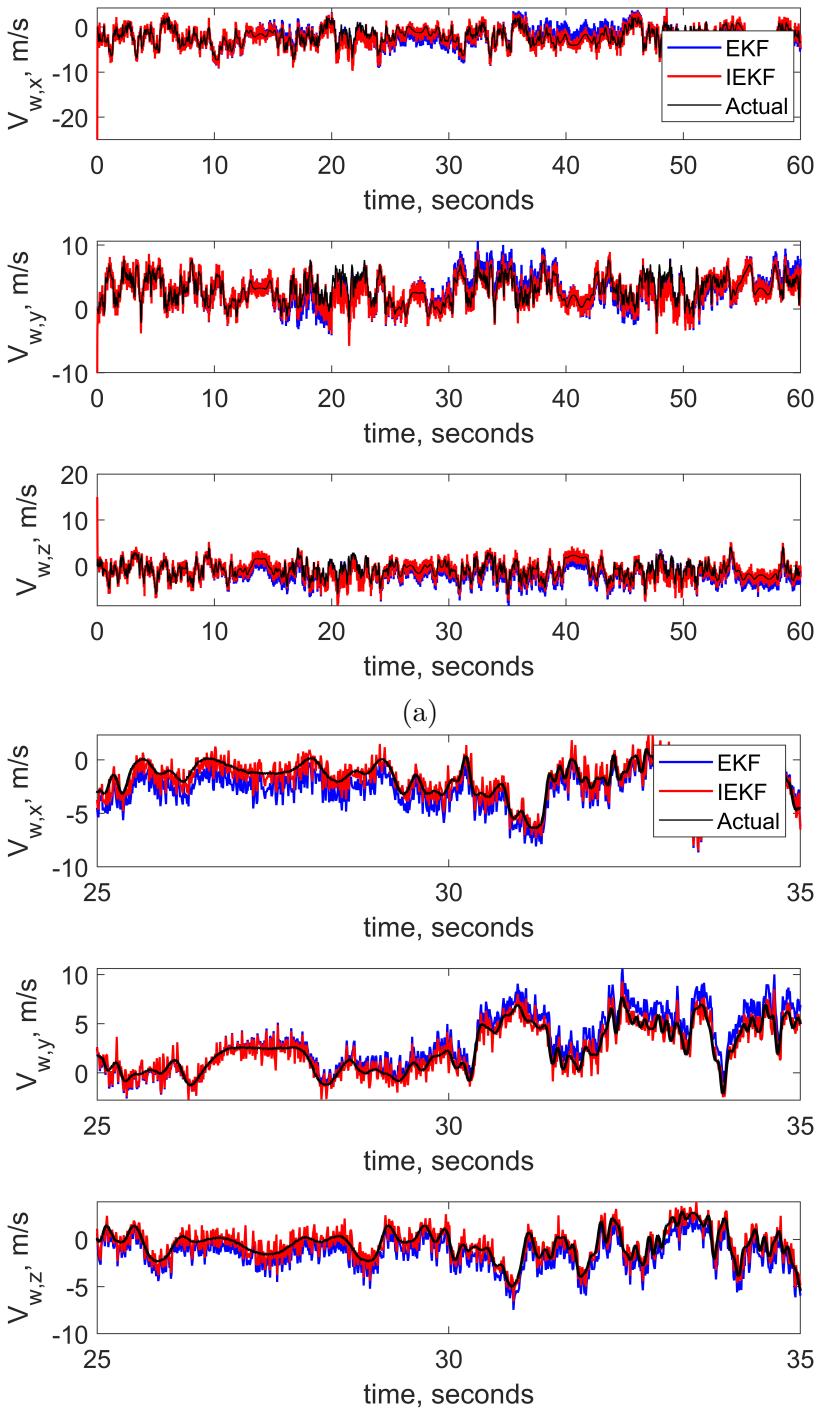

(a)

(b)

Figure 6.3: Wind estimation results using both the invariant EKF and the conventional EKF compared to the actual simulated wind velocity values in flight corresponding a non-accelerated helical turn where in (a) the results are shown for the full simulation time and in (b) a 10-second window of the estimates is shown.

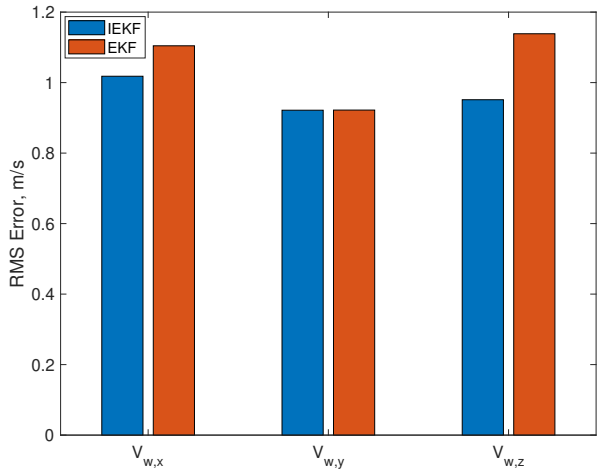

(a)

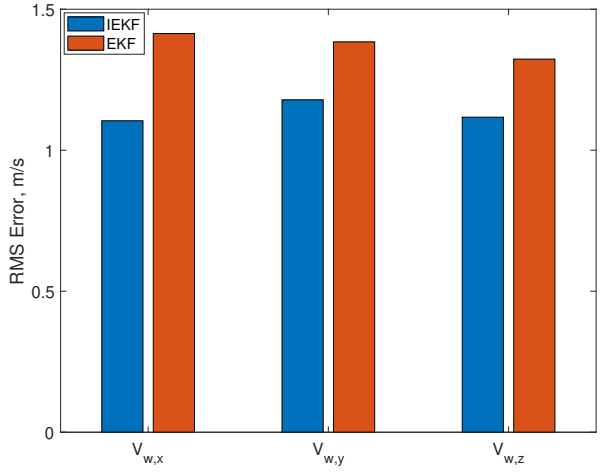

(b)

Figure 6.4: Root mean square error plots of wind estimates obtained using the invariant EKF and a conventional EKF for (a) nominally constant altitude, wings level flight, and (b) a non-accelerated helical turn.

Consider the system

$$\dot{\boldsymbol{x}} = \boldsymbol{f}(\boldsymbol{x}, \boldsymbol{u}) = \begin{pmatrix} \boldsymbol{R}_{\mathrm{IB}}\boldsymbol{v}_{\mathrm{r}} + \boldsymbol{V}_{\mathrm{w}} \\ \boldsymbol{R}_{\mathrm{IB}}\boldsymbol{\omega}^{\times} \\ \boldsymbol{v}_{\mathrm{r}} \times \boldsymbol{\omega} + \boldsymbol{R}_{\mathrm{IB}}^{T}\boldsymbol{g} + \boldsymbol{f}_{A} \\ \boldsymbol{0} \end{pmatrix} \tag{6.25}$$

with state and input given by

$$\boldsymbol{x} = \begin{pmatrix} \boldsymbol{X} \\ \boldsymbol{R}_{\mathrm{IB}} \\ \boldsymbol{v}_{\mathrm{r}} \\ \boldsymbol{V}_{\mathrm{w}} \end{pmatrix} \qquad \text{and} \qquad \boldsymbol{u} = \begin{pmatrix} \boldsymbol{f}_{A} \\ \boldsymbol{\omega} \end{pmatrix}.$$

Here, again, the reader is asked to forgive the abuse of notation in concatenating matrix and vector state and differential equations, as noted earlier in the chapter. The available measurements are

$$\boldsymbol{y} = \begin{pmatrix} \boldsymbol{X} \\ \boldsymbol{R}_{\mathrm{IB}} \\ \boldsymbol{R}_{\mathrm{IB}}\boldsymbol{v}_{\mathrm{r}} + \boldsymbol{V}_{\mathrm{w}} \\ \|\boldsymbol{v}_{\mathrm{r}}\| \end{pmatrix}. \tag{6.26}$$

Proposition 6.6. *The dynamics (6.25) are invariant under the left action of $SE(3)$ on the state and input as given below:*

$$\boldsymbol{\phi}_{g}(\boldsymbol{x}) = \begin{pmatrix} \boldsymbol{X} + \boldsymbol{X}_{g} \\ \boldsymbol{R}_{IB}\boldsymbol{R}_{g}^{\mathrm{T}} \\ \boldsymbol{R}_{g}\boldsymbol{v}_{r} \\ \boldsymbol{V}_{w} \end{pmatrix} \tag{6.27}$$

and

$$\boldsymbol{\psi}_g(\boldsymbol{u}) = \begin{pmatrix} \boldsymbol{R}_g \boldsymbol{f}_A \\ \boldsymbol{R}_g \boldsymbol{\omega} \end{pmatrix} \tag{6.28}$$

Proof. According to the definition (6.5a) with state and input transformations (6.27) and (6.28), respectively, the system is invariant if it satisfies the condition $\frac{d}{dt}\boldsymbol{\mathcal{X}} = \boldsymbol{f}(\boldsymbol{\phi}_g(\boldsymbol{x}), \boldsymbol{\psi}_g(\boldsymbol{u}))$, for all $g \in G$ and for all $\boldsymbol{x}$ and $\boldsymbol{u}$. The dynamics of the transformed state are written as

$$\frac{d}{dt}\begin{pmatrix} \boldsymbol{X} + \boldsymbol{X}_g \\ \boldsymbol{R}_{\mathrm{IB}}\boldsymbol{R}_g^{\mathrm{T}} \\ \boldsymbol{R}_g \boldsymbol{v}_r \\ \boldsymbol{V}_w \end{pmatrix} = \begin{pmatrix} \boldsymbol{R}_{\mathrm{IB}}\boldsymbol{R}_g^{\mathrm{T}}\boldsymbol{R}_g\boldsymbol{v}_r + \boldsymbol{V}_w \\ \boldsymbol{R}_{\mathrm{IB}}\boldsymbol{R}_g^{\mathrm{T}}\boldsymbol{R}_g\boldsymbol{\omega}^{\times}\boldsymbol{R}_g^{\mathrm{T}} \\ \boldsymbol{R}_g\boldsymbol{v}_r \times \boldsymbol{R}_g\boldsymbol{\omega} + \boldsymbol{R}_g\boldsymbol{f}_A + \frac{1}{m}\boldsymbol{R}_g\boldsymbol{R}_{\mathrm{IB}}^{\mathrm{T}}\boldsymbol{F}_g \\ \boldsymbol{0} \end{pmatrix}$$

or

$$\begin{pmatrix} \dot{\boldsymbol{X}} \\ \dot{\boldsymbol{R}}_{\mathrm{IB}}\boldsymbol{R}_g^{\mathrm{T}} \\ \boldsymbol{R}_g\dot{\boldsymbol{v}}_r \\ \dot{\boldsymbol{V}}_w \end{pmatrix} = \begin{pmatrix} \boldsymbol{R}_{\mathrm{IB}}\boldsymbol{v}_r + \boldsymbol{V}_w \\ \boldsymbol{R}_{\mathrm{IB}}\boldsymbol{\omega}^{\times}\boldsymbol{R}_g^{\mathrm{T}} \\ \boldsymbol{R}_g(\boldsymbol{v}_r \times \boldsymbol{\omega} + \boldsymbol{f}_A + \frac{1}{m}\boldsymbol{R}_{\mathrm{IB}}^{\mathrm{T}}\boldsymbol{F}_g) \\ \boldsymbol{0} \end{pmatrix}$$

The dynamics under the transformations $\boldsymbol{\phi}_g$ and $\boldsymbol{\psi}_g$ satisfy the condition (6.5a), thus the system described by Eq. (6.25) is invariant under the transformations (6.27) and (6.28). □

Proposition 6.7. *The output (6.26) is equivariant under the left action of $SE(3)$ with state*

and input transformations $\boldsymbol{\phi}_g(\boldsymbol{x})$ *and* $\boldsymbol{\psi}_g(\boldsymbol{u})$*, respectively, with output transformation*

$$\boldsymbol{\rho}_g(\boldsymbol{y}) = \begin{pmatrix} \boldsymbol{X} + \boldsymbol{X}_g \\ \boldsymbol{R}_{\mathrm{IB}} \boldsymbol{R}_g^{\mathrm{T}} \\ \boldsymbol{R}_{\mathrm{IB}} \boldsymbol{v}_{\mathrm{r}} + \boldsymbol{V}_{\mathrm{w}} \\ \|\boldsymbol{v}_{\mathrm{r}}\| \end{pmatrix} \tag{6.29}$$

Proof. Using the defined output transformation (6.29) it can be shown that condition (6.5b) is satisfied.

$$\begin{aligned} \boldsymbol{\rho}_g(\boldsymbol{y}) &= \boldsymbol{y}(\boldsymbol{\phi}_g(\boldsymbol{x}), \boldsymbol{\psi}_g(\boldsymbol{u})) \\ \begin{pmatrix} \boldsymbol{X} + \boldsymbol{X}_g \\ \boldsymbol{R}_{\mathrm{IB}} \boldsymbol{R}_g^{\mathrm{T}} \\ \boldsymbol{R}_{\mathrm{IB}} \boldsymbol{R}_g^{\mathrm{T}} \boldsymbol{R}_g \boldsymbol{v}_{\mathrm{r}} + \boldsymbol{V}_{\mathrm{w}} \\ \|\boldsymbol{R}_g \boldsymbol{v}_{\mathrm{r}}\| \end{pmatrix} &= \begin{pmatrix} \boldsymbol{X} + \boldsymbol{X}_g \\ \boldsymbol{R}_{\mathrm{IB}} \boldsymbol{R}_g^{\mathrm{T}} \\ \boldsymbol{R}_{\mathrm{IB}} \boldsymbol{v}_{\mathrm{r}} + \boldsymbol{V}_{\mathrm{w}} \\ \|\boldsymbol{v}_{\mathrm{r}}\| \end{pmatrix} \end{aligned}$$

The transformed output satisfies the condition (6.5b), thus the output equation (6.26) is $SE(3)$-equivariant. □

The steps to design the invariant EKF presented in Section 6.3 are followed to obtain the state and output matrices for implementation of the invariant EKF algorithm. First, the attitude kinematics given by

$$\dot{\boldsymbol{R}}_{\mathrm{IB}} = \boldsymbol{R}_{\mathrm{IB}} \boldsymbol{\omega}^{\times}$$

are replaced by using the kinematics described by the Euler angle parameterization of the rotation matrix:

$$\dot{\boldsymbol{\Theta}} = \boldsymbol{L}_{\mathrm{IB}} \boldsymbol{\omega} \tag{6.30}$$

where $\boldsymbol{L}_{\mathrm{IB}}$ is given in Eq. (6.9). The modified nonlinear dynamics, state, and state transformation, respectively, are

$$\dot{\boldsymbol{x}} = \boldsymbol{f}(\boldsymbol{x}, \boldsymbol{u}) = \begin{pmatrix} \boldsymbol{R}_{\mathrm{IB}}\boldsymbol{v}_{\mathrm{r}} + \boldsymbol{V}_{\mathrm{w}} \\ \boldsymbol{L}_{\mathrm{IB}}\boldsymbol{\omega} \\ \boldsymbol{v}_{\mathrm{r}} \times \boldsymbol{\omega} + \boldsymbol{R}_{\mathrm{IB}}^{T}\boldsymbol{g} + \boldsymbol{f}_{A} \\ \boldsymbol{0} \end{pmatrix}, \tag{6.31}$$

$$\boldsymbol{x} = \begin{pmatrix} \boldsymbol{X} \\ \boldsymbol{\Theta} \\ \boldsymbol{v}_{\mathrm{r}} \\ \boldsymbol{V}_{\mathrm{w}} \end{pmatrix},$$

and

$$\boldsymbol{\phi}_{g}(\boldsymbol{x}) = \begin{pmatrix} \boldsymbol{X} + \boldsymbol{X}_{g} \\ \boldsymbol{\Theta} + \boldsymbol{\Theta}_{g} \\ \boldsymbol{R}_{g}\boldsymbol{v}_{\mathrm{r}} \\ \boldsymbol{V}_{\mathrm{w}} \end{pmatrix}. \tag{6.32}$$

The six normalization equations are then

$$\boldsymbol{\phi}_{g}^{a} = \begin{pmatrix} \boldsymbol{X} + \boldsymbol{X}_{g} \\ \boldsymbol{\Theta} + \boldsymbol{\Theta}_{g} \end{pmatrix} \tag{6.33}$$

where the solution is given by

$$\boldsymbol{\gamma}(\boldsymbol{x}) = \begin{pmatrix} \boldsymbol{X} \\ \boldsymbol{\Theta} \end{pmatrix}^{-1} \tag{6.34}$$

where, recall that, $(\cdot)^{-1}$ denotes the inverse action. The scalar invariants are then

$$\hat{\boldsymbol{I}}(\hat{\boldsymbol{x}}, \boldsymbol{u}) = \begin{pmatrix} \boldsymbol{\phi}_g^b \\ \boldsymbol{\psi}_{\boldsymbol{\gamma}(\hat{\boldsymbol{x}})}(\boldsymbol{u}) \end{pmatrix} = \begin{pmatrix} \boldsymbol{R}_{\boldsymbol{\gamma}(\hat{\boldsymbol{x}})} \boldsymbol{v}_{\mathrm{r}} \\ \boldsymbol{V}_{\mathrm{w}} \\ \boldsymbol{R}_{\boldsymbol{\gamma}(\hat{\boldsymbol{x}})} \boldsymbol{f}_A \\ \boldsymbol{R}_{\boldsymbol{\gamma}(\hat{\boldsymbol{x}})} \boldsymbol{\omega} \end{pmatrix} \tag{6.35}$$

The invariant output error $\boldsymbol{E}$ is

$$\boldsymbol{E} = \boldsymbol{T} \begin{pmatrix} \hat{\boldsymbol{X}} - \boldsymbol{X} \\ \hat{\boldsymbol{\Theta}} - \boldsymbol{\Theta} \\ \hat{\boldsymbol{R}}_{\mathrm{IB}} \hat{\boldsymbol{v}}_{\mathrm{r}} + \hat{\boldsymbol{V}}_{\mathrm{w}} - \boldsymbol{R}_{\mathrm{IB}} \boldsymbol{v}_{\mathrm{r}} - \boldsymbol{V}_{\mathrm{w}} \\ \|\hat{\boldsymbol{v}}_{\mathrm{r}}\| - \|\boldsymbol{v}_{\mathrm{r}}\| \end{pmatrix} \tag{6.36}$$

where $\boldsymbol{T} = \mathbb{I}_{10}$. The invariant frame defined in Section 6.3.1 is $\boldsymbol{W} = \mathrm{diag}(\mathbb{I}_3, \mathbb{I}_3, \boldsymbol{R}_{\boldsymbol{\gamma}(\hat{\boldsymbol{x}})}, \mathbb{I}_3)$. The invariant state estimate error $\boldsymbol{\eta}$ is determined to be

$$\boldsymbol{\eta} = \begin{pmatrix} \boldsymbol{\eta}_X \\ \boldsymbol{\eta}_\Theta \\ \boldsymbol{\eta}_{v_{\mathrm{r}}} \\ \boldsymbol{\eta}_{V_{\mathrm{w}}} \end{pmatrix} = \begin{pmatrix} \hat{\boldsymbol{X}} - \boldsymbol{X} \\ \hat{\boldsymbol{\Theta}} - \boldsymbol{\Theta} \\ \boldsymbol{R}_{\boldsymbol{\gamma}(\hat{\boldsymbol{x}})}(\hat{\boldsymbol{v}}_{\mathrm{r}} - \boldsymbol{v}_{\mathrm{r}}) \\ \hat{\boldsymbol{V}}_{\mathrm{w}} - \boldsymbol{V}_{\mathrm{w}} \end{pmatrix} \tag{6.37}$$

Finally, the invariant state estimate error dynamics $\dot{\boldsymbol{\eta}}$, using the defined symmetry-preserving

pre-observer in [26], are

$$\dot{\boldsymbol{\eta}} = \underbrace{\begin{pmatrix} \hat{\boldsymbol{R}}_{\mathrm{IB}} \boldsymbol{R}^{\mathrm{T}}_{\boldsymbol{\gamma}(\hat{\boldsymbol{x}})} \boldsymbol{\eta}_{v_{\mathrm{r}}} + (\hat{\boldsymbol{R}}_{\mathrm{IB}} - \boldsymbol{R}_{\mathrm{IB}}) \boldsymbol{v}_{\mathrm{r}} + \boldsymbol{\eta}_{V_{\mathrm{w}}} \\ (\hat{\boldsymbol{L}}_{\mathrm{IB}} - \boldsymbol{L}_{\mathrm{IB}}) \boldsymbol{\omega} \\ \boldsymbol{R}_{\boldsymbol{\gamma}(\hat{\boldsymbol{x}})} \left(\boldsymbol{R}^{\mathrm{T}}_{\boldsymbol{\gamma}(\hat{\boldsymbol{x}})} \boldsymbol{\eta}_{v_{\mathrm{r}}} \times \boldsymbol{\omega} + (\hat{\boldsymbol{R}}^{\mathrm{T}}_{\mathrm{IB}} - \boldsymbol{R}^{\mathrm{T}}_{\mathrm{IB}}) \boldsymbol{g} \right) \\ \boldsymbol{0} \end{pmatrix}}_{\boldsymbol{f}_{\eta}} + \boldsymbol{W} \boldsymbol{K} \boldsymbol{E} \tag{6.38}$$

The state matrix $\boldsymbol{A}_k$ is found by linearizing the invariant state estimate error dynamics (6.38) about zero state estimate error, *i.e.*,

$$\boldsymbol{A}_k = \left. \frac{\partial \boldsymbol{f}_{\eta}}{\partial \boldsymbol{\eta}} \right|_{\eta = \boldsymbol{0}} = \begin{pmatrix} \boldsymbol{0}_3 & \boldsymbol{0}_3 & \hat{\boldsymbol{R}}_{\mathrm{IB}} \boldsymbol{R}^{\mathrm{T}}_{\boldsymbol{\gamma}(\hat{\boldsymbol{x}})} & \mathbb{I}_3 \\ \boldsymbol{0}_3 & \boldsymbol{0}_3 & \boldsymbol{0}_3 & \boldsymbol{0}_3 \\ \boldsymbol{0}_3 & \boldsymbol{0}_3 & -\boldsymbol{R}_{\boldsymbol{\gamma}(\hat{\boldsymbol{x}})} \boldsymbol{\omega}^{\times} \boldsymbol{R}^{\mathrm{T}}_{\boldsymbol{\gamma}(\hat{\boldsymbol{x}})} & \boldsymbol{0}_3 \\ \boldsymbol{0}_3 & \boldsymbol{0}_3 & \boldsymbol{0}_3 & \boldsymbol{0}_3 \end{pmatrix} \tag{6.39}$$

The output matrix $\boldsymbol{H}_k$ is determined by linearizing the invariant output error (6.36) about zero invariant state estimate error. The invariant output error $\boldsymbol{E}$ in Eq. (6.36) is rewritten in terms of the invariant state estimate error $\boldsymbol{\eta}$ as

$$\boldsymbol{E} = \boldsymbol{T} \begin{pmatrix} \boldsymbol{\eta}_X \\ \boldsymbol{\eta}_{\Theta} \\ \hat{\boldsymbol{R}}_{\mathrm{IB}} \boldsymbol{R}^{\mathrm{T}}_{\boldsymbol{\gamma}(\hat{\boldsymbol{x}})} \boldsymbol{\eta}_{v_{\mathrm{r}}} + (\hat{\boldsymbol{R}}_{\mathrm{IB}} - \boldsymbol{R}_{\mathrm{IB}}) \boldsymbol{v}_{\mathrm{r}} + \boldsymbol{\eta}_{V_{\mathrm{w}}} \\ \| \boldsymbol{R}^{\mathrm{T}}_{\boldsymbol{\gamma}(\hat{\boldsymbol{x}})} \boldsymbol{\eta}_{v_{\mathrm{r}}} + \boldsymbol{v}_{\mathrm{r}} \| - \| \boldsymbol{v}_{\mathrm{r}} \| \end{pmatrix} \tag{6.40}$$

The output matrix is then

$$\boldsymbol{H}_k = \left.\frac{\partial \boldsymbol{E}}{\partial \boldsymbol{\eta}}\right|_{\boldsymbol{\eta}=\mathbf{0}} = \begin{pmatrix} \mathbb{I}_3 & \mathbf{0}_3 & \mathbf{0}_3 & \mathbf{0}_3 \\ \mathbf{0}_3 & \mathbb{I}_3 & \mathbf{0}_3 & \mathbf{0}_3 \\ \mathbf{0}_3 & \mathbf{0}_3 & \hat{\boldsymbol{R}}_{\mathrm{IB}} \boldsymbol{R}^{\mathrm{T}}_{\boldsymbol{\gamma}(\hat{\boldsymbol{x}})} & \mathbb{I}_3 \\ \mathbf{0}_{1\times 3} & \mathbf{0}_{1\times 3} & \left(\frac{\boldsymbol{R}_{\boldsymbol{\gamma}(\hat{\boldsymbol{x}})}\boldsymbol{v}_{\mathrm{r}}}{\|\boldsymbol{v}_{\mathrm{r}}\|}\right)^{\mathrm{T}} & \mathbf{0}_{1\times 3} \end{pmatrix} \tag{6.41}$$

Local Observability for the invariant EKF

A simple observability analysis of the invariant EKF at each iteration can be computed using the state and output matrices (6.39) and (6.41), respectively. The observability matrix at each iteration of the filter k is given by

$$\mathcal{O}_k = \begin{pmatrix} \boldsymbol{H}_k \\ \boldsymbol{H}_k \boldsymbol{A}_k \\ \boldsymbol{H}_k \boldsymbol{A}_k^2 \\ \vdots \\ \boldsymbol{H}_k \boldsymbol{A}_k^{n-1} \end{pmatrix}$$

where $n = 12$ for the system (6.25). For the linearized system to be observable, the observability matrix must have full column rank at the given iteration of the filter at time step k. A fundamental result in linear algebra is that column rank is equal to row rank, thus if the observability matrix at iteration k has full row rank, the system is observable at step k. The

observability matrix for the system is then

$$\mathcal{O}_k = \begin{pmatrix} \mathbb{I}_3 & \mathbf{0}_3 & \mathbf{0}_3 & \mathbf{0}_3 \\ \mathbf{0}_3 & \mathbb{I}_3 & \mathbf{0}_3 & \mathbf{0}_3 \\ \mathbf{0}_3 & \mathbf{0}_3 & \hat{\boldsymbol{R}}_{\mathrm{IB}} \boldsymbol{R}^{\mathrm{T}}_{\boldsymbol{\gamma}(\hat{\boldsymbol{x}})} & \mathbb{I}_3 \\ \mathbf{0}_{1\times 3} & \mathbf{0}_{1\times 3} & \left(\frac{\boldsymbol{R}_{\boldsymbol{\gamma}(\hat{\boldsymbol{x}})}\boldsymbol{v}_{\mathrm{r}}}{\|\boldsymbol{v}_{\mathrm{r}}\|}\right)^{\mathrm{T}} & \mathbf{0}_{1\times 3} \\ \mathbf{0}_3 & \mathbf{0}_3 & \hat{\boldsymbol{R}}_{\mathrm{IB}} \boldsymbol{R}^{\mathrm{T}}_{\boldsymbol{\gamma}(\hat{\boldsymbol{x}})} & \mathbb{I}_3 \\ \mathbf{0}_3 & \mathbf{0}_3 & \mathbf{0}_3 & \mathbf{0}_3 \\ \mathbf{0}_3 & \mathbf{0}_3 & -\hat{\boldsymbol{R}}_{\mathrm{IB}} \boldsymbol{\omega}^{\times} \boldsymbol{R}^{\mathrm{T}}_{\boldsymbol{\gamma}(\hat{\boldsymbol{x}})} & \mathbf{0}_3 \\ \mathbf{0}_{1\times 3} & \mathbf{0}_{1\times 3} & -\left(\frac{\boldsymbol{R}_{\boldsymbol{\gamma}(\hat{\boldsymbol{x}})}\boldsymbol{v}_{\mathrm{r}}}{\|\boldsymbol{v}_{\mathrm{r}}\|}\right)^{\mathrm{T}} \boldsymbol{R}_{\boldsymbol{\gamma}(\hat{\boldsymbol{x}})} \boldsymbol{\omega}^{\times} \boldsymbol{R}^{\mathrm{T}}_{\boldsymbol{\gamma}(\hat{\boldsymbol{x}})} & \mathbf{0}_{1\times 3} \\ & & \mathbf{0}_{100\times 12} & \end{pmatrix} \tag{6.42}$$

The observability matrix (6.42) has full row rank, rank($\mathcal{O}_k = 12$), for all values of $\boldsymbol{\Theta}$ (avoiding the singularity of the Euler angle parameterization at $\theta = \pm\frac{\pi}{2}$), for $\|\boldsymbol{v}_r\| \neq 0$, and if at least one component of $\boldsymbol{\omega}$ is non-zero.

Experiment Description and Results

The invariant EKF using the state and output matrices in Eqs. (6.39) and (6.41), respectively, was implemented on two sets of collected flight data using the MTD2 aircraft shown in Fig. 6.5 for indirect wind velocity estimation. The results obtained using the invariant EKF were compared to those obtained using a conventional EKF. The experimental flight profile flown by the MTD2 was the grid pattern flown at 210 m above ground level at a cruise speed of 18 m/s shown in Fig. 6.6. Two portions of the flight profile were chosen to obtain wind estimates using both the invariant EKF and a conventional EKF. Further details on the experimental flight profile are in [101]. The trajectories for the two sets of flight data

are shown in Fig. 6.7 where the trajectory of the first flight corresponds to straight and level flight and the second corresponds to a coordinated turn.

Figure 6.5: The MTD2 aircraft.

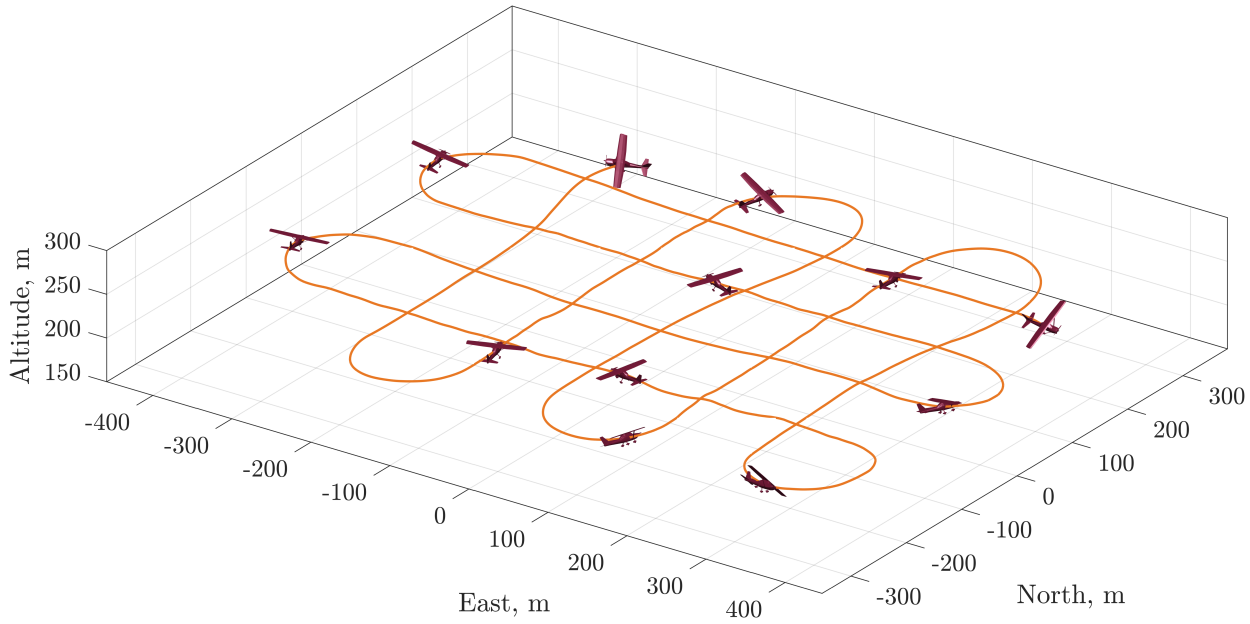

Figure 6.6: Experimental flight profile of the MTD2 from which two sets of flight data were chosen.

The results of wind estimation using the invariant EKF on the two trajectories shown in Fig. 6.7 are shown in Figs. 6.8 and 6.9. The reconstructed, or measured, wind velocity that is considered the *actual* wind velocity is obtained from an air data system onboard the MTD2 aircraft. The air data system measures the airspeed $\|\boldsymbol{v}_r\|$ of the aircraft using a Kiel probe, as well as the AoA α and flank angle β_f using two flow vanes. The flank angle and AoA are

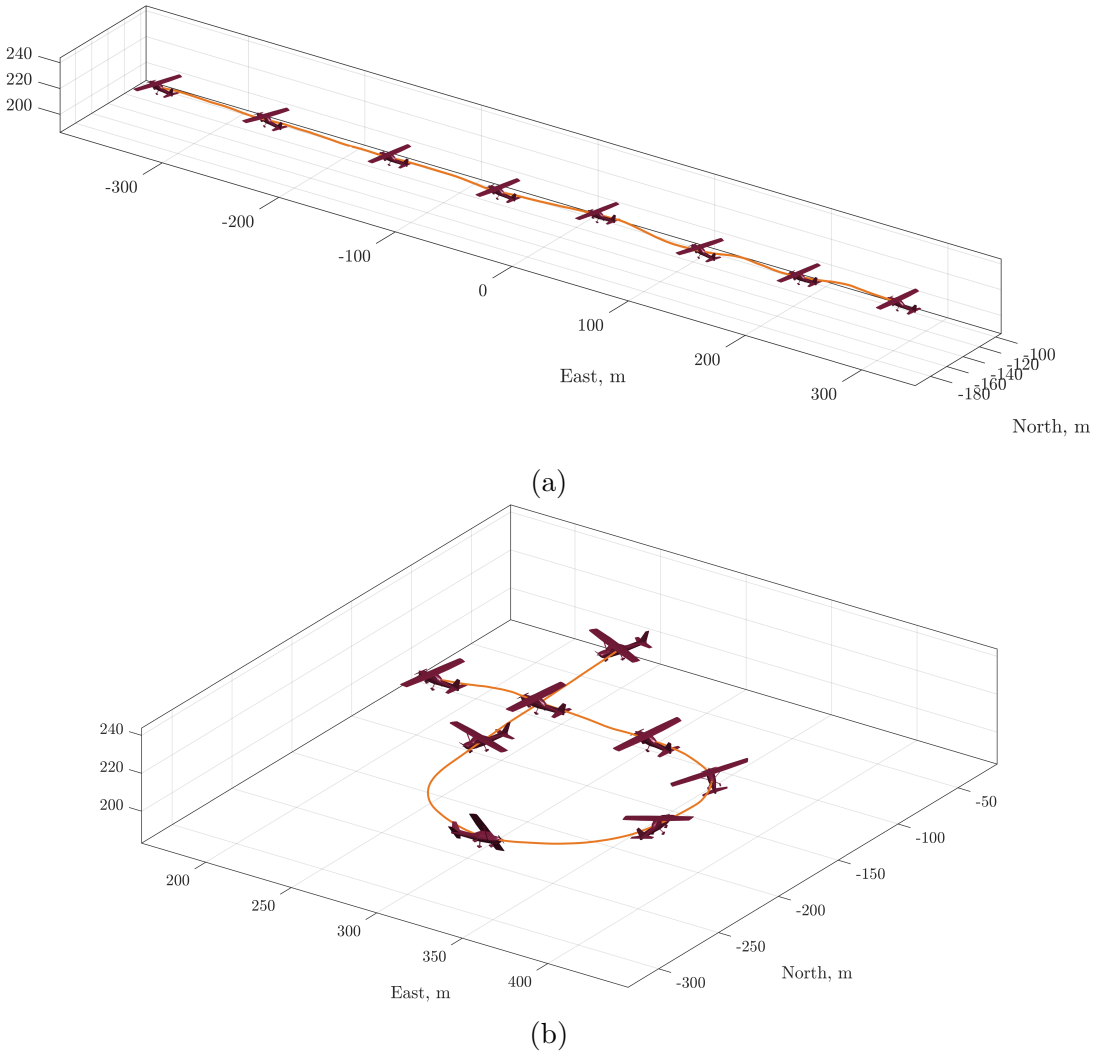

Figure 6.7: Two trajectories of collected experimental flight data where in (a) the UAV is in straight and level flight and in (b) the UAV is executing a coordinated turn.

used to obtain AoS β using the relationship $\beta = \tan^{-1}(\tan(\beta_f)\cos(\alpha))$. The components of the air-relative velocity $\boldsymbol{v}_r$ of the aircraft are determined using the measurements of $\|\boldsymbol{v}_r\|$, α, and β. The inertial velocity $\boldsymbol{V}$ of the aircraft is obtained from the GNSS receiver. The wind triangle shown in Fig. 3.1 is then solved for wind velocity $\boldsymbol{V}_\text{w}$ where $\boldsymbol{V}_\text{w} = \boldsymbol{V} - \boldsymbol{R}_\text{IB}\boldsymbol{v}_r$. The rotation matrix $\boldsymbol{R}_\text{IB}$ is obtained from the onboard navigation solution and IMU. This computed wind velocity is then used as the actual wind velocity that the wind velocity estimates from the implemented filters are compared to. It is important to note that the *true* wind velocity is unknown and the reconstructed, or actual wind velocity values obtained are as accurate as the information collected by the air data system. The obtained wind estimates are compared to the actual wind velocity values in Figs. 6.8 and 6.9. Additional state estimates of the position, attitude, and inertial velocity can be found in Appendix A.0.3 for both experimental flight trajectories. Both the invariant EKF and EKF were initialized with an initial state estimate covariance $\boldsymbol{P}_0 = 10 \cdot \mathbb{I}_{12}$ and initial states for the straight and level flight and coordinated turn

$$\boldsymbol{x}_0 = (-143.3, 295.8, -214.6, -0.0584, 0.0568, -1.378, 19.01, 0.6251, 0.1218, -5.101, 5.481, -0.4321)^\text{T}$$

and

$$\boldsymbol{x}_0 = (-67.17, 262.9, -214.8, -0.0544, -0.0060, -2.760, 18.79, 0.3138, 0.7232, -5.234, 6.971, 0.8164)^\text{T},$$

respectively, with commensurate units. The process noise covariance in straight and level flight was set to

$$\boldsymbol{Q} = \text{diag}(39.38, 44.08, 22.54, 0.0044, 3.158e{-}4, 7.155e{-}4, 2.880, 8.176, 7.751, 7.797, 3.346, 6.220),$$

with commensurate units. For the coordinated turn, the process noise covariance was set to

$$\boldsymbol{Q} = \text{diag}(13.55, 15.77, 20.49, 0.0087, 2.681e-4, 2.705, 2.768, 6.990, 5.650, 3.871, 3.214, 5.316),$$

with commensurate units. For both sets of flight data, the measurement noise covariance was set to

$$\boldsymbol{R} = \text{diag}(0.0291, 0.0294, 0.1563, 1e-6, 1e-6, 1e-6, 0.0093, 0.0095, 0.0119, 4e-4),$$

with commensurate units.

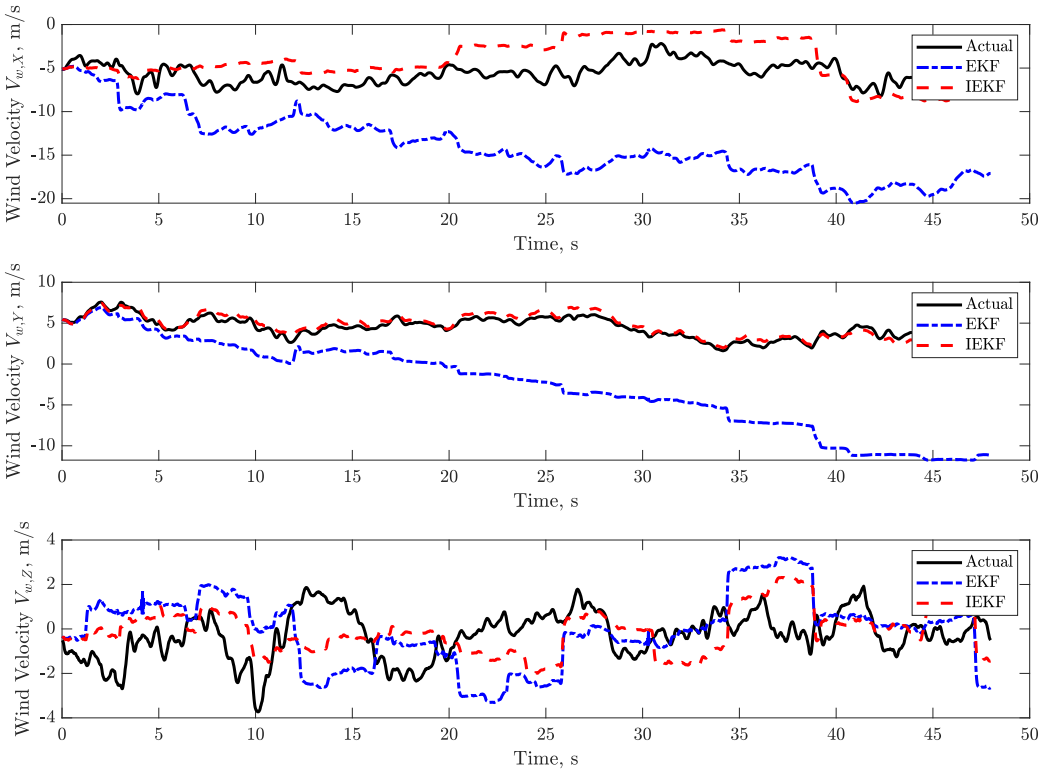

Figure 6.8: Wind estimation results using both the invariant EKF and conventional EKF compared to reconstructed (or measured) wind velocity using an air data system (denoted actual) on straight and level flight.

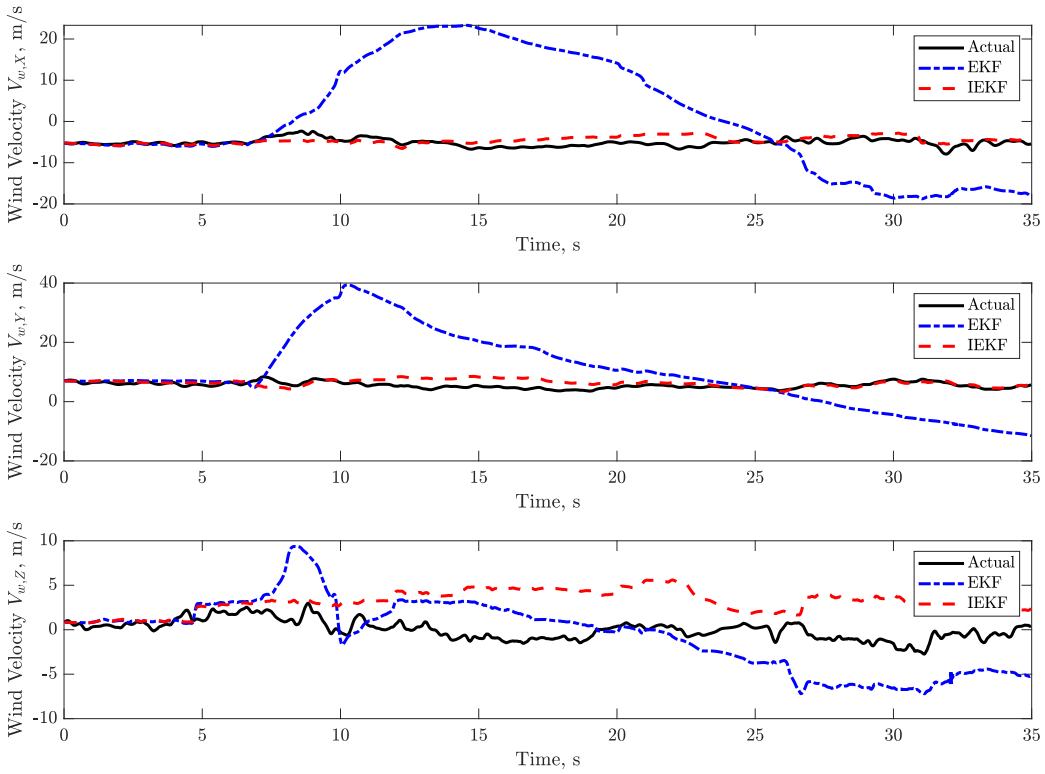

Figure 6.9: Wind estimation results using both the invariant EKF and conventional EKF compared to reconstructed (or measured) wind velocity using an air data system (denoted actual) when the aircraft executes a coordinated turn.

Figures 6.8 and 6.9 show that the invariant EKF outperforms the EKF in providing accurate wind velocity estimates. The EKF diverges from the actual wind velocity in both experimental data sets. The invariant EKF is thus shown to be capable of aerodynamic model-free indirect wind estimation. This work is the first application of the invariant EKF for indirect wind estimation using a small, fixed-wing UAV for both simulated and experimental flight data. It also shows that aerodynamic model-free indirect wind estimation is possible using the invariant EKF, as demonstrated in Figs. 6.3, 6.2, 6.8 and 6.9, where the most notable contribution is the successful implementation of the invariant EKF to obtain accurate wind estimates on experimental flight data. The ability of the invariant EKF on this application

establishes the effectiveness and utility of the invariant EKF for indirect wind estimation as this method can be applied to *any* fixed-wing UAV without requiring knowledge of the aerodynamic force and measurement models. It is important to note that the estimated wind velocity here is the *mean* wind velocity and the rotational components of the wind velocity are neglected. Additional work will be required to relax the assumptions made on the wind field described in Section 4 and the problem described here may need to be reformulated to capture additional wind velocity components, such as turbulent and rotational components.

Chapter 7

Conclusions

This dissertation presents the invariant EKF as an estimation algorithm that can be used to indirectly infer wind velocity using a small, fixed-wing UAV. An introduction to rigid body mechanics, geometric mechanics, and classical invariant theory are provided as foundational material for the design and implementation of the invariant EKF to estimate the extended state of the rigid aircraft in wind. An extensive literature review gives background on indirect wind estimation methods, categorized as either model-based or model-free methods, is presented. An overview of aircraft equations in wind, assumptions on the wind field, and common estimators are also described.

The main result of this work is the design and implementation of the invariant EKF for aerodynamic model-free indirect wind estimation using a small, fixed-wing UAV. This first requires proving that the dynamics and measurement of the system are invariant and equivariant, respectively, with respect to the action of a Lie group. An initial implementation of the invariant EKF on a UAV horizontal-plane flight shows that the 3DOF fixed-wing aircraft motion model is $G-$invariant under the left action of $SE(2)$ and that the output is $G-$equivariant. The formulation assumes that the specific force and specific moment acting on the aircraft due to aerodynamic effects are known inputs to the system. The invariant dynamics and equivariant output were then used to design the invariant EKF to estimate the position, orientation, velocity, and angular rate of the UAV as well as the wind velocity. A conventional EKF was also implemented to obtain wind velocity estimates.

The aircraft was simulated in both 1D and 2D von Kármán turbulence at a constant altitude cruise, and subject to a 40° yaw doublet in the first case. Results show that the invariant EKF outperforms the EKF in providing accurate wind velocity estimates. The measurement noise was varied to observe the sensitivity of the invariant EKF to measurement noise, and it was shown that while the invariant EKF estimates degraded they did not diverge. The invariant EKF, in general, has convergence guarantees over a larger subset of the state space when compared to the EKF as the state and output matrices are constant for a larger set of trajectories.

The invariant EKF was also designed for wind estimation using the full 6DOF rigid aircraft motion. It was proven that the dynamics of the UAV are invariant under the left action of the Lie group $G = SE(3)$ and that the chosen output is G-equivariant. The design of the invariant EKF was described in five steps: determining the normalization equations, building an invariant output error and a set of scalar invariants, building an invariant frame, defining an invariant state estimate error and determining the corresponding error dynamics, and designing the invariant EKF by linearizing the invariant state estimate error dynamics and the invariant output error about zero state error. The invariant EKF has local convergence guarantees along permanent trajectories, such as wings-level flight at constant altitude. Moreover, the Jacobian matrices defining the linearization within the invariant EKF remain relatively constant in a larger region of state space around this permanent trajectory. Simulated flight data were generated for nominal motions of a small, fixed-wing UAV corresponding to wings-level flight at constant altitude and flight along a vertically helical path with constant pitch and radius. In both cases, the nominal motion was disturbed by 1D von Kármán wind turbulence. For the wings-level flight example, the motion was further disturbed by a large pitch doublet. Wind estimates obtained using the invariant EKF were more accurate than those obtained using a conventional EKF. Qualitatively, time

histories of true and estimated wind velocity clearly show better tracking by the invariant EKF. Quantitatively, the invariant EKF wind estimates have lower RMS error compared with the EKF wind estimates. The RMS error of the invariant EKF estimates in wings level flight is at or below 1 m/s for all three wind velocity components whereas the EKF wind velocity estimates' RMS error approaches 1.1 m/s in the North direction and 1.15 m/s in the down direction. For the non-accelerated helical turn, the maximum invariant EKF RMS error is approximately 1.2 m/s in the east direction, and the maximum EKF RMS error of the wind velocity estimates is approximately 1.45 m/s. For both simulated flights, the EKF wind velocity estimate RMS error is higher than the invariant EKF wind velocity estimate RMS error.

The most notable contribution of this work was the application of the invariant EKF for wind estimation on experimental flight data. The problem was reformulated for the 6DOF case where the rotational dynamics of the aircraft were not considered. The modified kinematics and dynamics were shown to be $SE(3)$-invariant and the measurements available from the onboard sensor suite were shown to be $SE(3)$-equivariant. The invariant EKF was applied to two sets of flight data: a straight and level flight and a coordinated turn. The invariant EKF provided accurate wind estimates compared to the true (or reconstructed) wind velocity measurement by the aircraft in both flight conditions whereas estimates obtained from a conventional EKF diverged when applied to the coordinated turn flight data. The motivation of this work was to answer the question: Is aerodynamic model-free wind estimation possible using the invariant EKF where only measurements from the operational sensor suite of a fixed-wing UAV are available? It is demonstrated that aerodynamic model-free indirect wind estimation can be achieved using the invariant EKF on both simulated and experimental flight data using a full 6DOF rigid aircraft. There is a clear advantage in using the invariant EKF over common estimators, namely the EKF that was also implemented, as the estimator

does not diverge when the aircraft transitions from straight and level flight to executing a coordinated turn.

A limitation of the invariant EKF when applied to experimental flight data for indirect wind estimation is that the formulation is specific to fixed-wing aircraft that have airspeed measurements available. A valuable extension of the application of the invariant EKF to indirect wind estimation using UAVs would be to include a formulation for multirotor aircraft. Additionally, the application of the invariant EKF to experimental flight data required that the rotational dynamics of the aircraft be ignored and that the body angular rates be taken as inputs to the dynamic system. An improvement in indirect wind estimation results on experimental flight data may be achieved if the body angular rates are considered as part of the state of the aircraft and if measurements of the specific moment are available. Further work in the theory of symmetry-preserving observers may be to consider systems with reduced symmetry and design a framework such that the (reduced) symmetries of such a system can be exploited to design a state estimator.

Bibliography

[1] Greenwood, W. W., Lynch, J. P., and Zekkos, D., "Applications of UAVs in civil infrastructure," *Journal of Infrastructure Systems*, Vol. 25, No. 2, 2019, p. 04019002. doi:10.1061/(ASCE)IS.1943-555X.0000464.

[2] Savva, A., Zacharia, A., Makrigiorgis, R., Anastasiou, A., Kyrkou, C., Kolios, P., Panayiotou, C., and Theocharides, T., "ICARUS: Automatic autonomous power infrastructure inspection with UAVs," *International Conference on Unmanned Aircraft Systems (ICUAS)*, 2021. doi:10.1109/ICUAS51884.2021.9476742.

[3] Radoglou-Grammatikis, P., Sarigiannidis, P., Lagkas, T., and Moscholios, I., "A compilation of UAV applications for precision agriculture," *Computer Networks*, Vol. 172, 2020, p. 107148. doi:https://doi.org/10.1016/j.comnet.2020.107148.

[4] Poikonen, S., and Campbell, J. F., "Future directions in drone routing research," *Networks*, Vol. 77, No. 1, 2021, pp. 116–126.

[5] Nex, F., and Remondino, F., "UAV for 3D mapping applications: a review," *Applied Geomatics*, Vol. 6, No. 1, 2014, pp. 1–15. doi:10.1007/s12518-013-0120-x.

[6] Barbieri, L., Kral, S. T., Bailey, S. C., Frazier, A. E., Jacob, J. D., Reuder, J., Brus, D., Chilson, P. B., Crick, C., Detweiler, C., Doddi, A., Elston, J., Foroutan, H., González-Rocha, J., Greene, B. R., Guzman, M. I., Houston, A. L., Islam, A., Kemppinen, O., Lawrence, D., Pillar-Little, E. A., Ross, S. D., Sama, M. P., Schmale, D. G., Schuyler, T. J., Shankar, A., Smith, S. W., Waugh, S., Dixon, C., Borenstein, S., and Boer, G. D., "Intercomparison of small unmanned aircraft system (sUAS) measurements

for atmospheric science during the LAPSE-RATE campaign," *Sensors (Switzerland)*, Vol. 19, No. 9, 2019. doi:10.3390/s19092179.

[7] Jensen, A. A., Pinto, J. O., Bailey, S. C., Sobash, R. A., Boer, G. D., Houston, A. L., Chilson, P. B., Bell, T., Romine, G., Smith, S. W., Lawrence, D. A., Dixon, C., Lundquist, J. K., Jacob, J. D., Elston, J., Wwaugh, S., and Steiner, M., "Assimilation of a coordinated fleet of uncrewed aircraft system observations in complex terrain: EnKF system design and preliminary assessment," *Monthly Weather Review*, Vol. 149, No. 5, 2021, pp. 1459–1480. doi:10.1175/MWR-D-20-0359.1.

[8] Nolan, P. J., Pinto, J., González-Rocha, J., Jensen, A., Vezzi, C. N., Bailey, S. C., de Boer, G., Diehl, C., Laurence, R., Powers, C. W., Foroutan, H., Ross, S. D., and Schmale, D. G., "Coordinated unmanned aircraft system (UAS) and ground-based weather measurements to predict Lagrangian coherent structures (LCSs)," *Sensors (Switzerland)*, Vol. 18, No. 12, 2018. doi:10.3390/s18124448.

[9] Pillar-Little, E. A., Greene, B. R., Lappin, F. M., Bell, T. M., Segales, A. R., Azevedo, G. B. H. D., Doyle, W., Kanneganti, S. T., Tripp, D. D., and Chilson, P. B., "Observations of the thermodynamic and kinematic state of the atmospheric boundary layer over the San Luis Valley, CO, using the CopterSonde 2 remotely piloted aircraft system in support of the LAPSE-RATE field campaign," *Earth System Science Data*, Vol. 13, No. 2, 2021, pp. 269–280. doi:10.5194/essd-13-269-2021.

[10] Segales, A. R., Greene, B. R., Bell, T. M., Doyle, W., Martin, J. J., Pillar-Little, E. A., and Chilson, P. B., "The CopterSonde: An insight into the development of a smart unmanned aircraft system for atmospheric boundary layer research," *Atmospheric Measurement Techniques*, Vol. 13, No. 5, 2020, pp. 2833–2848. doi:10.5194/amt-13-2833-2020.

[11] De Wekker, S. F. J., Kossmann, M., Knievel, J. C., Giovannini, L., Gutmann, E. D., and Zardi, D., "Meteorological applications benefiting from an improved understanding of atmospheric exchange processes over mountains," *Atmosphere*, Vol. 9, No. 10, 2018. doi:10.3390/atmos9100371.

[12] Kumar, A., and Ben-Tzvi, P., "Estimation of wind conditions utilizing RC helicopter dynamics," *IEEE/ASME Transactions on Mechatronics*, Vol. 24, No. 5, 2019, pp. 2293–2303. doi:10.1109/TMECH.2019.2937844.

[13] Torgesen, A. J., How, J. P., and Cameron, B., "Airborne sensing for ship air wake surveys with a tethered autonomous UAV," *AIAA Scitech 2021 Forum*, AIAA, 2021. doi:10.2514/6.2021-0381.

[14] Phelps, D., Gamagedara, K., Waldron, J., Patil, K., and Snyder, M., "Ship air wake detection using a small fixed wing unmanned aerial vehicle," *AIAA Aerospace Sciences Meeting, 2018*, AIAA, 2018. doi:10.2514/6.2018-0784.

[15] Benders, S., Wenz, A., and Johansen, T. A., "Adaptive path planning for unmanned aircraft using in-flight wind velocity estimation," *Proceedings of the 2018 International Conference on Unmanned Aircraft Systems*, IEEE, 2018. doi:10.1109/ICUAS.2018.8453341.

[16] "NASA Aeronautics Strategic Implementation Plan," *Aeronautics Research Mission Directorate*, 2019. URL https://www.nasa.gov/sites/default/files/atoms/files/armd-strategic-implementation-plan.pdf.

[17] Wilson, T. C., Brenner, J., Morrison, Z., Jacob, J. D., and Elbing, B. R., "Wind speed statistics from a small UAS and its sensitivity to sensor location," *Atmosphere*, Vol. 13, No. 3, 2022. doi:10.3390/atmos13030443.

[18] Greenwood, D. T., *Advanced Dynamics*, Cambridge University Press, 2003.

[19] Hand, L. N., and Finch, J. D., *Analytical Mechanics*, Cambridge University Press, 1998.

[20] Holm, D., Schmah, T., and Stoica, C., *Geometric Mechanics and Symmetry: From Finite to Infinite Dimensions*, Oxford Texts in Applied and Engineering Mathematics, OUP Oxford, 2009. URL https://books.google.com/books?id=H9qHi9UgYvsC.

[21] Marsden, J., and Ratiu, T., *Introduction to Mechanics and Symmetry: A Basic Exposition of Classical Mechanical Systems*, Texts in Applied Mathematics, Springer-Verlag New York, 2013.

[22] Bullo, F., and Lewis, A., *Geometric Control of Mechanical Systems: Modeling, Analysis, and Design for Simple Mechanical Control Systems*, Texts in Applied Mathematics, Springer New York, 2004. URL https://books.google.com/books?id=jg7VumxOoe4C.

[23] Olver, P. J., *Classical Invariant Theory*, Cambridge University Press, 1999.

[24] Murray, R. M., Li, Z., and Sastry, S. S., *A Mathematical Introduction to Robotic Manipulation*, CRC Press, 1994.

[25] Boothby, W. M., *An Introduction to Differentiable Manifolds and Riemannian Geometry*, Academic Press, 1986.

[26] Bonnabel, S., Martin, P., and Rouchon, P., "Symmetry-Preserving Observers," *IEEE Transactions on Automatic Control*, Vol. 53, No. 11, 2008, pp. 2514–2526. doi:10.1109/TAC.2008.2006929.

[27] Ahmed, Z., Halefom, M. H., and Woolsey, C. A., "A Tutorial Overview of Indirect Wind Estimation Using Small Uncrewed Air Vehicles," *Journal of Aerospace Information Systems*, 2024. (To appear).

[28] Gahan, K., Hopwood, J. W., and Woolsey, C. A., "Wind estimation using an H∞ filter with fixed-wing aircraft flight test results," *AIAA SCITECH 2023 Forum*, 2023. doi:10.2514/6.2023-2252.

[29] Abichandani, P., Lobo, D., Ford, G., Bucci, D., and Kam, M., "Wind measurement and simulation techniques in multi-rotor small unmanned aerial vehicles," *IEEE Access*, 2020. doi:10.1109/ACCESS.2020.2977693.

[30] Wenz, A., and Johansen, T. A., "Moving horizon estimation of air data parameters for UAVs," *IEEE Transactions on Aerospace and Electronic Systems*, Vol. 56, No. 3, 2020, pp. 2101–2121. doi:10.1109/TAES.2019.2946677.

[31] Kaimal, J. C., Wyngaard, J. C., Izumi, Y., and Coté, O. R., "Spectral characteristics of surface-layer turbulence," *Quarterly Journal of the Royal Meteorological Society*, Vol. 98, No. 417, 1972, pp. 563–589. doi:https://doi.org/10.1002/qj.49709841707.

[32] Mann, J., "The spatial structure of neutral atmospheric surface-layer turbulence," *Journal of Fluid Mechanics*, Vol. 273, 1994, p. 141–168. doi:10.1017/S0022112094001886.

[33] Berg, J., Natarajan, A., Mann, J., and Patton, E. G., "Gaussian vs non-Gaussian turbulence: impact on wind turbine loads," *Wind Energy*, Vol. 19, No. 11, 2016, pp. 1975–1989. doi:https://doi.org/10.1002/we.1963.

[34] Hattenberger, G., Bronz, M., and Condomines, J. P., "Estimating wind us-

ing a quadrotor," *International Journal of Micro Air Vehicles*, Vol. 14, 2022. doi:10.1177/17568293211070824.

[35] Langelaan, J. W., Spletzer, J., Montella, C., and Grenestedt, J., "Wind field estimation for autonomous dynamic soaring," *Proceedings of the IEEE International Conference on Robotics and Automation*, IEEE, 2012. doi:10.1109/ICRA.2012.6224954.

[36] Xiang, X., Wang, Z., Mo, Z., Chen, G., Pham, K., and Blasch, E., "Wind field estimation through autonomous quadcopter avionics," *AIAA/IEEE Digital Avionics Systems Conference - Proceedings*, Vol. 2016-December, IEEE, 2016. doi:10.1109/DASC.2016.7778071.

[37] Petrich, J., and Subbarao, K., "On-board wind speed estimation for UAVs," *AIAA Guidance, Navigation, and Control Conference*, AIAA, 2011. doi:10.2514/6.2011-6223.

[38] Balmer, G., Muskardin, T., Wlach, S., and Kondak, K., "Enhancing model-free wind estimation for fixed-wing UAV," *2018 International Conference on Unmanned Aircraft Systems*, IEEE, 2018. doi:10.1109/ICUAS.2018.8453419.

[39] Chen, H., Bai, H., and Taylor, C. N., "Invariant-EKF design for quadcopter wind estimation," *Proceedings of the 2022 American Control Conference (ACC)*, IEEE, 2022. doi:10.23919/ACC53348.2022.9867417.

[40] Lie, F. A. P., and Gebre-Egziabher, D., "Synthetic air data system," *Journal of Aircraft*, Vol. 50, No. 4, 2013, pp. 1234–1249. doi:10.2514/1.C032177.

[41] Pappu, V. S. R., Liu, Y., Horn, J. F., and Cooper, J., "Wind gust estimation on a small VTOL UAV," *7th AHS Technical Meeting on VTOL Unmanned Aircraft Systems and Autonomy*, American Helicopter Society, Mesa, AZ, USA, 2017.

[42] Sun, J., Li, B., Wen, C. Y., and Chen, C. K., "Model-aided wind estimation method for a tail-sitter aircraft," *IEEE Transactions on Aerospace and Electronic Systems*, Vol. 56, No. 2, 2020, pp. 1262–1278. doi:10.1109/TAES.2019.2929379.

[43] Tian, P., and Chao, H., "Model aided estimation of angle of attack, sideslip angle, and 3D wind without flow angle measurements," *AIAA Guidance, Navigation, and Control Conference*, American Institute of Aeronautics and Astronautics Inc, AIAA, 2018. doi:10.2514/6.2018-1844.

[44] Cho, A. M., Kim, J., Lee, S., and Kee, C., "Wind estimation and airspeed calibration using a UAV with a single-antenna GPS receiver and pitot tube," *IEEE Transactions on Aerospace and Electronic Systems*, Vol. 47, No. 1, 2011. doi:10.1109/TAES.2011.5705663.

[45] Rautenberg, A., Graf, M. S., Wildmann, N., Platis, A., and Bange, J., "Reviewing wind measurement approaches for fixed-wing unmanned aircraft," *Atmosphere*, Vol. 9, No. 11, 2018. doi:10.3390/atmos9110422.

[46] Zhang, Q., Xu, Y., Wang, X., Yu, Z., and Deng, T., "Real-time wind field estimation and pitot tube calibration using an extended kalman filter," *Mathematics*, Vol. 9, No. 6, 2021. doi:10.3390/math9060646.

[47] Wenz, A., Johansen, T. A., and Cristofaro, A., "Combining model-free and model-based angle of attack estimation for small fixed-wing UAVs using a standard sensor suite," *Proceedings of the 2016 International Conference on Unmanned Aircraft Systems*, IEEE, 2016. doi:10.1109/ICUAS.2016.7502583.

[48] Condomines, J.-P., Bronz, M., Hattenberger, G., and Erdelyi, J.-F., "Experimental wind field estimation and aircraft identification," *IMAV 2015: International Micro Air Vehicles Conference and Flight Competition*, 2015.

[49] Cooper, J., Hopwood, J., Woolsey, C., Wekker, S. D., and DeVore, M., "Intelligent wind estimation for chemical source localization," *VFS International 79th Annual Forum and Technology Display*, Vertical Flight Society, 2023.

[50] Larrabee, T., Chao, H., Rhudy, M., Gu, Y., and Napolitano, M. R., "Wind field estimation in UAV formation flight," *Proceedings of the American Control Conference*, IEEE, 2014. doi:10.1109/ACC.2014.6859266.

[51] Lee, J. H., Sevil, H. E., Dogan, A., and Hullender, D., "Estimation of maneuvering aircraft states and time-varying wind with turbulence," *Aerospace Science and Technology*, Vol. 31, No. 1, 2013, pp. 87–98. doi:10.1016/j.ast.2013.09.009.

[52] Rhudy, M. B., Gu, Y., and Chao, H., "Wind field velocity and acceleration estimation using a small UAV," *Proceedings of the AIAA Modeling and Simulation Technologies Conference*, AIAA, 2014. doi:10.2514/6.2014-2647.

[53] Rhudy, M., Gross, J., and Gu, Y., "Stochastic wind modeling and estimation for unmanned aircraft systems," *AIAA Aviation 2019 Forum*, AIAA, 2019. doi:10.2514/6.2019-3111.

[54] Rhudy, M. B., Gu, Y., Gross, J. N., and Chao, H., "Onboard wind velocity estimation comparison for unmanned aircraft systems," *IEEE Transactions on Aerospace and Electronic Systems*, Vol. 53, No. 1, 2017, pp. 55–66. doi:10.1109/TAES.2017.2649218.

[55] Asignacion, A., Suzuki, S., Noda, R., Nakata, T., and Liu, H., "Frequency-based wind gust estimation for quadrotors using a nonlinear disturbance observer," *IEEE Robotics and Automation Letters*, Vol. 7, No. 4, 2022, pp. 9224–9231. doi:10.1109/LRA.2022.3190073.

[56] González-Rocha, J., Wekker, S. F. D., Ross, S. D., and Woolsey, C. A., "Wind profiling

in the lower atmosphere from wind-induced perturbations to multirotor UAS," *Sensors (Switzerland)*, Vol. 20, No. 5, 2020. doi:10.3390/s20051341.

[57] González-Rocha, J., Woolsey, C. A., Sultan, C., Rose, N., and Wekker, S. F. D., "Measuring atmospheric winds from quadrotor motion," *AIAA Atmospheric Flight Mechanics Conference*, AIAA, 2017. doi:10.2514/6.2017-1189.

[58] González-Rocha, J., Woolsey, C. A., Sultan, C., and Wekker, S. F. D., "Sensing wind from quadrotor motion," *Journal of Guidance, Control, and Dynamics*, Vol. 42, No. 4, 2019, pp. 836–852. doi:10.2514/1.G003542.

[59] Borup, K. T., Fossen, T. I., and Johansen, T. A., "A nonlinear model-based wind velocity observer for unmanned aerial vehicles," *IFAC-PapersOnLine*, Vol. 49, Elsevier B.V., 2016. doi:10.1016/j.ifacol.2016.10.177.

[60] Azid, S. I., Kumar, K., Cirrincione, M., and Fagiolini, A., "Wind gust estimation for precise quasi-hovering control of quadrotor aircraft," *Control Engineering Practice*, Vol. 116, 2021. doi:10.1016/j.conengprac.2021.104930.

[61] Hong, H., Wang, M., Holzapfel, F., and Tang, S., "Wind estimation for fixed-wing aircraft using command tracking approach," *MED 2018 - 26th Mediterranean Conference on Control and Automation*, Institute of Electrical and Electronics Engineers Inc., 2018. doi:10.1109/MED.2018.8443055.

[62] Langelaan, J. W., Alley, N., and Neidhoefer, J., "Wind field estimation for small unmanned aerial vehicles," *Journal of Guidance, Control, and Dynamics*, Vol. 34, No. 4, 2011, pp. 1016–1030. doi:10.2514/1.52532.

[63] Marinescu, M., Olivares, A., Staffetti, E., and Sun, J., "On the estimation of vector

wind profiles using aircraft-derived data and Gaussian process regression," *Aerospace*, Vol. 9, No. 7, 2022. doi:10.3390/aerospace9070377.

[64] Meier, K., Hann, R., Skaloud, J., and Garreau, A., "Wind estimation with multirotor UAVs," *Atmosphere*, Vol. 13, No. 4, 2022. doi:10.3390/atmos13040551.

[65] Neumann, P. P., and Bartholmai, M., "Real-time wind estimation on a micro unmanned aerial vehicle using its inertial measurement unit," *Sensors and Actuators, A: Physical*, Vol. 235, 2015, pp. 300–310. doi:10.1016/j.sna.2015.09.036.

[66] Palomaki, R. T., Rose, N. T., van den Bossche, M., Sherman, T. J., and Wekker, S. F. D., "Wind estimation in the lower atmosphere using multirotor aircraft," *Journal of Atmospheric and Oceanic Technology*, Vol. 34, No. 5, 2017, pp. 1183–1191. doi:10.1175/JTECH-D-16-0177.1.

[67] Perozzi, G., Efimov, D., Biannic, J. M., and Planckaert, L., "Using a quadrotor as wind sensor: time-varying parameter estimation algorithms," *International Journal of Control*, Vol. 95, No. 1, 2022, pp. 126–137. doi:10.1080/00207179.2020.1780324.

[68] Salazar, L. R., Cobano, J. A., and Ollero, A., "Small UAS-based wind feature identification system Part 1: Integration and validation," *Sensors (Switzerland)*, Vol. 17, No. 1, 2017. doi:10.3390/s17010008.

[69] Shelekhov, A., Afanasiev, A., Shelekhova, E., Kobzev, A., Tel'minov, A., Molchunov, A., and Poplevina, O., "High-Resolution Profiling of Atmospheric Turbulence Using UAV Autopilot Data," *Drones*, Vol. 7, 2023, p. 412. doi:10.3390/drones7070412.

[70] Velasco-Carrau, J., García-Nieto, S., Salcedo, J. V., and Bishop, R. H., "Multi-objective optimization for wind estimation and aircraft model identification," *Jour-*

nal of Guidance, Control, and Dynamics, Vol. 39, No. 2, 2016, pp. 372–389. doi:10.2514/1.G001294.

[71] Witte, B. M., Singler, R. F., and Bailey, S. C., "Development of an unmanned aerial vehicle for the measurement of turbulence in the atmospheric boundary layer," *Atmosphere*, Vol. 8, No. 10, 2017. doi:10.3390/atmos8100195.

[72] Halefom, M. H., Gresham, J. L., and Woolsey, C. A., "Wind estimation from an unsteady aerodynamic fixed-wing motion model," *AIAA SciTech Forum 2022*, AIAA, 2022. doi:10.2514/6.2022-0554.

[73] Hong, H., Wang, M., Holzapfel, F., and Tang, S., "Fast real-time three-dimensional wind estimation for fixed-wing aircraft," *Aerospace Science and Technology*, Vol. 69, 2017, pp. 674–685. doi:10.1016/j.ast.2017.07.019.

[74] Leonard, N., and Krishnaprasad, P., "Motion control of drift-free, left-invariant systems on Lie groups," *IEEE Transactions on Automatic Control*, Vol. 40, No. 9, 1995, pp. 1539–1554. doi:10.1109/9.412625.

[75] Leonard, N., "Geometric methods for robust stabilization of autonomous underwater vehicles," *Proceedings of Symposium on Autonomous Underwater Vehicle Technology*, 1996. doi:10.1109/AUV.1996.532449.

[76] Aghannan, N., and Rouchon, P., "On invariant asymptotic observers," *Proceedings of the 41st IEEE Conference on Decision and Control, 2002.*, Vol. 2, 2002. doi:10.1109/CDC.2002.1184728.

[77] Aghannan, N., and Rouchon, P., "An intrinsic observer for a class of Lagrangian systems," *IEEE Transactions on Automatic Control*, Vol. 48, No. 6, 2003, pp. 936–945. doi:10.1109/TAC.2003.812778.

[78] Mahony, R., Trumpf, J., and Hamel, T., "Observers for Kinematic Systems with Symmetry," *IFAC Proceedings Volumes*, Vol. 46, No. 23, 2013, pp. 617–633. doi:https://doi.org/10.3182/20130904-3-FR-2041.00212, URL https://www.sciencedirect.com/science/article/pii/S1474667016317293, 9th IFAC Symposium on Nonlinear Control Systems.

[79] Barrau, A., and Bonnabel, S., "The invariant extended Kalman filter as a stable observer," *IEEE Transactions on Automatic Control*, Vol. 62, No. 4, 2017, pp. 1797–1812. doi:10.1109/TAC.2016.2594085.

[80] Barrau, A., and Bonnabel, S., "Invariant Kalman filtering," *Annual Review of Control, Robotics, and Autonomous Systems*, Vol. 1, No. 1, 2018, pp. 237–257. doi:10.1146/annurev-control-060117-105010.

[81] Bonnabel, S., "Left-invariant extended Kalman filter and attitude estimation," *2007 46th IEEE Conference on Decision and Control*, 2007. doi:10.1109/CDC.2007.4434662.

[82] Bonnabel, S., Martin, P., and Salaün, E., "Invariant Extended Kalman Filter: Theory and Application to a Velocity-aided Attitude Estimation Problem," *Proceedings of the 48h IEEE Conference on Decision and Control (CDC) held jointly with 2009 28th Chinese Control Conference*, 2009. doi:10.1109/CDC.2009.5400372.

[83] Potokar, E. R., Norman, K., and Mangelson, J. G., "Invariant extended Kalman filtering for underwater navigation," *IEEE Robotics and Automation Letters*, Vol. 6, No. 3, 2021, pp. 5792–5799. doi:10.1109/LRA.2021.3085167.

[84] Coleman, K., Bai, H., and Taylor, C. N., "Extended Invariant-EKF Designs for State and Additive Disturbance Estimation," *Automatica*, Vol. 125, 2021, p. 109464. doi:https://doi.org/10.1016/j.automatica.2020.109464.

[85] Condomines, J.-P., Seren, C., and Hattenberger, G., "Nonlinear state estimation using an invariant unscented Kalman filter," *AIAA Guidance, Navigation, and Control (GNC) Conference*, 2013. doi:10.2514/6.2013-4869.

[86] Condomines, J.-P., Seren, C., and Hattenberger, G., "Pi-invariant unscented Kalman filter for sensor fusion," *53rd IEEE Conference on Decision and Control*, 2014. doi:10.1109/CDC.2014.7039518.

[87] Condomines, J.-P., Seren, C., and Hattenberger, G., "Invariant unscented Kalman filter with application to attitude estimation," *2017 IEEE 56th Annual Conference on Decision and Control (CDC)*, 2017. doi:10.1109/CDC.2017.8264063.

[88] Chen, H., and Bai, H., "Incorporating Thrust Models for Quadcopter Wind Estimation," *IFAC-PapersOnLine*, Vol. 55, No. 37, 2022, pp. 19–24. doi:https://doi.org/10.1016/j.ifacol.2022.11.155, 2nd Modeling, Estimation and Control Conference MECC 2022.

[89] Etkin, B., *Dynamics of Atmospheric Flight*, Dover Books on Aeronautical Engineering, Dover Publications, 2005.

[90] Kaimal, J. C., and Finnigan, J. J., *Atmospheric Boundary Layer Flows: Their Structure and Measurement*, Oxford University Press, 1994. doi:10.1093/oso/9780195062397.001.0001.

[91] Arnold, L., *Stochastic Differential Equations: Theory and Application*, Vol. 1, John Wiley & Sons, New York, 1974.

[92] Luenberger, D., "An introduction to observers," *IEEE Transactions on Automatic Control*, Vol. 16, No. 6, 1971, pp. 596–602. doi:10.1109/TAC.1971.1099826.

[93] Brogan, W. L., *Modern Control Theory*, 3rd ed., Prentice-Hall, Englewood Cliffs, NJ, 1991.

[94] Rugh, W. J., *Linear System Theory*, 2nd ed., Prentice-Hall, Upper Saddle River, N.J., 1996.

[95] Bar-Shalom, Y., Rong Li, X., and Kirubarajan, T., *Estimation with Applications to Tracking and Navigation*, John Wiley & Sons, 2002. doi:https://doi.org/10.1002/0471221279.

[96] Julier, S. J., and Uhlmann, J. K., "New extension of the Kalman filter to nonlinear systems," *Signal Processing, Sensor Fusion, and Target Recognition VI*, Vol. 3068, edited by I. Kadar, International Society for Optics and Photonics, SPIE, 1997. doi:10.1117/12.280797.

[97] Wan, E., and Van Der Merwe, R., "The unscented Kalman filter for nonlinear estimation," *Proceedings of the IEEE 2000 Adaptive Systems for Signal Processing, Communications, and Control Symposium (Cat. No.00EX373)*, 2000. doi:10.1109/ASSPCC.2000.882463.

[98] Gresham, J. L., Simmons, B. M., Fahmi, J.-M. W., and Woolsey, C. A., "Remote uncorrelated pilot inputs for nonlinear aerodynamic model identification from flight data," *AIAA Aviation 2021 Forum*, 2021. doi:10.2514/6.2021-2792.

[99] Bonnabel, S., Martin, P., and Rouchon, P., "Non-Linear symmetry-preserving observers on Lie groups," *IEEE Transactions on Automatic Control*, Vol. 54, No. 7, 2009, pp. 1709–1713. doi:10.1109/TAC.2009.2020646.

[100] Krener, A. J., "The convergence of the extended Kalman filter," *Directions in Math-*

ematical Systems Theory and Optimization, edited by A. Rantzer and C. I. Byrnes, Springer Berlin Heidelberg, Berlin, Heidelberg, 2003.

[101] Halefom, M. H., Hopwood, J. W., and Woolsey, C. A., "Unsteady Aerodynamics in Model-Based Wind Estimation from Fixed-Wing Aircraft Motion," *Journal of Guidance, Control, and Dynamics*, Vol. 0, No. 0, 2024, pp. 1–13. doi:10.2514/1.G007836.

Appendices

Appendix A

A.0.1 Example Aircraft Parameters

The small, fixed-wing aircraft model used in simulation was the MTD2 aircraft model identified by the Nonlinear Systems Laboratory (NSL) at Virginia Tech. The mass and geometric properties of the MTD2 are provided in Table A.1. An identified aerodynamic model of the

Table A.1: MTD2 aircraft mass and geometric properties.

Parameter	Symbol	Value
Mass	m	3.311 kg
Wing span	b	1.80 m
Moments of inertia	I_{xx}	$0.319\,\text{kg-m}^2$
	I_{yy}	$0.267\,\text{kg-m}^2$
	I_{zz}	$0.471\,\text{kg-m}^2$
	I_{xz}	$0.024\,\text{kg-m}^2$
Mean aerodynamic chord	c	0.254 m
Wing surface area	S	$0.457\,\text{m}^2$
Propeller diameter	D	0.254 m
Number of propellers	η_n	2
Propeller Efficiency	η_e	90%

aircraft was used to simulate its flight. The model was identified from flight data by other

members of the NSL. The models identified for the aerodynamic force and moment are

$$\boldsymbol{F}_{\mathrm{A}} = \frac{1}{2}\rho\|\boldsymbol{v}\|^2 S \begin{pmatrix} C_X(\boldsymbol{v},\boldsymbol{\omega},\boldsymbol{\delta}) \\ C_Y(\boldsymbol{v},\boldsymbol{\omega},\boldsymbol{\delta}) \\ C_Z(\boldsymbol{v},\boldsymbol{\omega},\boldsymbol{\delta}) \end{pmatrix} + D^4\rho\eta_e\eta_{\mathrm{n}}\delta_{\mathrm{rps}}^2 \begin{pmatrix} C_J(\boldsymbol{\delta}) \\ 0 \\ 0 \end{pmatrix} \tag{A.1}$$

$$\boldsymbol{M}_{\mathrm{A}} = \frac{1}{2}\rho\|\boldsymbol{v}\|^2 S \begin{pmatrix} bC_l(\boldsymbol{v},\boldsymbol{\omega},\boldsymbol{\delta}) \\ \bar{c}C_m(\boldsymbol{v},\boldsymbol{\omega},\boldsymbol{\delta}) \\ bC_n(\boldsymbol{v},\boldsymbol{\omega},\boldsymbol{\delta}) \end{pmatrix} \tag{A.2}$$

where $\boldsymbol{\delta} = [\delta_a, \delta_e, \delta_r, \delta_{\mathrm{rps}}]^{\mathrm{T}}$ are the control inputs corresponding to aileron, elevator, rudder, and thrust commands, $\bar{c}$ is the mean aerodynamic chord, b is the wingspan, S is the aircraft wing surface area, ρ is the air density, D is the diameter of the propeller, η_e is the propeller efficiency, and η_n is the number of propellers. The non-dimensional thrust, force, and moment models are

$$C_J = C_{J_0} + C_J J + C_{J^2} J^2 \tag{A.3a}$$

$$C_X = C_{X_0} + C_{X_{\delta_e}}\delta_e + C_{X_\alpha}\alpha + C_{X_\alpha^2}\alpha^2 \tag{A.3b}$$

$$C_Y = C_{Y_p}\hat{p} + C_{Y_{\mathrm{r}}}\hat{r} + C_{Y_{\delta_a}}\delta_a + C_{Y_{\delta_{\mathrm{r}}}}\delta_{\mathrm{r}} + C_{Y_\beta}\beta \tag{A.3c}$$

$$C_Z = C_{Z_0} + C_{Z_q}\hat{q} + C_{Z_\alpha}\alpha \tag{A.3d}$$

$$C_l = C_{l_p}\hat{p} + C_{l_{\delta_a}}\delta_a + C_{l_\beta}\beta \tag{A.3e}$$

$$C_m = C_{m_0} + C_{m_q}\hat{q} + C_{m_{\delta_e}}\delta_e + C_{m_\alpha}\alpha + C_{m_{\dot{\alpha}}}\dot{\alpha} \tag{A.3f}$$

$$C_n = C_{n_{\mathrm{r}}}\hat{r} + C_{n_{\delta_a}}\delta_a + C_{n_{\delta_{\mathrm{r}}}}\delta_{\mathrm{r}} + C_{n_\beta}\beta \tag{A.3g}$$

where the non-dimensional terms in Eqn. (A.3) are

$$\alpha = \tan^{-1}\left(\frac{w}{u}\right) \quad \beta = \sin^{-1}\left(\frac{v}{\|\boldsymbol{v}\|}\right) \quad \hat{p} = \frac{pb}{2\|\boldsymbol{v}\|} \quad \hat{q} = \frac{q\bar{c}}{2\|\boldsymbol{v}\|} \quad \hat{r} = \frac{rb}{2\|\boldsymbol{v}\|} \quad J = \frac{\|\boldsymbol{v}\|}{\delta_{\mathrm{rps}}D}$$

Table A.2 provides the identified force and moment coefficients.

Table A.2: Aerodynamic force and moment coefficients for the MTD2.

Coefficient	Value	Coefficient	Value	Coefficient	Value
C_{J_0}	-0.131	C_{Y_p}	0.221	C_{Z_0}	-0.225
C_J	-0.040	C_{Y_r}	0.230	C_{Z_q}	-12.54
C_{J^2}	0.116	$C_{Y_{\delta_a}}$	0.118	C_{Z_α}	-4.451
C_{X_0}	-0.428	$C_{Y_{\delta_r}}$	0.136		
$C_{X_{\delta_e}}$	0.051	C_{Y_β}	-0.525		
C_{X_α}	0.282				
$C_{X_{\alpha^2}}$	3.292				
Coefficient	Value	Coefficient	Value	Coefficient	Value
C_{l_p}	-0.386	C_{m_0}	0.008	C_{n_r}	-0.119
$C_{l_{\delta_a}}$	-0.137	C_{m_q}	-14.02	$C_{n_{\delta_a}}$	0.013
C_{l_β}	-0.039	$C_{m_{\delta_e}}$	-0.415	$C_{n_{\delta_r}}$	-0.068
		C_{m_α}	-0.471	C_{n_β}	0.103
		$C_{m_{\dot{\alpha}}}$	0.550		

A.0.2 Additional State Estimates (Simulation)

Estimates of the states $(X, Y, Z, \phi, \theta, \psi, u, v, w, p, q, r)$ are provided using both the invariant EKF and conventional EKF on the simulated flight data shown in Section 6.4. Figures A.1, A.2, and A.3 show results of estimation along the permanent trajectory corresponding to constant altitude, constantly linearly accelerated wings level flight. The estimates along the permanent trajectory of a non-accelerated helical turn are given in Fig. A.4, A.5, and A.6.

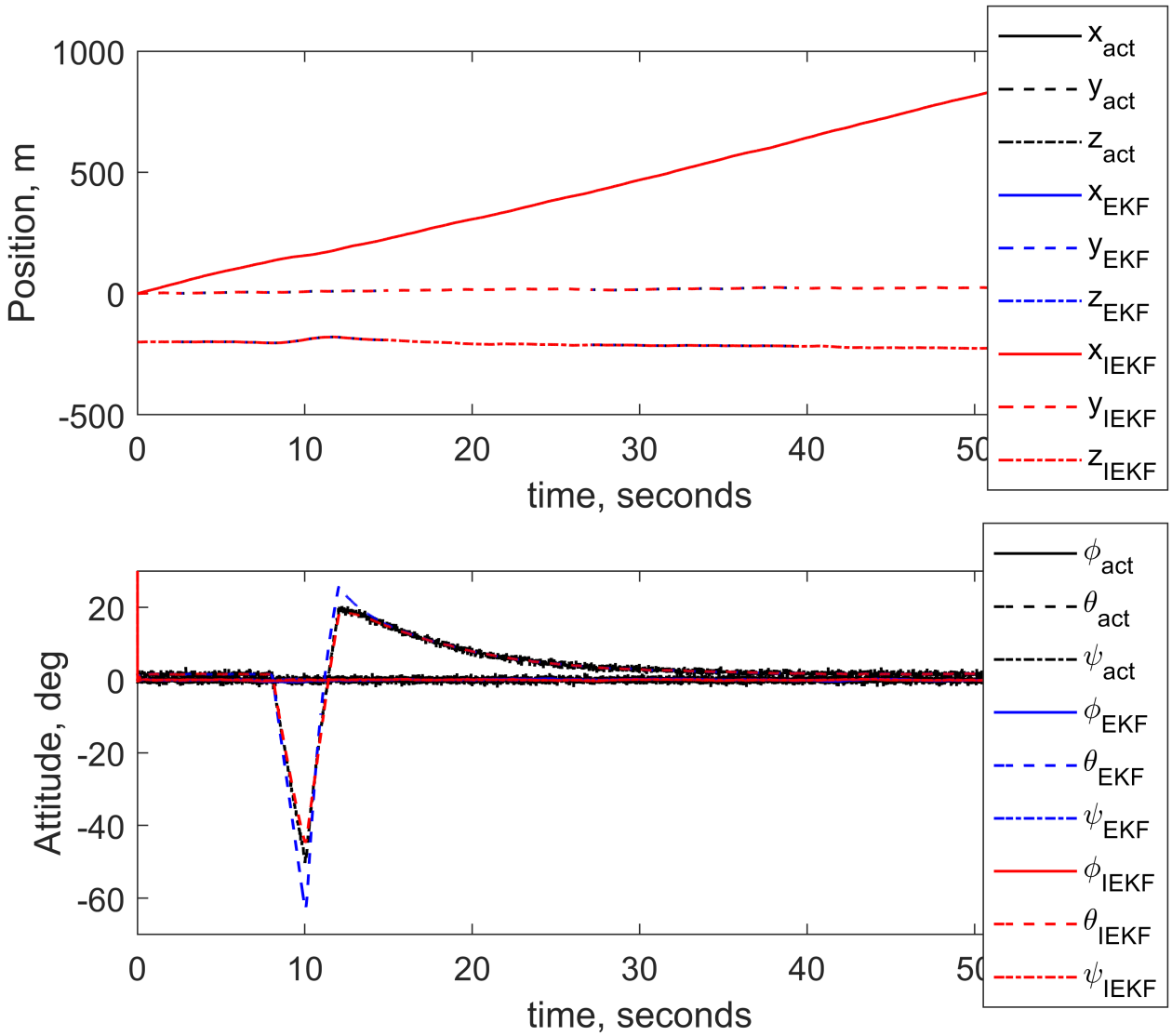

Figure A.1: Position and attitude estimates for the aircraft simulated along constant altitude, constantly linearly accelerated wings level flight with an applied perturbation of a 10 degree elevator doublet at $t = 8$ seconds using both the invariant EKF and conventional EKF.

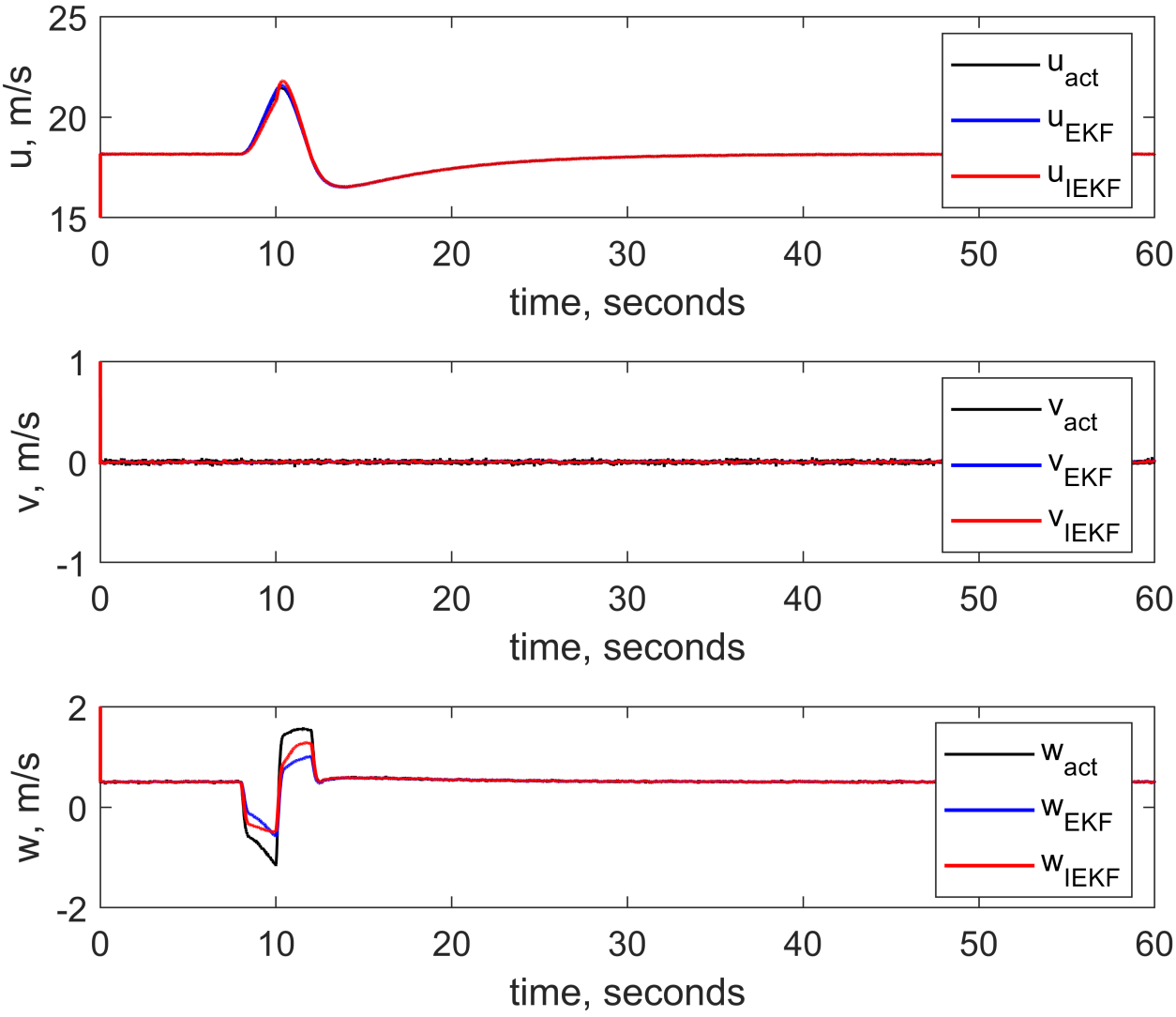

Figure A.2: Body velocity estimates for the aircraft simulated along constant altitude, constantly linearly accelerated wings level flight with an applied perturbation of a 10 degree elevator doublet at $t = 8$ seconds using both the invariant EKF and conventional EKF.

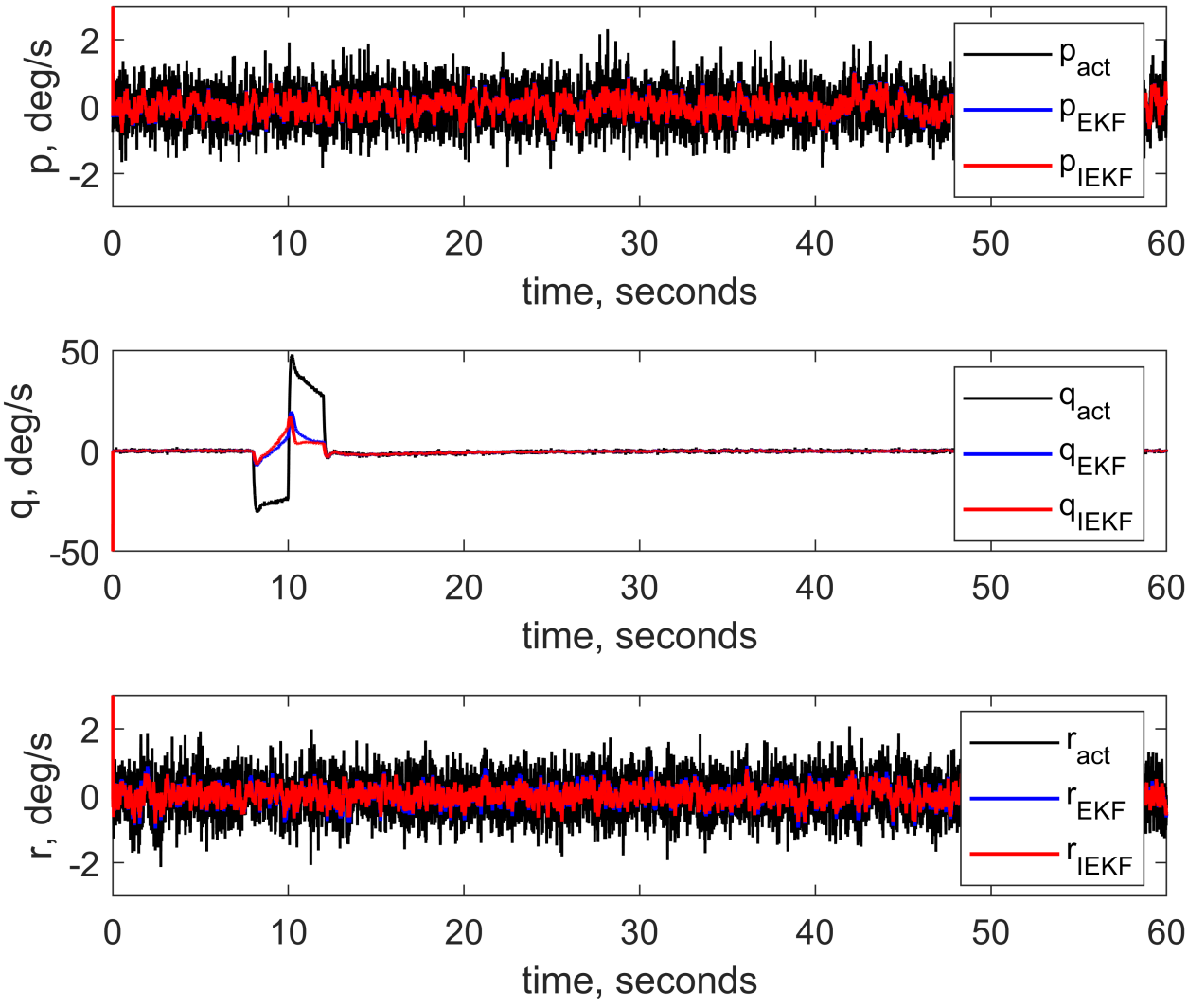

Figure A.3: Body angular rate estimates for the aircraft simulated along constant altitude, constantly linearly accelerated wings level flight with an applied perturbation of a 10 degree elevator doublet at $t = 8$ seconds using both the invariant EKF and conventional EKF.

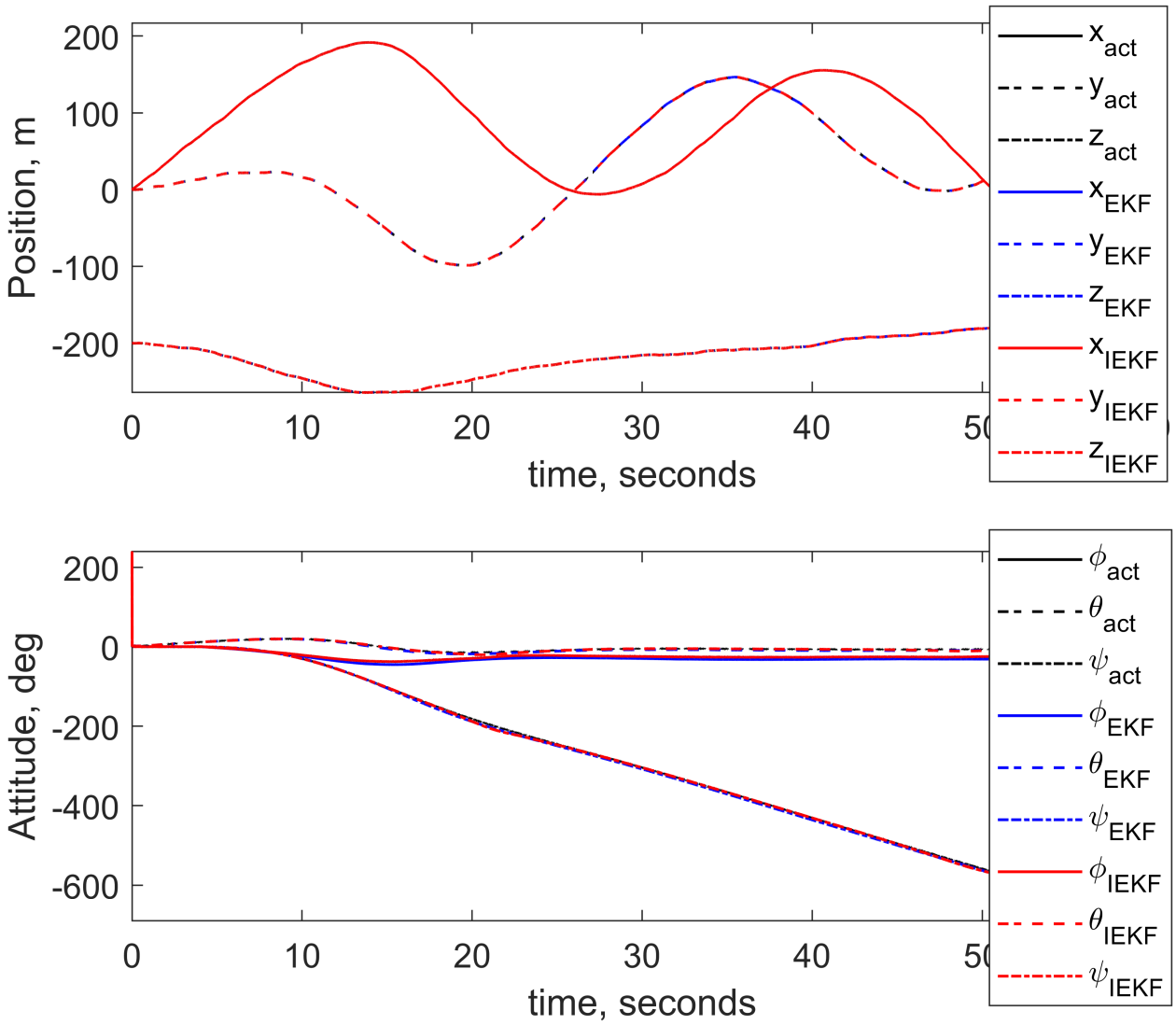

Figure A.4: Position and attitude estimates for the aircraft simulated along a non-accelerated helical turn using both the invariant EKF and conventional EKF.

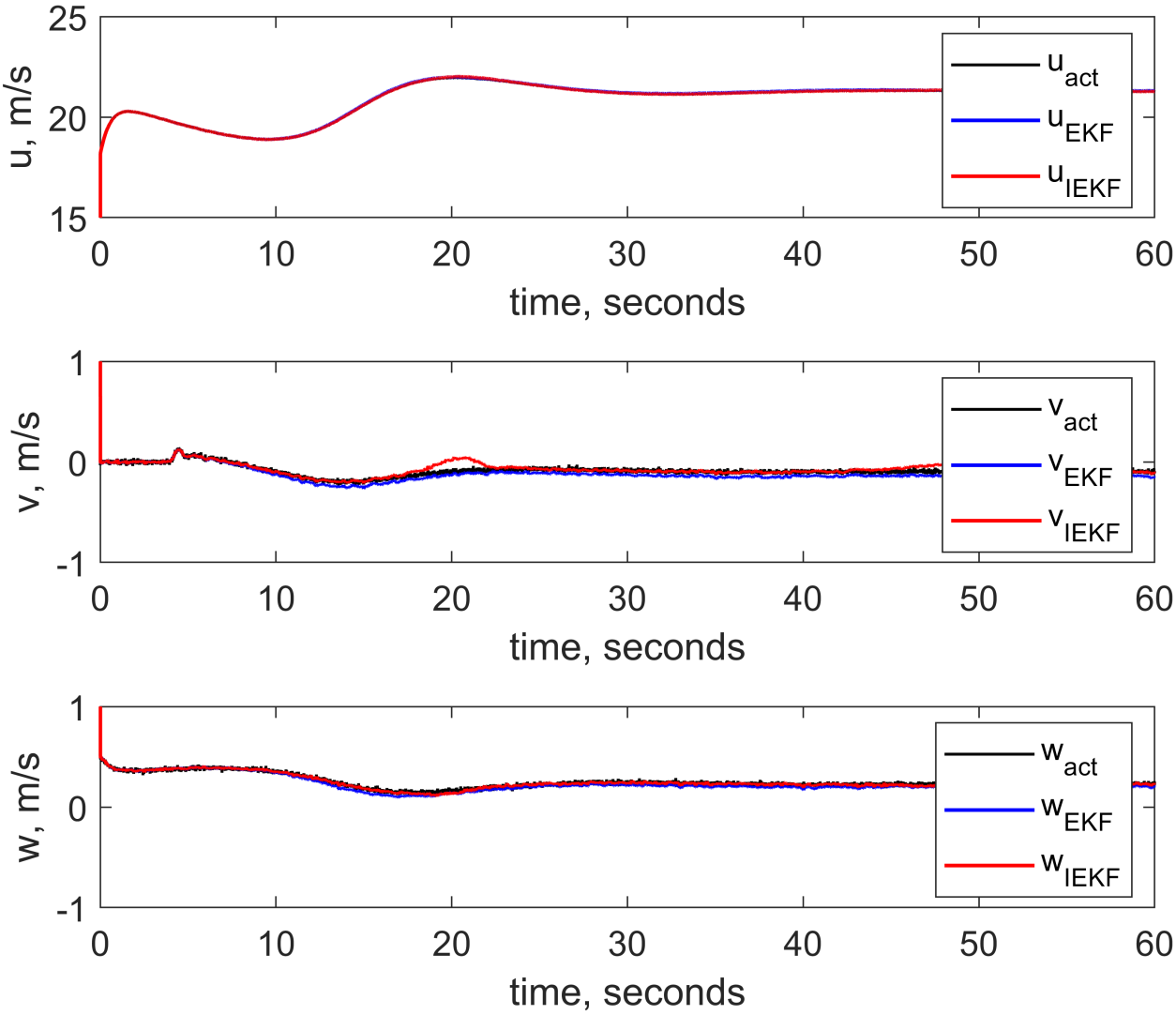

Figure A.5: Body velocity estimates for the aircraft simulated along a non-accelerated helical turn using both the invariant EKF and conventional EKF.

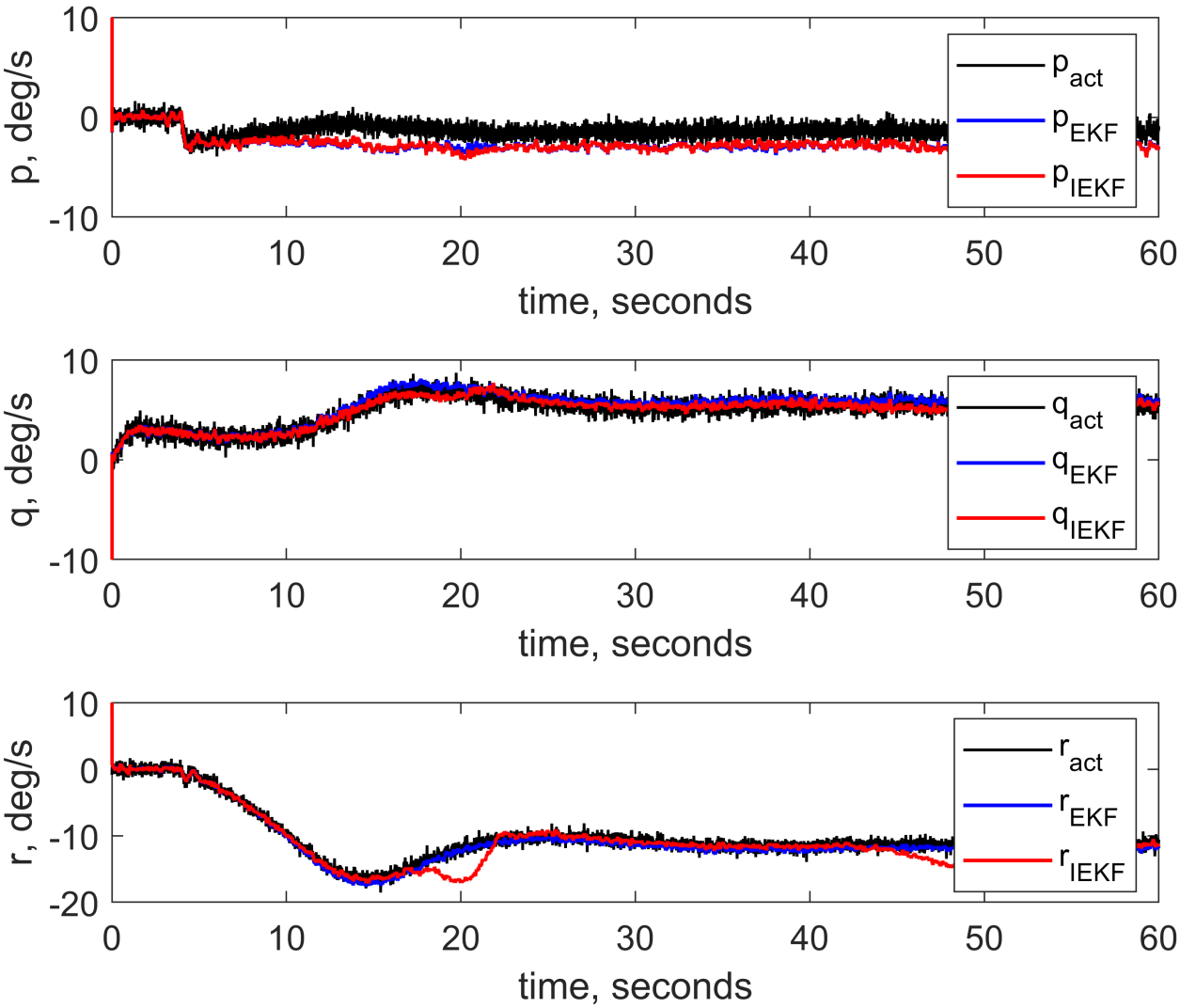

Figure A.6: Body angular rate estimates for the aircraft simulated along a non-accelerated helical turn using both the invariant EKF and conventional EKF.

A.0.3 Additional State Estimates (Experimental)

Estimates of the inertial position and inertial velocity of the UAV for the experimental flight data shown in Section 6.5 are provided. Figures A.7 and A.8 show the additional state estimates for the aircraft in straight and level flight. Figures A.9 and A.10 show the additional state estimates for the aircraft while executing a coordinated turn.

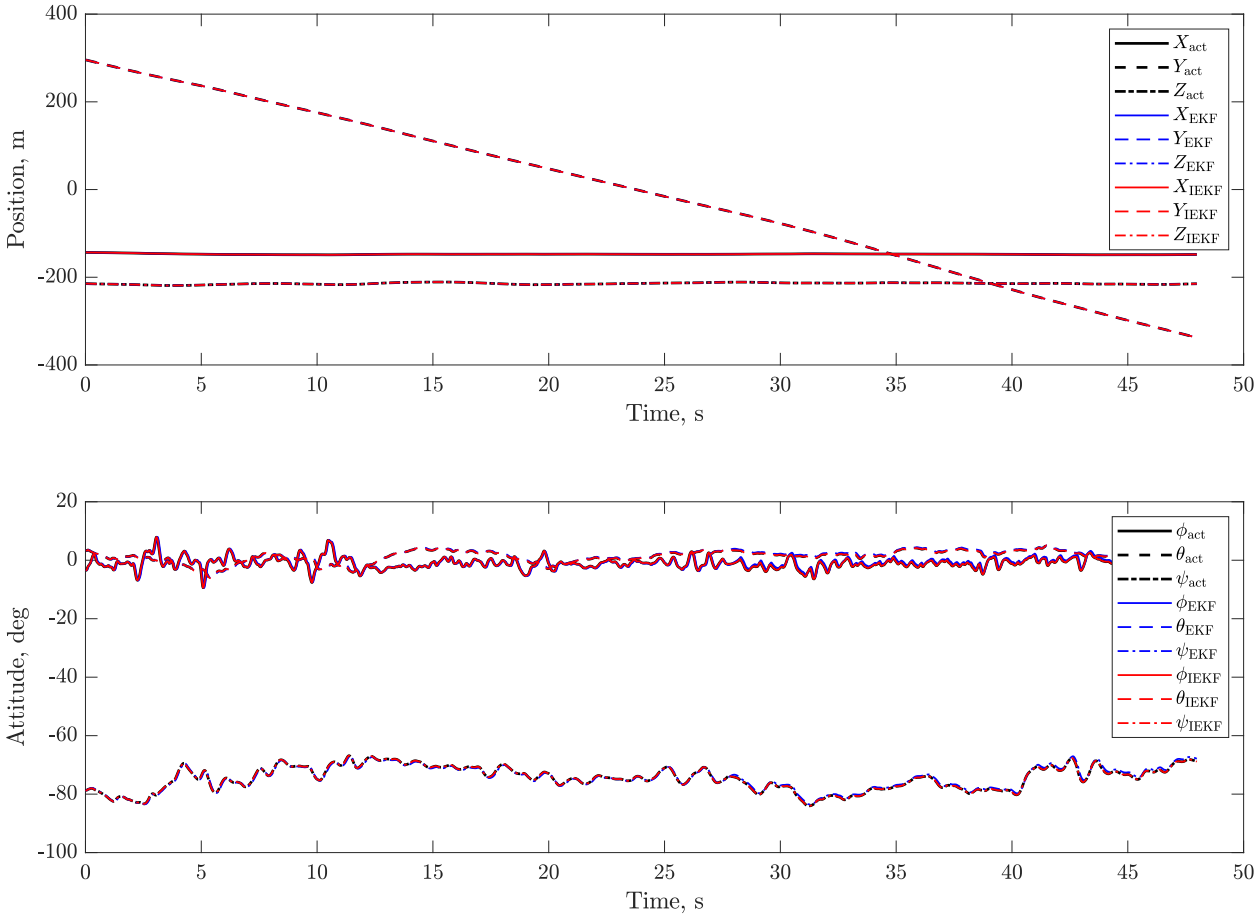

Figure A.7: Position and attitude estimates for the aircraft in straight and level flight using both the invariant EKF and EKF.

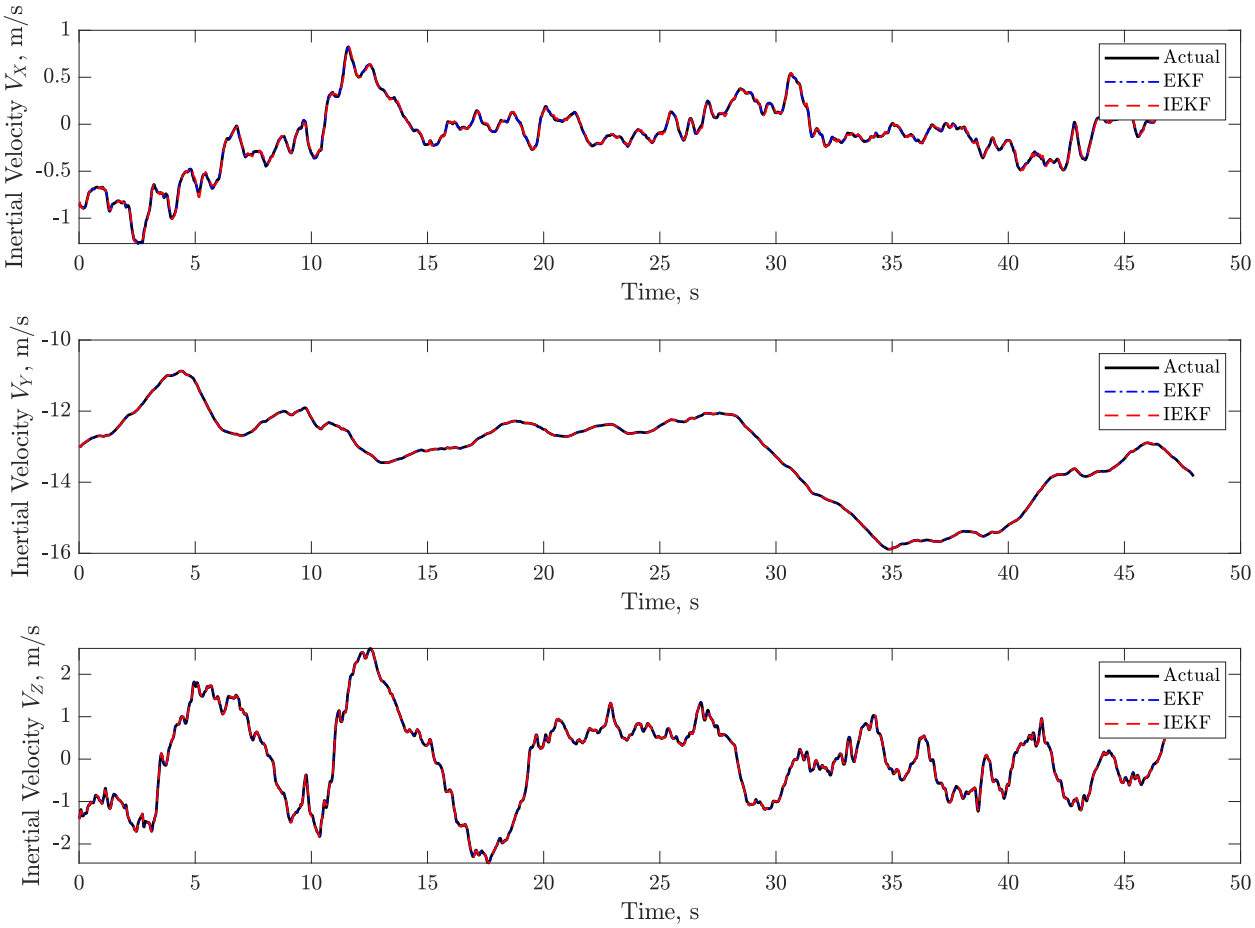

Figure A.8: Inertial velocity estimates for the aircraft in straight and level flight using both the invariant EKF and EKF.

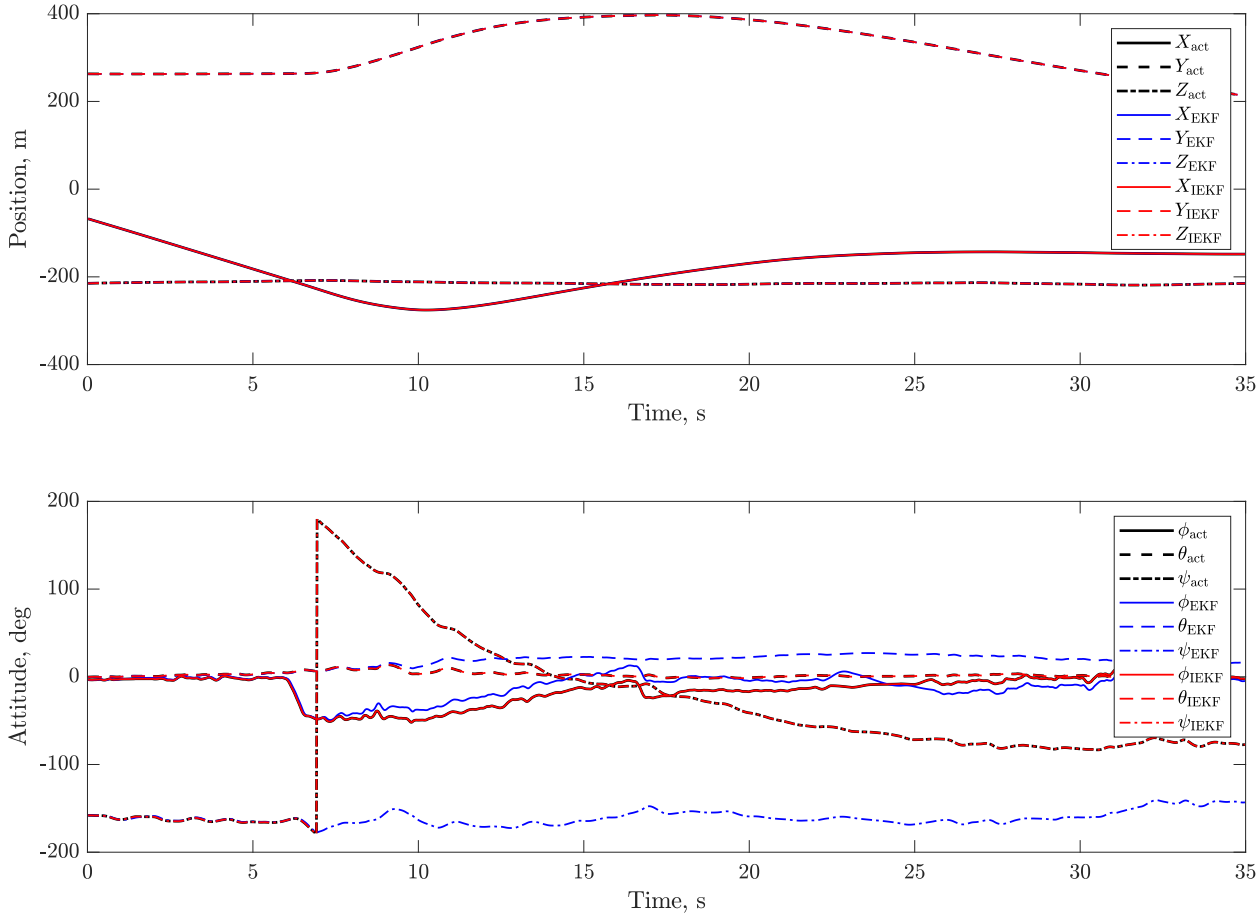

Figure A.9: Position and attitude estimates for the aircraft in a coordinated turn using both the invariant EKF and EKF.

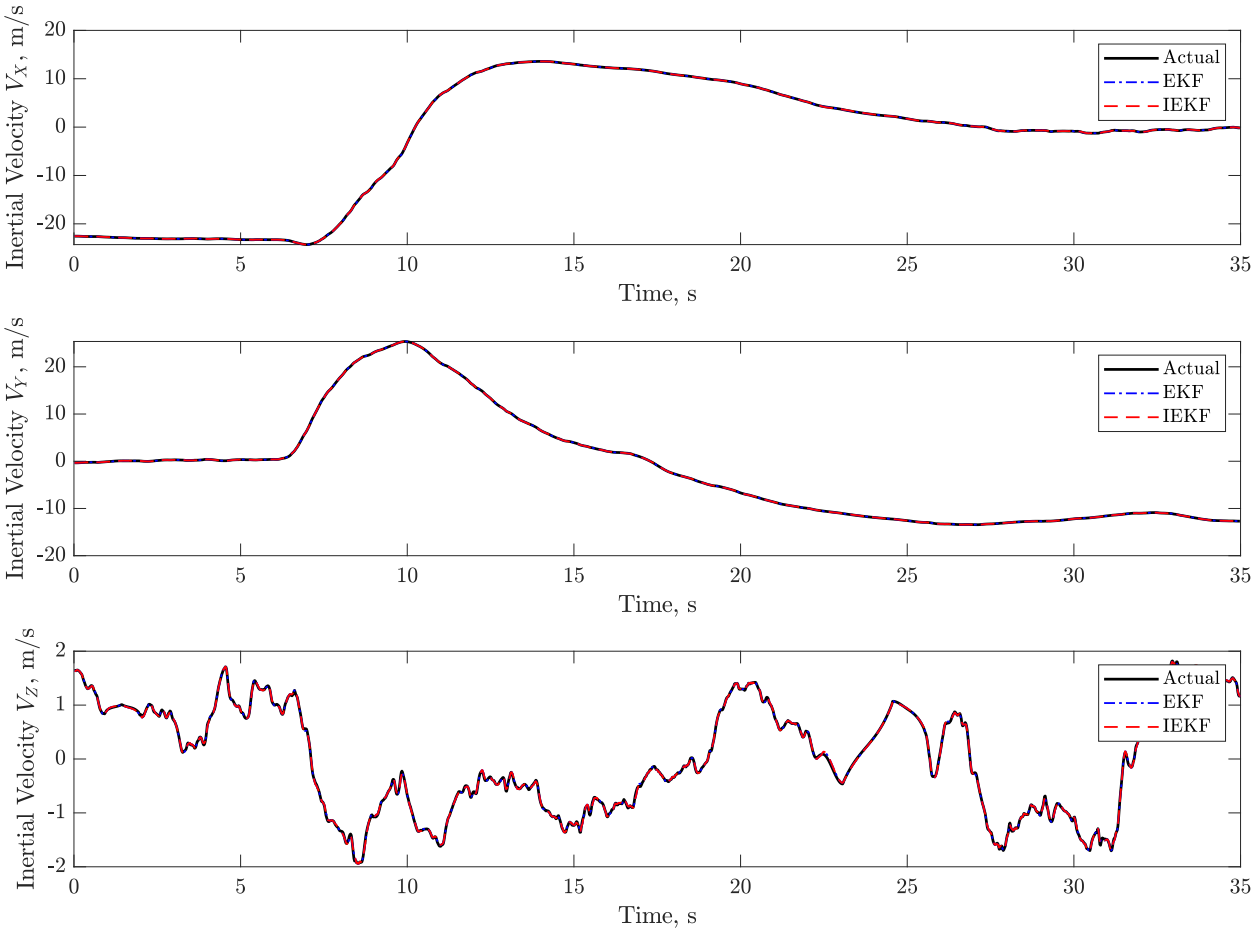

Figure A.10: Inertial velocity estimates for the aircraft in a coordinated turn using both the invariant EKF and EKF.